



LEOPOLD-FRANZENS-UNIVERSITÄT INNSBRUCK

MASTER THESIS

# Fabrication of Superconducting Quantum Bits

*Stephanie Maria Wögerer*

supervised by  
Univ.-Prof. Dr. Gerhard KIRCHMAIR

January 1, 2021



# Abstract

As I started my master thesis in the Superconducting Quantum Circuits group of Univ.-Prof. Dr. Gerhard Kirchmair, the clean room at the IQOQI in Innsbruck was brand new and we were the first people working there. We tried to set up a fabrication procedure for superconducting circuit elements that are used in the experiments of the group. It turned out to be not that straight forward as expected, but in the end we managed to get working elements and could test how they behave at low temperatures of a few Kelvin.

In this thesis I give an overview of the fabrication steps for single quantum bits (qubits). Especially the so called *Josephson junctions* (JJ) are the most interesting parts and need some more attention. At very low temperatures they bring up quantum effects that lead to a nonlinearity in the system. This nonlinearity creates an anharmonic potential which is needed to differentiate between the states in the system and perform controlled excitations. Josephson junctions are widely used for various systems. The single qubits are somehow the simplest applications of the JJ one can create.

After a little introduction and motivation why one is, or could be interested in producing superconducting circuit elements, technically and physically, I give a short summary of the most relevant theory. With these basics one can understand and think about what's important and what to pay attention on fabricating qubits. Then a section to explain the different procedure steps, not just theoretically but also with the parameters we used in the fabrication, follows. In section 10 one can find a presentation of some of the wafers from our fabrication progress, each one with its problems that appeared during fabrication and some "tricks" and ideas how one could solve those. In the last section I present the results from the microwave transmission measurements performed with the fabricated qubits. I compare how they fit to theory and try to give some kind of starting points to do successful qubit fabrication in the new clean room. Beside some numbers how reproducible the fabrication can be performed at the moment, I also calculated an estimation of the junction capacitance, the band gap of the used aluminium and how much the junctions are ageing over time.





## Acknowledgement

First of all I want to thank Gerhard Kirchmair for the opportunity to do my master thesis in his group. Thanks to my office mates Stefan Oleschko who showed me the labs and took me around in my first week and Max Zanner who showed me how to fab. A big thank you to Aleksei Sharafiev who every now and then crashed into my office and told me about his current work, explained me every time a little more about the theory of superconducting quantum bits and didn't get bored to listen and answer all my "stupid" questions. This in general accounts to the whole group! Every time I could ask everyone when I needed something or had some questions, in particular again to Gerhard who patiently explained me things also more than once.

Thanks to every single one who kept me going on during this long journey to finally finish this thesis!



# Contents

<b>1</b>	<b>Introduction</b>	<b>1</b>
<b>2</b>	<b>A philosophical motivation for superconductivity</b>	<b>3</b>
<b>3</b>	<b>Superconductivity</b>	<b>5</b>
3.1	Discovery and theories of superconductivity . . . . .	5
3.2	Josephson Effect . . . . .	6
3.3	Ambegaokar-Baratoff formula . . . . .	8
<b>4</b>	<b>Qubit Description</b>	<b>9</b>
4.1	Short reminder to Hamilton formalism . . . . .	9
4.2	Superconducting qubits as electrical circuits . . . . .	9
<b>5</b>	<b>Idea of the experiment</b>	<b>15</b>
5.1	Experimental set up . . . . .	15
5.2	Rectangular waveguide . . . . .	15
5.2.1	Waveguide without qubits . . . . .	16
5.2.2	Waveguide with qubits . . . . .	16
5.3	Dilution Refrigerator . . . . .	17
<b>6</b>	<b>Simulation of the qubits in the waveguide</b>	<b>19</b>
6.1	Simulation set up . . . . .	19
<b>7</b>	<b>From Theory to Fabrication</b>	<b>21</b>
7.1	Qubit Parameter . . . . .	21
7.2	Numbers for a simulated qubit . . . . .	23
<b>8</b>	<b>Different ways to fabricate Josephson junctions</b>	<b>24</b>
8.1	Dolan-Bridge junction . . . . .	24
8.2	Bridge-free junction . . . . .	24
8.2.1	How to find the right evaporation angle in the example of a Bridge-free junction	25
8.3	Crosstype junction . . . . .	29
<b>9</b>	<b>Fabrication of qubits</b>	<b>30</b>
9.1	Wafer preparation . . . . .	30
9.1.1	Clean the wafer . . . . .	30
9.1.2	Spincoat resist layers . . . . .	31
9.1.3	Sputter gold . . . . .	32
9.2	Electron-beam Lithography . . . . .	33
9.2.1	Theoretical background . . . . .	34
9.2.2	Writing qubits with electron-beam lithography . . . . .	35
9.3	Development . . . . .	42
9.3.1	Remove gold layer . . . . .	42
9.3.2	Develop structures . . . . .	43
9.4	Metal deposition . . . . .	44
9.4.1	Evaporate junction layers . . . . .	44
9.4.2	Lift off residual resist layers with unwanted Al layers . . . . .	46
9.5	Measuring the normal state resistance of the junctions . . . . .	47
<b>10</b>	<b>Fabrication progress</b>	<b>49</b>
10.1	Test for different junction sizes on Silicon . . . . .	49
10.2	Dose test on sapphire - KC003329 . . . . .	51
10.3	Having a closer look with the e-beam - KC003326 . . . . .	56
10.4	Reproduction of the previous wafer - KC003361 . . . . .	61
10.5	Last test - KC003364 . . . . .	66
10.6	Take aways of the fabrication progress . . . . .	72

10.7 Qubits to cool down - KC003368 & KC003369 . . . . .	73
10.7.1 Design of the measured qubits . . . . .	73
<b>11 Microwave transmission measurement</b>	<b>77</b>
11.1 Waveguide set up . . . . .	77
11.1.1 Impedance matching . . . . .	77
11.2 Performing measurements . . . . .	78
11.3 Results . . . . .	80
11.3.1 Characterizing the qubits . . . . .	80
11.3.2 Comparison of measurement and theory . . . . .	83
11.3.3 Autler-Townes splitting . . . . .	85
<b>12 Conclusion and Outlook</b>	<b>88</b>
<b>Appendices</b>	<b>93</b>

"Nature isn't classical, dammit, and if you want to make a simulation of Nature, you'd better make it quantum mechanical, and by golly it's a wonderful problem, because it doesn't look so easy."  
*R. Feynman*

## 1 Introduction

Nowadays everybody has heard or knows about quantum physics. Especially quantum computers seem to be the most prominent examples for quantum technologies people talk about. In general, the leading areas are quantum communication, quantum simulation, quantum sensors and, of course, the quantum computer. To give an estimation of the directions, possibilities and time

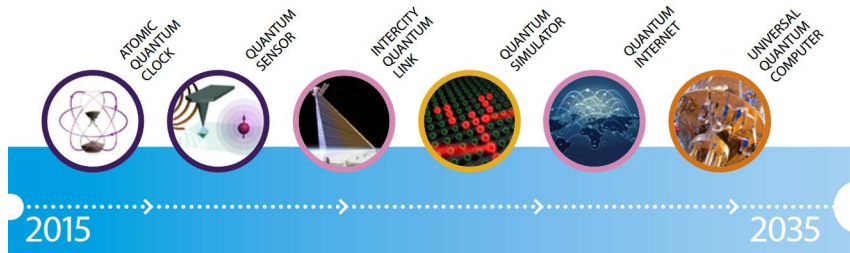


Figure 1: Timeline for quantum technologies. In the fields of communication (circled in pink), simulations (yellow), sensors (dark blue) and computers (orange), we can expect great scientific advances in the next ten to fifteen years from quantum technologies. Picture taken from [1]

scales for the future of quantum technologies, an illustrative of the predictions for the biggest mile stones, is shown in fig.1.

In 2016 leading european scientists kick off the so called *Quantum Manifesto* "...to launch an ambitious European initiative in quantum technologies, needed to ensure Europe's leading role in a technological revolution now under way." [1]

There, in a rough outline up to 2020, they expected things like a core technology of quantum repeaters and a secure point-to-point quantum link for quantum communication, a simulator for the motion of electrons in materials, quantum sensors for gravity, magnetic sensors for health care, geosurvey and security, small quantum processors and the operation of a logical qubit protected by error correction or topologically.

In the following five years the development is predicted to reach quantum credit cards, quantum networks between distant cities, the development and design of new complex materials with quantum simulators, quantum navigation devices and a quantum computer with up to 100 physical qubits to solve chemistry and material science problems.

Even further in the future the goals are set and predicted to move in the direction of a secure Europe-wide internet merging quantum and classical communication, simulators of quantum dynamics and chemical reaction mechanisms to support drug design, gravity imaging devices based on gravity sensors and quantum computers exceeding the computational power of classical computers.[1]

All these technologies are based on the usage of quantum states. Based on the bits of a classical computer, also the elementary units of information storage for a quantum computer are called *qubits*. This quantum mechanical two-level-systems can, in analogy to the 0 and 1 state of a classical computer, also operate with superpositions of the two states of the qubit.

There are a few different systems in which this states can be defined. For example nuclear spins, selected electron states of an ion or, like in our case, superconducting circuits. Currently, people are testing which of these systems can be used best for the applications mentioned above.

In this competition, superconducting qubits are promising candidates to operate as a quantum computer. They are scalable and the qubit parameters can be flexibly changed in fabrication. The negative aspects are, that they are strongly coupled to the environment and therefore to the external degrees of freedom. Furthermore they bring along inherent, difficult to control variations

due to the fabrication process. However there are also some benefits due to the superconductivity of their material. Two-level-systems defined in the energy gap of the superconductor, are effectively decoupled from quasi particles and the environment. In addition, the superconducting state itself already provides a non degenerate, macroscopic ground state.[2] Therefore it seems to be a promising choice to put effort into it and get to know and develop this type of qubits. During my work as a master student we tried to set up and characterize the qubit fabrication in the new clean room at the IQOQI in Innsbruck. A summary of the fabrication and the results are presented in this thesis.

"...in the beginning when the world was  
young there were a great many thoughts  
but no such thing as a truth."

S. Anderson

The book of grotesque

## 2 A philosophical motivation for superconductivity

Back in history the laws of physics are established by observing the behaviour of the nature and the things around. With geometric and kinematic considerations Newton for example developed three physical laws in 1687, describing forces that act on a body and its motion as response to those forces, that laid the foundation for today's classical mechanics. To the question of the origin and nature of these forces, Newton gave the famous answer "*hypotheses non figo* - I frame no hypotheses". In 1695 Leibniz presents his *Specimen Dynamicum* as kind of an answer to Newton where he missed the substantiation of physics. He not just focuses on the motion itself but in particular also on the origin. According to Leibniz physics has to be about to understand the motion **together** with its origin, even if they may be just hypotheses at first.

In the 19th and 20th century, also as a result of the progressive mathematization, physics more and more moved away from the description of the directly perceived. Accompanied with an increasing loss of vividness. An example of this perspective change are the descriptions of the electric and magnetic phenomena observed. They seemed to be a completely new type of physical interaction. In analogy to the continuum mechanics and fluid mechanics not the motion of single physical objects through the space is tracked now, but the temporal development of the mechanical properties. It was somehow the change from a "particle theory" description to a "field theory" description. In 1915 Albert Einstein established a field theory of gravity depicted by the geometry of space and time. The general theory of relativity. The hope grew to merge both known interactions (gravity and electromagnetism) into a single theory. The old idea to reduce all the physics to geometry influenced also the physics of the 20th century and was now, compared to the geometrisation of Platon and Descartes, mathematically much more prepared.

The troubles on the way to this unified field theory came up when people wanted to describe phenomena on the atomic level. Many of the physical quantities are not continuous anymore but appear "stepwise" as a multiple of a certain value. They are quantized. This discrete structure was hardly compatible with the continuous equations in the field-theoretical approach.

Was it first a problem of direct observation, now also analogies like the atomic angular momentum or Bohr's atomic model, coming from the physics of the gyro, got problematic. For the directional quantization observed in the Stern-Gerlach-Experiment for example exists no classical analogy. To deal with it they put a "spin" on the electron. The focus now was more on finding a mathematical formalism for the experimental results to make accurate predictions. In 1925 Heisenberg and Schrödinger provided the central designs for a theory now known as quantum mechanics. As in classical physics, also in quantum physics, the state of a system at any time  $t$  for a given initial state can be determined from a basic equation. In quantum mechanics the evolution of a quantum mechanical system is described by the so called Schrödinger equation

$$i\hbar \frac{\partial}{\partial t} \Psi(\mathbf{r}, t) = -\frac{\hbar^2}{2m} \frac{\partial^2 \Psi(\mathbf{r}, t)}{\partial \mathbf{r}^2} + V\Psi(\mathbf{r}, t)$$

with the reduced Plank constant  $\hbar$ , the potential energy  $V$ , the mass  $m$  and the wave function  $\Psi(\mathbf{r}, t)$  of the particle. In general a wave function doesn't have significance in the classical world. Quantum mechanical behaviour usually doesn't show up on large scales except in the standard way that it reproduces Newton's laws.

When Schrödinger discovered his equation he started calculating some problems and found out, that it doesn't always work out quite right and doesn't fit to experimental observations. A solution to this inconsistency brought Max Born. His idea was to interpret the values of the quantum mechanical formalism as probabilities.[3] The product of the function  $\Psi$  in the Schrödinger equation with its complex conjugate, for example, should be interpreted in terms of a probability amplitude

$$P(\mathbf{r}, t) = \Psi^*(\mathbf{r}, t)\Psi(\mathbf{r}, t)$$

The wave function  $\Psi$  doesn't describe a smeared out electron with a smooth charge density anymore, but the probability to find the electron somewhere with its entire charge at that point.

Now think of not only one electron, but the situation of a huge number of particles in exactly the same state with exactly the same wave function. We will find for any of the particles in any volume  $dx dy dz$  a number close to  $\Psi\Psi^* dx dy dz$ . So every single one of those many identical electrons has more or less the same probability to be in any volume  $dx dy dz$ . The product  $\Psi\Psi^*$  can in this situation then again be interpreted as the electric charge density.

Therefore in the situation where you have a lot of particles in the same state, the charge density  $\rho$  can be calculated directly from the wave function  $\Psi(r) = \sqrt{\rho(r)} \cdot e^{i\varphi(r)}$ . The wave function suddenly takes on a physical meaning which extends into classical, macroscopic situations.

At low temperatures for example, when only a very small number of states near the ground state are occupied by such a possibly huge number of particles, the quantum mechanical character of that ground state can appear on a macroscopic scale. This time not in the usual way that quantum mechanics reproduces Newtonian mechanics on the average, but in the situation where quantum mechanics produce its own characteristic effects on a "macroscopic" scale.[4]

Superconductivity is exactly that situation. Cooling down a metal to very low temperatures leads to Cooper pairing which allows a lot of particles in the same state. The quantum mechanical behaviour of these particles now can appear on a macroscopic scale - in our case in form of the Josephson Effect.



"Real new territory in science can  
probably only be gained if you are, at  
a crucial point, ready to leave the ground  
on which the previous science is based."  
*Werner Heisenberg*

### 3 Superconductivity

This chapter starts with the historical discoveries which lead to different theories to describe superconductivity. Followed by the ideas to explain and describe the new physical states, the *BCS ground states*, that are appearing. Then we come to the special case for weakly coupled superconductors. The *Josephson effect* that is observable in this case motivates the fabrication and the design of the so called *Josephson junctions* - the experimental realisations of weakly coupled superconductors. The last part is about the connection between the *BCS-theory* and *Josephsons theory* to weakly coupled superconductors. The resistance in the resulting equation, measured at room temperature, provides an easy accessible parameter to draw conclusions about the properties of the junction at low temperatures. For the fabrication of qubits this is an important parameter to check the functionality of the qubits.

#### 3.1 Discovery and theories of superconductivity

The electrical resistance of metals is caused by scattering of the conduction electrons on phonons and lattice defects as well as by scattering among each other. With decreasing temperature the resistance should also decrease due to freezing out phonons, but should never disappear completely because of the residual lattice defects and impurities.

In 1911 Heike Kamerlingh Onnes discovered that at a certain temperature the resistance suddenly isn't measurable anymore and disappears. He first discovered it in experiments with mercury. (see fig.2). This temperature is now called the critical temperature  $T_C$ . It is different for different materials and lies around a few to a few hundred Kelvin. In 1933 Walther Meißner and Robert

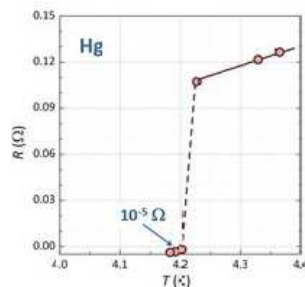


Figure 2: Data from the lab book of Kamerlingh Onnes. The resistance in dependence of the temperature for mercury. It was the discovery of the "critical temperature" at which suddenly the resistance goes to zero.[5]

Ochsenfeld discovered that superconducting materials are also perfect diamagnets as they completely displace magnetic fields from their inside.

In general superconductivity is a phenomena in which correlations in the electronic system play an important role. They lead, below the critical temperature, to a new kind of order and are difficult to describe because there is effectively not just one electron anymore to describe but a lot of them. That's the reason why there is up to now no established microscopic theory for high-temperature superconductors for example.

In the beginning a lot of theories were developed which could describe the experimental results correctly but couldn't explain them. Starting with a bifluid model from *Casimir* and *Gorter* describing correctly the vanishing resistance below  $T_C$ , the model of Fritz and Heinz *London*, where there is a finite density of superconducting electrons which could move without friction, can describe the infinitely high conductivity and the perfect diamagnetism. *Ginzburg* and *Landau* introduced

a complex macroscopic wavefunction as regulatory parameter which describe the local density of the superconducting electrons as  $\rho(r) = |\Psi(r)|^2$ . This theory could explain especially phenomena where the spatial variation of the density of the superconducting electrons is important.

The real breakthrough came in 1957 with the microscopic theory of *Bardeen, Cooper* and *Schrieffer*, the so called BCS-theory. They recognized that the existence of an attractive interaction between the electrons of a metal leads to pairing of the electrons. The pairs are called *Cooper pairs*. Below the critical temperature  $T_C$  the Cooper pairs build a coherent many-body state which again can be described with a single macroscopic wave function.

In 1961 two experimental groups simultaneously observed the quantisation of the magnetic flux in units of the flux quantum  $\Phi_0 = \frac{h}{2e} = 2.0678 \times 10^{-15}$  Wb. It was the first time that the existence of Cooper pairs with charge  $-2e$  was proven.

But let's see how the Cooper pairs can appear and start with a little thought experiment. Assuming that we have a gas of free electrons at  $T = 0$  K where all states up to the Fermi energy  $E_F = \hbar^2 k_F^2 / 2m$ , with the wave vector  $k_F$ , the reduced Planck constant  $\hbar$  and the mass of the particle  $m$ , are occupied. Adding two additional electrons allows them to interact with each other via the crystal lattice by exchanging phonons. Since the next free states for the electrons are above  $E_F$  and the maximum energy for the phonons is  $\hbar\omega_D$ , with the Debye-Frequency  $\omega_D$ , the interaction of the electrons take place in the region between  $E_F$  and  $E_F + \hbar\omega_D$  with the corresponding wave vectors  $k_F$  and  $\Delta k \simeq \frac{m\omega_D}{\hbar k_F}$ . In this momentum region Cooper pairs are scattered permanently into new states so that we choose for the pair-wave-function to describe a Cooper pair the ansatz of a superposition of the product-wave-function in the interval  $[k_F, k_F + \Delta k]$

$$\Psi(\mathbf{r}_1, \mathbf{r}_2) = \sum_{k=k_F}^{k_F+\Delta k} a_k e^{i\mathbf{k}_1 \mathbf{r}_1} e^{i\mathbf{k}_2 \mathbf{r}_2} = \sum_{k=k_F}^{k_F+\Delta k} a_k e^{i\mathbf{k} \mathbf{r}}$$

With this ansatz we can solve the Schrödinger equation for the electron pair

$$-\frac{\hbar^2}{2m} (\Delta_1^2 + \Delta_2^2) \Psi(\mathbf{r}_1, \mathbf{r}_2) + V(\mathbf{r})\Psi(\mathbf{r}_1, \mathbf{r}_2) = E\Psi(\mathbf{r}_1, \mathbf{r}_2).$$

The interaction potential  $V(\mathbf{r})$  depends only on the relative coordinate  $\mathbf{r}$  and includes the Coulomb interaction via the lattice as the attractive interaction between the electrons. The calculations are skipped here, which can for example be looked up in [5] p.849 ff., and we go directly to the solution for the appropriate case of weak interaction

$$E \simeq 2E_F - 2\hbar\omega_D e^{-4/D(E_F)V_0}.$$

During the calculation a few assumptions and simplifications were made, but for now let's just define what the different variables mean and not where they come from.  $D(E_F)$  is the density of states at the Fermi energy and  $V_0$  is the interaction potential under the assumption of an isotropic interaction.

We see that the energy is smaller than  $2E_F$  which means that we have a bound two-electron state, a Cooper pair. It leads to a reduced energy in contrast to free electrons. Thereby the gas of interaction-free electrons becomes unstable compared to the paired electrons. This instability causes a transition to a new ground state of the electron system, the so called *BCS ground state*. [5] This new coherent many body state of the electrons as we heard before can be described with a single wave function through the charge density  $\rho$  and a phase  $\varphi$

$$\Psi = \sqrt{\rho} \cdot e^{i\varphi}$$

### 3.2 Josephson Effect

In 1962 interesting phenomena for weakly coupled superconductors were predicted by Brian D. Josephson. If two superconductors are coupled weakly, by for example a thin insulating layer, their wave functions have a finite overlap. Since the probability of a single electron to tunnel in a superconductor-insulator-superconductor (SIS) contact is already smaller than  $10^{-4}$  it was expected that the probability of a pair of electrons to tunnel has to be unmeasurable small, about

$(10^{-4})^2$ . Josephson broke this mindset and postulates that the probability of a Cooper pair to tunnel is the same as for a single electron.

He predicted two effects. A possible supercurrent  $I_s$  at zero voltage and an oscillating supercurrent, at an applied voltage  $V$  across the junction, with a frequency  $\frac{2e}{h}V$ , where  $h$  is the Planck constant.

In fig.3 the current depending on the voltage across a SIS tunnel junction is plotted for different

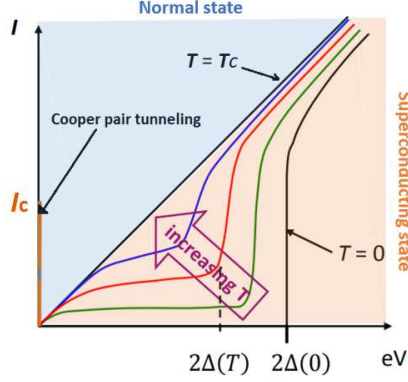


Figure 3: Current  $I$  depending on the voltage  $V$  across the junction. On the very left, the predicted supercurrent  $I_C$  at zero voltage is shown. The linear slope at the critical temperature  $T = T_C$  indicates the transition from the *normal state* (the resistance follows Ohms law) to the *superconducting state* (resistance doesn't follow Ohms law anymore). At the absolute zero point  $T = 0$ , a current just appears at an applied voltage of  $2\Delta$ . There, one can directly read out the value for the band gap  $\Delta$  of the used material. Picture taken from [6] and modified.

temperatures. On the very left, the predicted supercurrent  $I_C$  of Cooper pairs at zero voltage is visible. The black linear line for  $T = T_C$  indicates the transition from the normal state to the superconducting state. Left hand side of this line, the linear I-V dependence correspond to Ohms law. The current just consists of single electrons. Right hand side, the electrons begin to pair and an additional current of Cooper pairs contribute. For small voltages of a few meV the I-V dependence is not linear anymore.

Let's start in a pure superconducting state at a temperature  $T = 0$ . For  $T = 0$  the tunnel current only starts when reaching a voltage  $eV = 2\Delta(0)$ , depending on the band gap  $\Delta$  of the junction material. There, at  $T = 0$ , one can directly read out the value of the band gap of the used superconductors from the measured I-V-curve.[5] Is the voltage across the junction much higher than the gap value, a Cooper pair breaks up and one of the resulting single electrons, which are called *quasiparticles*, can pass to the other electrode. This current of quasiparticles is called the *normal current*  $I_N$  and contributes together with the supercurrent to the total current  $I = I_N + I_C$ . The greater the proportion of normal current, the more the I-V-curve becomes linear again, like for the classical Ohm's law without Cooper pairs.

For temperatures  $T > 0$  there is some thermal motion of charge carriers with an energy of about the Boltzmann constant times the temperature  $k_B T$ . This motion can also break up Cooper pairs and create quasiparticles. With increasing temperature the thermal energy  $k_B T$  also increases. If the thermal energy becomes much higher than the binding energy of the Cooper pairs, much more single electrons than Cooper pairs are around. Therefore, at temperatures closer and closer to  $T_C$ , as shown in fig.3, more single electrons than Cooper pairs contribute to the current and the I-V curve also in this case gets closer and closer to Ohms law.[7]

To describe the observed effects for weakly coupled SIS junctions at low temperatures, Josephson derived two equations. In fig.4 the two superconductors, described with the wave functions  $\Psi_1$  and  $\Psi_2$  and separated by a tunnel barrier of thickness  $d$ , are shown. Provided that the tunnel barrier is considerably thinner than the superconducting coherence length, the theory to explain the predicted effects across the junction is, that they appear because the amplitudes of  $\Psi_1$  and  $\Psi_2$  for the condensed electron pairs may overlap in the oxide layer. This is the case even though the band gap is essentially zero there.[8]

The first equation Josephson derived, also known as current-phase-relation, says, that the super-

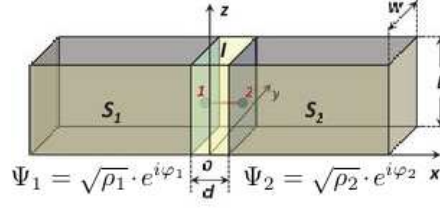


Figure 4: Schematics of a superconductor-insulator-superconductor contact, a so called Josephson contact. The insulator is the tunnel barrier with thickness  $d$ . The two superconductors can be described with the wave functions  $\Psi_1$  and  $\Psi_2$ . [5]

current density  $J$  varies sinusoidal between the two contact electrodes with a phase difference  $\varphi$  between the two macroscopic wave functions  $\Psi_1$  and  $\Psi_2$  of the superconductors.

$$J(\varphi) = J_c \sin(\varphi) \quad (1)$$

The second equation, the voltage-phase-relation, reads

$$\frac{\partial \varphi}{\partial t} = \frac{2\pi}{\Phi_0} V \quad (2)$$

and describes the connection between the change of the phase  $\varphi$  over time and the voltage across the junction. [5]

### 3.3 Ambegaokar-Baratoff formula

In 1963 Vinay Ambegaokar and Alexis Baratoff generalized Josephsons calculations and related them to the BCS-theory. For symmetrical junctions, with the same electrode materials, they calculated a quite simple temperature dependence of the supercurrent  $I_C$ , using the "BCS-temperature-dependence" of the gap

$$I_C R_n = \frac{\pi}{2e} \Delta(T) \tanh \left( \frac{\Delta(T)}{2k_B T} \right) \quad (3)$$

[7].  $I_C$  is the maximum supercurrent and  $R_n$  the normal state resistance. In our case the temperature is so small, that  $\tanh(\Delta(T)/2k_B T) \approx 1$  and the band gap  $\Delta(T)$  can be approximated as a constant. For the calculations to my qubits, I therefore used the formula

$$I_C = \frac{\pi \Delta}{2e} \frac{1}{R_n} \cdot 0,87. \quad (4)$$

The constant value 0,87 is an experimentally evaluated value. It corrects the difference in resistance measured at room temperature and at a few mK (see also [9], where the resistance changed from 300 to 77 K by about 15%). In sec.11.3.2 we plotted the critical current  $I_C$  of our qubits against their measured normal state resistance  $R_n$  and could calculate a value of  $\Delta = 1,57 \pm 0,06 \cdot 10^{-4}$  eV for the band gap of the used aluminium.

For further descriptions of the dynamics of a Josephson junction we have to introduce additional dimensions like the Josephson coupling energy  $E_J$  or the charging energy  $E_C$ . [10] How we get them, what they mean and for what they are useful we will see in the next sections.

"The real problem with time travel is not  
that you can become your own father.  
A good family therapy copes with this.  
The problem is the grammar."  
*Douglas Adams*

## 4 Qubit Description

This chapter starts with a short reminder to the Hamilton formalism which is used to describe the qubits as electrical circuits. Followed by the description of a classical linear LC resonant circuit, to understand the dynamics of the system. Then we'll go further, quantize it and go to the anharmonic case of the non-linear circuit with the Josephson junction. In sec.7 it is discussed how the parameters in the theory can be connected to the design parameters of the physical qubit in the experiment.

### 4.1 Short reminder to Hamilton formalism

A mechanical system with  $s$  degrees of freedom can be described by  $s$  general coordinates

$$q = \{q^\alpha\}_{\alpha=1,\dots,s}$$

and the corresponding derivatives

$$\dot{q} = \{\dot{q}^\alpha\}_{\alpha=1,\dots,s}$$

Together with the time they are the arguments of the Lagrange function  $\mathcal{L}(t, q, \dot{q}) = \mathcal{T} - \mathcal{U}$ , with the kinetic energy  $\mathcal{T}$  and the potential energy  $\mathcal{U}$ , which contains the whole information of a system. One can define to each coordinate  $q^\alpha$  its conjugate variable, the momentum  $p_\alpha$

$$p_\alpha \equiv \frac{\partial \mathcal{L}(t, q, \dot{q})}{\partial \dot{q}^\alpha}$$

Now the motion of a mechanical system at time  $t$  can be characterized not just with the coordinates and the corresponding velocities, but also via the generalized coordinates and the momenta conjugated to them. To do so, one needs instead of the Lagrange function  $\mathcal{L}(t, q, \dot{q})$  a new function with the "new" variables. This new function, the Hamilton function, defined as

$$\mathcal{H}(t, q, p) \equiv \sum_{\alpha=1}^s p_\alpha \dot{q}^\alpha - \mathcal{L}(t, q, \dot{q})$$

has the same information as the Lagrange function, just with other variables.[11]

### 4.2 Superconducting qubits as electrical circuits

Superconducting qubits can be described as electrical circuits. The elements of such a circuit can be for example the linear elements, resistors (R), capacitors (C) and inductors (L), or the Josephson element, which acts as a non-linear inductor. In the classical case the simplest combination of those elements is the LC circuit. Using superconducting materials for this circuit and operating it at low enough temperatures ( $< 100$  mK), the circuit gets naturally prepared in a quantum mechanical ground state (the BCS-ground-state, discussed before). Although we now have a quantum system, it still behaves classical and we get *coherent states*. To achieve quantum mechanical behaviour and get, for example, *qubit states*, we need to realize anharmonic energy levels. This we can do by including a non-linear element in the circuit.

Therefore we replace the linear inductor element with the non-linear inductor element, the Josephson junction. This creates an anharmonic quantum oscillator potential whose lowest energy levels can be used as a qubit. [12]

In fig. 5 the linear LC circuit and its energy levels on the left side (in (a) and (b)) and the non-linear circuit and its energy levels on the right side (in (c) and (d)) are shown. But let's start with

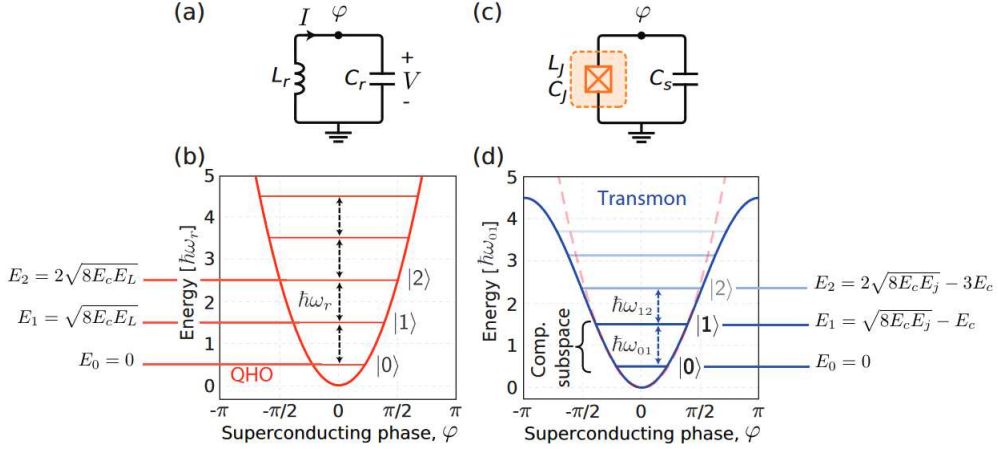


Figure 5: (a) Circuit diagram of a simple harmonic resonant circuit with the inductor  $L_r$  and the capacitor  $C_r$ .  $I$  is the current flowing through the circuit,  $\varphi$  the superconducting phase and  $V$  the voltage through the capacitor. (b) The energy diagram of the circuit shown in (a). It's a quantum harmonic oscillator (QHO) quadratic potential with equidistantly spaced energy levels. (c) Circuit diagram of an anharmonic circuit, where the linear inductor is replaced by a Josephson junction which acts as nonlinear inductor  $L_J$  and brings another capacitance  $C_J$  to the circuit. (d) Shows the potential energy plot of the circuit in (c) with the not equidistantly spaced energy levels. The first two energy levels build the computational subspace in which most of the qubit operations take place. Picture taken from [13] and modified.

(a) and see how (b), (c) and (d) follow.

In a linear LC resonant circuit the electrical and magnetic energies oscillate between the capacitor  $C$  and the inductor  $L$ . The instantaneous, time-dependent energy in each element is given by the voltage  $V(t)$  and the current  $I(t)$  related to the capacitor and the inductor

$$E(t) = \int_{-\infty}^t V(t')I(t')dt' \quad (5)$$

### Harmonic Oscillator

In any system, classical or quantum mechanical, to derive the dynamical behaviour, one needs the Hamiltonian of the system. The generalized circuit coordinates of the circuit are charge and flux. They are defined through current and voltage as

$$\begin{aligned} \Phi(t) &= \int_{-\infty}^t V(t')dt' \\ Q(t) &= \int_{-\infty}^t I(t')dt'. \end{aligned} \quad (6)$$

We arbitrarily pick flux as our variable to derive the Hamiltonian through the classical Lagrange-Hamilton-formalism. One gets the same result for charge. With the relations

$$\begin{aligned} I &= C \frac{dV}{dt} \\ V &= L \frac{dI}{dt} \end{aligned}$$

and equations (5) and (6) we can find the energy terms for the capacitor

$$\begin{aligned} E(t) &= \int_{-\infty}^t V(t') C \frac{dV}{dt'} dt' = C \left( [V(t')V(t')]_{-\infty}^t - \int_{-\infty}^t \frac{dV(t')}{dt'} V(t') dt' \right) \\ &= 2 \int_{-\infty}^t CV(t') \frac{dV(t')}{dt'} dt' = CV(t')^2 \\ &= \int_{-\infty}^t CV(t') \frac{dV(t')}{dt'} dt' = \boxed{\frac{1}{2} C \dot{\Phi}(t)^2 = E_C(t)} \end{aligned}$$

and the inductor

$$E(t) = \int_{-\infty}^t L \frac{dI}{dt'} I(t') dt' = \frac{1}{2} L \dot{Q}(t)^2 = \frac{1}{2} LI(t)^2 = [\Phi = -LI] = \frac{L}{2} \frac{\Phi^2}{L^2} = \boxed{\frac{1}{2L} \Phi^2 = E_L(t)}.$$

Comparing these energies to that of a classical harmonic oscillator we can see some analogies. The energy of the capacitor looks like the kinetic energy term of the harmonic oscillator and the energy term of the inductor looks like the potential energy term of the harmonic oscillator. With these two energy terms we can now build the Lagrangian and derive the Hamiltonian of the system.

$$\begin{aligned} \mathcal{L} &= \frac{1}{2} C \dot{\Phi}^2 - \frac{1}{2L} \Phi^2 \\ \mathcal{H} &= \frac{\partial \mathcal{L}}{\partial \dot{\Phi}} \dot{\Phi} - \mathcal{L} = \underbrace{C \dot{\Phi}}_Q \dot{\Phi} - \frac{1}{2} C \dot{\Phi}^2 + \frac{1}{2L} \Phi^2 = C \dot{\Phi}^2 \cdot \frac{C}{C} - \frac{1}{2} C \dot{\Phi}^2 \cdot \frac{C}{C} + \frac{1}{2L} \Phi^2 = \boxed{\frac{Q^2}{2C} + \frac{\Phi^2}{2L} = \mathcal{H}} \end{aligned}$$

With the relations  $Q = C\dot{\Phi}$  and  $\dot{\Phi}(t) = V(t)$  the Hamiltonian can also be expressed as

$$\mathcal{H} = C \frac{V^2}{2} + L \frac{I^2}{2}. \quad (7)$$

So far, there was no quantum mechanic necessary to get the Hamiltonian of the system. To describe the phenomena observed at low temperatures and small scales, where a classical description is not valid anymore, we have to extent the theory and quantize the circuit.

According to the second postulate of quantum mechanics each observable can be represented by an operator. We therefore "make" our variables of the system, the flux and charge coordinate, to operators by putting a hat on them. The flux and the charge are canonically conjugate variables  $([\hat{\Phi}, \hat{Q}] = [\hat{\Phi}, -i\hbar \frac{\partial}{\partial \Phi}] = i\hbar)$ , just like in the quantum harmonic oscillator (QHO) case with the variables position  $x$  and momentum  $p$ .

Defining the reduced flux  $\phi \equiv 2\pi \frac{\Phi}{\Phi_0}$ , with the superconducting flux quantum  $\Phi_0 = \frac{h}{2e}$ , and the reduced charge  $n \equiv \frac{Q}{2e} = \hat{n} - n_g$  with the charge number operator  $\hat{n} = \frac{\hat{Q}}{2e}$  and a possible offset charge  $n_g = \frac{Q_g}{2e}$  coming from capacitive couplings to external charges, we can write the Hamiltonian as

$$\mathcal{H} = \frac{\hat{Q}^2}{2C} + \frac{\hat{\Phi}^2}{2L} = 4 \underbrace{\frac{e^2}{2C}}_{E_C} n^2 + \frac{\hat{\phi}^2}{2} \underbrace{\frac{\Phi_0^2}{4\pi^2 L}}_{E_L} = \boxed{4E_C n^2 + \frac{1}{2} E_L \hat{\phi}^2 = \mathcal{H}}. \quad (8)$$

In this form of the Hamiltonian we can interpret  $\frac{e^2}{2C} = E_C$  as the charging energy of the capacitor needed to add one electron and  $(\frac{\Phi_0}{2\pi})^2 \frac{1}{L} = E_L$  as the energy of the inductor to carry one flux quantum.

Solving the eigenvalue problem of this Hamiltonian one finds eigenenergies  $E_k$  to the eigenstates  $|k\rangle$ , ( $k = 0, 1, 2, \dots$ ), spaced equidistantly with  $E_{k+1} - E_k = \hbar\omega_r$ . The resonant frequency  $\omega_r$  of the system is given by

$$\omega_r = \sqrt{8E_C E_L} / \hbar = \frac{1}{\sqrt{LC}}. \quad (9)$$

Fig.5 (b) shows the energy potential of the LC circuit harmonic oscillator with its equidistant energy levels. To not excite all of the levels at the same time by sending a wave with the resonant frequency  $\omega_r$  and creating a coherent state, we need to make the potential anharmonic. To achieve the anharmonicity between the states we have to include a non-linear element in our circuit. We exchange the linear inductor with a Josephson junction (see fig. 5 (c)).

## Anharmonic Oscillator - Qubit = Transmon

Let's see how the Hamiltonian changes when exchanging the linear inductor with the non-linear inductor in our circuit. As we saw in the calculations before, the energy of the inductor can be seen as the potential energy of the system and the energy of the capacitor as the kinetic energy. To find the Hamiltonian of this new system with the Josephson junction we proceed just as before. For the kinetic energy we find again the equation  $E_{kin} = \frac{1}{2}C\dot{\Phi}(t)^2$ . Also the potential energy term calculates in the same way from equ.5, but now with the two Josephson relations (see equ.1 and 2)

$$I = I_C \sin(\varphi), \quad V = \frac{\Phi_0}{2\pi} \frac{d\varphi}{dt} \quad (10)$$

$$E_{pot}(t) = \int \frac{\Phi_0}{2\pi} \frac{d\varphi}{dt'} \cdot I_C \sin(\varphi) dt' = I_C \frac{\Phi_0}{2\pi} \int \sin(\varphi) d\varphi = -I_C \frac{\Phi_0}{2\pi} \cos(\varphi)$$

The Lagrangian now reads

$$\mathcal{L} = \frac{1}{2}C\dot{\Phi}^2 + I_C \frac{\Phi_0}{2\pi} \cos(\varphi)$$

and therefore the Hamiltonian

$$\mathcal{H} = \frac{1}{2}C\dot{\Phi}^2 - \left( \frac{1}{2}C\dot{\Phi}^2 + I_C \frac{\Phi_0}{2\pi} \cos(\varphi) \right) = 4E_C n^2 - \underbrace{I_C \frac{\Phi_0}{2\pi}}_{E_J} \cos(\varphi)$$

$$\boxed{\mathcal{H} = 4E_C n^2 - E_J \cos(\varphi)} \quad (11)$$

Considered in more detail, the junction itself also has a small capacitor. The capacitance in  $E_C$  is therefore a combination of the shunt capacitance  $C_S$  and the self-capacitance of the junction  $C_J$ ,  $C_\Sigma = C_S + C_J$ , as illustrated in fig. 5 (c). The part  $I_C \frac{\Phi_0}{2\pi} =: E_J$ , with the critical current of the junction  $I_C$ , we name the Josephson energy  $E_J$ . The dynamics of this non-linear system depends on the dominant energy term in equ.11, reflected in the ratio  $E_J/E_C$ . [13]

In the phase basis this Hamiltonian can be solved exactly in terms of the Mathieu functions. The first three energy levels are plotted in fig. 6 as a function of the effective offset charge  $n_g$  for different ratios  $E_J/E_C$ . [14] If the charging energy dominates, the eigenstates of the Hamiltonian are approximately given by the eigenstates of the charge operator  $\hat{n}$ . The paraboles of this "quadratic in  $n$ " kinetic energy part of the Hamiltonian are shown in fig.6 (a). In this situation, where  $E_J \approx E_C$ , a change in the gate charge  $n_g$  has large influence on the transition frequency of the device, as the energy changes quickly with just small "fluctuations" in  $n_g$ . [15] The second term

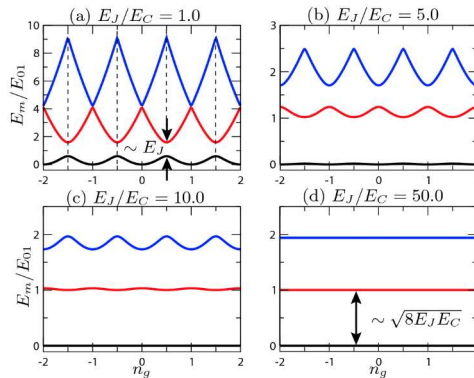


Figure 6: First three energy levels of the Hamiltonian (11) in units of the transition energy  $E_{01}$  as a function of the effective offset charge  $n_g$  for the ratios  $E_J/E_C = 1, 5, 10$  and  $50$ . With increasing ratio the energy levels flatten more and more until the region where  $E_J \gg E_C$  and they look like discrete levels, independent of the charge.[14]

of the Hamiltonian, coming from the Josephson junction, is "responsible" for the splitting of the



energy levels. It lifts the degeneracy. With increasing ratio of  $E_J$  to  $E_C$ , as we can see in fig.6 (b)-(d), the energy levels split more apart and their wiggles flatten out more and more.

Considering just the cosine-potential in equ.11, increasing  $E_J$  means higher amplitudes of the cosine. Higher amplitudes means higher potential walls for the particles living in the potential minima. Therefore the probability to hop over or tunnel through the potential to the next minima decreases. The states of the particle become localized in one of the minima.

In the regime where  $E_J \gg E_C$  the energy levels, again of the whole potential in fig.6, look like discrete levels. With the localized states in the periodic potential they can be treated as Bloch bands. They are independent of the charge, and are therefore quite insensitive to charge noise.[14]

One way to reach this  $E_J \gg E_C$  limit is to make  $E_C = \frac{e^2}{2(C_S + C_J)}$  small by shunting the junction with a big capacitance  $C_S \gg C_J$ . The circuit operated in this regime, is called a *transmon qubit*. In this limit, the superconducting phase  $\varphi$  is a good quantum number, i.e. the spread of  $\varphi$  values represented by the quantum wavefunction is small and therefore, as plotted in fig.5 (d) the low-energy eigenstates are, to a good approximation, localized states in the potential well.[13] Due to this approximation, that  $\varphi$  is small, we can expand the cos-term of the Hamiltonian into a power series

$$E_J \cos(\varphi) = -E_J + \frac{1}{2}E_J\varphi^2 - \frac{1}{24}E_J\varphi^4 + \mathcal{O}(\varphi^6).$$

We can neglect periodic boundary conditions and eliminate the  $n^2$  term of the Hamiltonian by a gauge transformation. Keeping the terms up to fourth order, the Hamiltonian can be seen as a harmonic oscillator with a quartic perturbation and can be written in form of a so called *Duffing oscillator*

$$H = \sqrt{8E_CE_J}(\hat{b}^\dagger\hat{b} + \frac{1}{2}) - E_J - \frac{E_C}{12}(\hat{b} + \hat{b}^\dagger)^4$$

with the annihilation and creation operators  $\hat{b}$  and  $\hat{b}^\dagger$ . Solving this eigenvalue problem in first-order correction of the quartic term leads to the  $m^{th}$  eigenenergy [14]

$$E_m \approx -E_J + \sqrt{8E_CE_J} \left( m + \frac{1}{2} \right) - \frac{E_C}{12} (6m^2 + 6m + 3). \quad (12)$$

To get a feeling how this energy levels look like, let's write out the energy terms for the first four states.

By setting  $m = 0$  we get all the constant parts of the energy

$$E_0 = -E_J + \frac{1}{2}\sqrt{8E_CE_J} - \frac{E_C}{4}.$$

To simplify the equation we can define our zero point at this energy and set  $E_0 = 0$ . We are then left with

$$E_m \approx -\sqrt{8E_CE_J}m - \frac{E_C}{2}(m^2 + m) \quad (13)$$

Therefore the first energy levels of this now anharmonic oscillator read

$$\begin{aligned} E_1 &= \sqrt{8E_CE_J} - E_C \\ E_2 &= 2\sqrt{8E_CE_J} - 3E_C \\ E_3 &= 3\sqrt{8E_CE_J} - 6E_C \\ E_4 &= 4\sqrt{8E_CE_J} - 10E_C \end{aligned}$$

Comparing the energies of the harmonic oscillator with this energies of the anharmonic oscillator we see, that the difference doesn't grow linearly. It is represented by the number of  $E_C$ s subtracted from the harmonic oscillator energies. As a consequence, the energy difference of higher lying energy levels gets smaller and smaller, as shown in fig.5(d). In experiments normally the first two states are used as the qubit states. For those states the difference in energy between harmonic and anharmonic oscillator is one  $E_C$ . Expressed in frequencies ( $\omega = E/\hbar$ ) we get

$$\omega_{01} = \sqrt{8E_CE_J}/\hbar - E_C/\hbar.$$

Comparing this to equation (9) and defining  $\alpha := E_C/\hbar$ , it reads

$$\boxed{\omega_{01} = \omega_r - \alpha}. \quad (14)$$

$\alpha$  is called the *anharmonicity* of the qubit. It can also be defined just within the anharmonic potential, as the difference of the transition frequencies from  $E_1$  to  $E_2$  and from  $E_0$  to  $E_1$

$$\boxed{\alpha = \omega_{12} - \omega_{01}}. \quad (15)$$

In general we want a large anharmonicity to make the transition frequency of our qubit to the transition frequencies of the other levels more distinguishable. The more distinguishable they are, the shorter the microwave pulses to drive the qubit can be.[13] The limit is the condition  $E_J \gg E_C$  to get a Transmon, which still has to be fulfilled. In that sense we are limited by the fabrication where we can't make arbitrary small junctions to increase  $E_J$ .

"Be less curious about people  
and more curious about ideas."  
*Marie Curie*

## 5 Idea of the experiment

This section shows an overview of the experimental set up and the goal what we want to see, find and measure in this thesis. The chapter starts with the idea of the experiment and the set up. Followed by a short introduction to waveguides, how they work and how they can be used to measure qubits. In the end a short description of the working principle of a dilution refrigerator is given.

### 5.1 Experimental set up

The idea of this thesis is to get the fabrication in the new clean room running, fabricate single qubits, see how reproducible they are, cool them down and see how they fit to theory. In the previous chapters it was motivated why people in general are interested in fabricating superconducting qubits and how qubits can be described theoretically. In this chapter the additional experimental parts, the waveguide and the fridge, used to measure the fabricated qubits are introduced. For the fabrication of the qubits I refer to sec.10 where it is explained in more detail how to fabricate superconducting devices, especially qubits. The three main parts for the experiment are therefore the qubits fabricated on sapphire, shown in fig.7 (a), the waveguide where the qubit chips are mounted (fig.7 (b)) and the dilution refrigerator to cool down the whole system to temperatures of about 20 mK (bottom part of the refrigerator shown in fig.7 (c)).

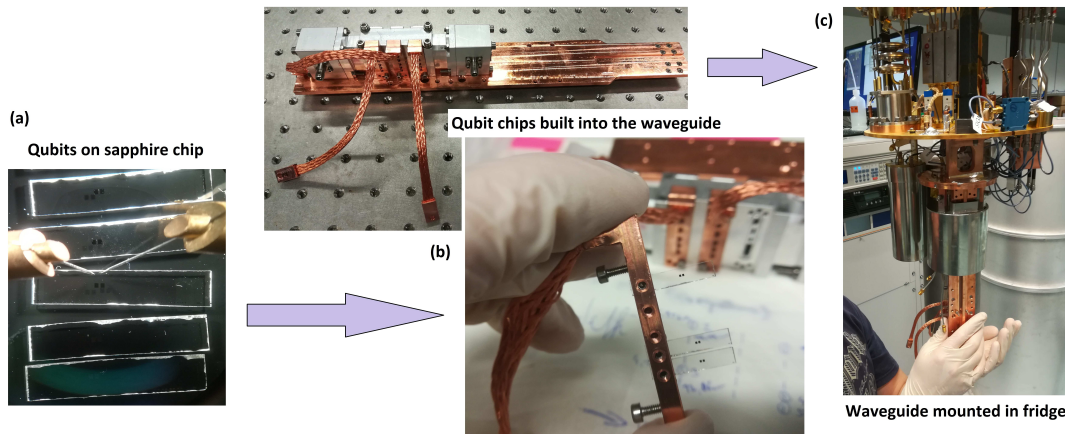


Figure 7: (a) The qubits fabricated on sapphire chips are shown under an optical microscope. (b) Shows how the chips are mounted in the used waveguide. (c) Bottom part of the open refrigerator where the waveguide is mounted.

### 5.2 Rectangular waveguide

One of the earliest transmission lines to transport microwave signals were rectangular waveguides. [16] The waveguide used to measure the qubits for this thesis is a rectangular waveguide. It was fabricated and used before for measurements to characterize stripline resonators. The documentation about this and the detailed waveguide parameters and dimensions can be found in [17]. Here I want to give a short summary of the working principle of a waveguide without qubits and why it is helpful to simulate the system 'waveguide with qubit', before fabricating the qubit.

### 5.2.1 Waveguide without qubits

Let's define the width of the waveguide in  $x$ -direction as  $a$  and the height in  $y$ -direction as  $b$ . In  $z$ -direction the length is not limited. The waves can therefore travel in  $z$ -direction, but are confined in  $x$ - and  $y$ -direction by the walls of the waveguide. Those are the boundary conditions which lead to just two types of electromagnetic waves that can propagate. Waves where the electric field component parallel to the waveguide is zero ( $\vec{E} = (E_x, E_y, 0)$  and  $\vec{B} = (B_x, B_y, B_z)$ ), the so called TE (transverse electric) modes, and waves where the parallel magnetic field component vanishes ( $\vec{E} = (E_x, E_y, E_z)$  and  $\vec{B} = (B_x, B_y, 0)$ ), the TM (transverse magnetic) modes. [18] In fig.8 the first modes for the possible waves are sketched in the  $x$ - $y$ -plane. The colours indicate the wave vectors pointing out of the plane and into the plane. For the red colour the waves come out of the plane and point in  $z$ -direction. For the blue colour the electric field is zero  $E = 0$ . For each mode

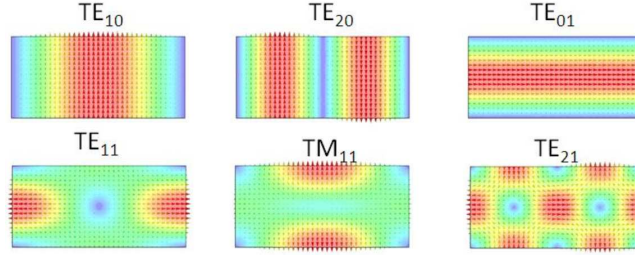


Figure 8: Distribution of the electric field in the  $x$ - $y$ -plane of the waveguide for the first 6 modes (sorted by their cutoff frequency). Picture taken from [19] and modified.

there exist a *cutoff frequency*  $f_c$ . Below  $f_c$  propagation is not possible. Only waves with frequencies  $f > f_c$  will propagate. Waves with frequencies  $f < f_c$  being below cutoff decay exponentially away from the source of excitation. In the TE case, the cutoff frequencies are given by

$$f_{c_{mn}} = \frac{1}{2\pi\sqrt{\mu\epsilon}} \sqrt{\left(\frac{m\pi}{a}\right)^2 + \left(\frac{n\pi}{b}\right)^2}$$

with each combination of  $n, m \in \mathbb{Z}$  representing one mode, the permeability of the material that fills the waveguide  $\mu$ , the permittivity of the material that fills the waveguide  $\epsilon$  and the waveguide dimensions  $a$  and  $b$ . The mode with the lowest cutoff frequency is called the *dominant mode*. In the case of TE modes this is the mode with  $m = 1$  and  $n = 0$ , the  $TE_{01}$ , and the cutoff frequency

$$f_{c_{01}} = \frac{1}{2a\sqrt{\mu\epsilon}}.$$

In the TM case, the lowest propagating mode is the  $TM_{11}$  mode with the cutoff frequency

$$f_{c_{11}} = \frac{1}{2\pi\sqrt{\mu\epsilon}} \sqrt{\left(\frac{\pi}{a}\right)^2 + \left(\frac{\pi}{b}\right)^2}.$$

One can see, that it is larger than the cut off frequency of the  $TE_{01}$  mode. The preferred mode for a wave propagating in a waveguide is therefore a TE mode. [16] In our case we want to design the qubits that way, that they can be measured within the first mode of the waveguide, the  $TE_{10}$  mode.

### 5.2.2 Waveguide with qubits

From the qubits point of view, the waveguide is the environment of the qubit. Interaction between the qubit and the waveguide can be achieved, if the waveguide provides a frequency that fits the resonance frequency of the qubit, or vis versa, if the resonance frequency of the qubit is within the propagating modes of the waveguide. The design of the waveguide with its cutoff frequency  $f_c$  has to match the designed qubit frequency  $f_{01}$ , such that  $f_{01} > f_c$ . For the qubit, the resonance frequency depends on  $E_C$  like  $f_{01} = \frac{1}{2\pi\hbar} (\sqrt{8E_J E_C} - E_C)$ . For  $E_C$  all possible capacitances of

the system have to be taken into account. For just the qubit this means the shunt capacitance  $C_s$  and the capacitance of the junction  $C_J$ . For the qubit in the waveguide it also depends on the capacitance that is provided by the walls of the waveguide  $C_{WG}$ . This capacitance depends on the position in the waveguide. With a simulation we can find the resonance frequencies of the qubit in the environment of the waveguide and can calculate the the capacitance with  $C = \frac{1}{L(2\pi f)^2}$ . This is the capacitance including the shunt capacitance and the capacitance from the waveguide  $C_{sim} = C_s + C_{WG}$ , as we didn't account a junction capacitance in the simulation. From the measured resonance frequencies of the qubit  $f_{01}$  and  $f_{12}$  ( $\alpha = f_{01} - f_{12} = E_C$ ) in the experiment we can also calculate a capacitance  $C = \frac{e^2}{2E_C}$ . This time it is the sum of all possible capacitances in the system  $C_\Sigma = C_s + C_{WG} + C_J$ . Comparing  $C_{sim}$  and  $C_\Sigma$  we can find the proportion of capacitance the junction itself provides. When designing a qubit for a particular resonant frequency, this capacitance should be taken into account.

In general one should have in mind, that the waveguide environment itself changes the energy levels of the qubit (like here:  $C_{WG} \rightarrow E_C \rightarrow f_{01}$ ). As we will see later, also the applied microwave tone couples to the qubit and leads to shifts of the energy levels, like the so called *Stark shift* or the *Lamb shift*.

### 5.3 Dilution Refrigerator

To cool down the samples to a few K we use a dilution refrigerator. The main principle of a dilution refrigerator is evaporative cooling of liquid helium. A "pot" in which the pressure is reduced to about 0,1 mbar is continuously fed with liquid helium from a main bath. The liquid helium evaporates in the pot. Due to the latent heat of the evaporated liquid cooling can be achieved. As shown in fig.9 (a) the temperature is limited by the exponentially decreasing vapour pressure. At very low pressure there are not enough molecules anymore to cool the pot further. With pumping

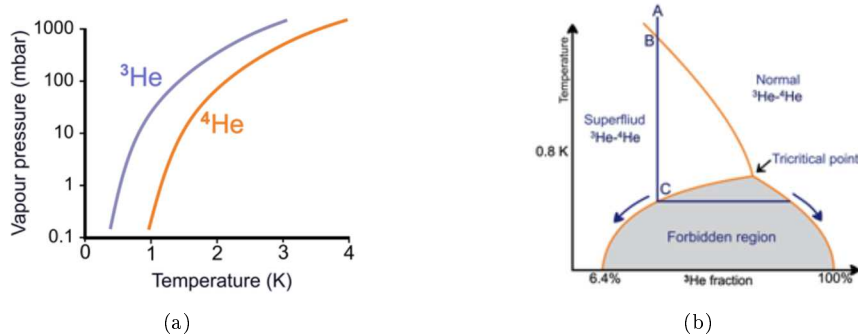


Figure 9: (a) Vapour pressure of helium against the temperature.  $^3\text{He}$  has much higher vapour pressure than  $^4\text{He}$  and can therefore reach lower temperatures. Picture taken from [20]. (b)

on  $^4\text{He}$  temperatures of about 1,2 K can be reached. This is already colder than the temperature in outer space of about 2,7 K. According to fig.9 (a) even lower temperatures of around 0,25 K can be reached by pumping  $^3\text{He}$ . The reason is the nuclear spin of the two molecules.  $^4\text{He}$  has a nuclear spin of  $I=0$ , follows the Boson statistics and reaches the transition to a superfluid at  $T=2,17$  K.  $^3\text{He}$  on the other hand has a nuclear spin of  $I=1/2$  and therefore follows the Fermi statistics. Due to the Pauli exclusion principle  $^3\text{He}$  reaches the superfluid transition, at which the spins pair up and obey Boson statistics, at much lower temperatures. Most of the time people use a mix of  $^4\text{He}$  and  $^3\text{He}$ . In the mixture of the two isotopes, the superfluid transition temperature depends on the  $^3\text{He}$  concentration. In fig.9 (b) the temperature is plotted against the fraction of  $^3\text{He}$ . Starting from point A where we have a normal  $^3\text{He}$ - $^4\text{He}$ -mixture, we can reach point B by cooling down the mixture. There the mixture becomes superfluid. Cooling the mixture even further, at some point (point C in fig.9 (b)) the mixture separates in two phases (indicated with the horizontal line starting from point C). One  $^4\text{He}$ -rich phase which always contains minimum 6,4%  $^3\text{He}$  all the way down to 0 K and the  $^3\text{He}$ -rich phase. The  $^3\text{He}$  rich phase floats on the heavier  $^4\text{He}$  rich phase. [20] At the *tricritical point* we can see, that  $^4\text{He}$  superfluidity terminates for  $^3\text{He}$  concentrations higher

than 67,5%. Below this point just mixtures for particular concentrations of the two isotopes are possible. The region with the concentrations that are not miscible is called the *forbidden region*, indicated in gray in fig.9 (b). [21]

"You can never solve problems with the  
same mindset that created them."  
*Albert Einstein*

## 6 Simulation of the qubits in the waveguide

This section gives a quick summary of the simulation that was done. In the next chapter the theory explained so far will be filled with some numbers resulting from this simulation. With this numbers we can see how to estimate if the designed qubit is going to work in the used waveguide.

### 6.1 Simulation set up

The simulation was done with the program HFSS (High Frequency Structure Simulator). The waveguide was modelled as a box with the dimensions 23 x 20 x 11 mm in X-, Y- and Z-direction (see fig.10). The Y-dimension represent the length of the waveguide. It is not the real size of

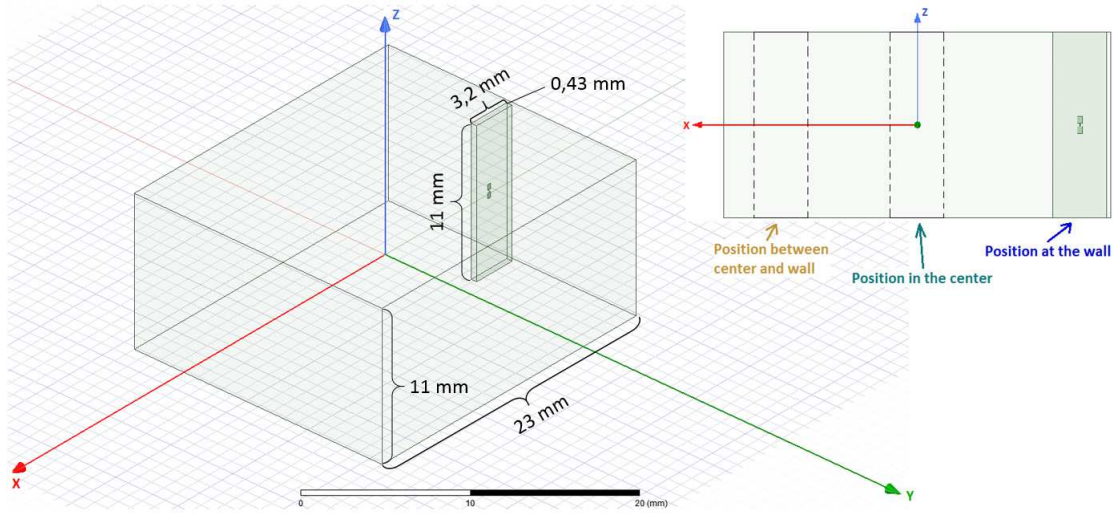


Figure 10: Model for the simulation. On the right the three positions of the qubit chip relative to the wall are sketched.

the waveguide, but for the applied 'Eigenmode'-simulation, we need two walls at each side of the input and the output. This "additional" walls lead to additional modes which are "artefacts" in this simulation and not "real" things that we can find in the measurements. The other dimensions correspond to the real dimensions of the inside wall of the used waveguide. More details about the waveguide can be found in [17]. On top of the waveguide there are slots at different positions to put the qubit chip inside. The different distances to the walls of the waveguide, lead to different coupling strengths. The simulation was done for one qubit chip in the waveguide for three different distances to the wall, shown in fig.10. From the results we can see how the positions change the resonance frequency.

The dimensions of the waveguide, the dimensions of the qubit chip, in this case a sapphire chip, and the dimensions of the qubit itself are summarized in tab.1. The qubit parts are modelled as 2D "sheets", set as perfect conductors of the electrical field. The junction is modelled as a lumped element with an inductance  $L_j$ . For each position of the qubit chip, the simulation sweeps the inductance from 3 nH to 7 nH with a stepsize of 0,2 nH, and finds the corresponding resonant frequencies. In fig.11 the first three Eigenmodes of the system, simulated for the three qubit positions in the waveguide, shown on the right in fig.10, are plotted. The blue line corresponds to the qubit placed directly next to the waveguide wall, the green line shows the Eigenmodes of the qubit placed in the center of the waveguide and the orange line is the result for a qubit placed at a position 2 mm away from the waveguide wall. The second mode whose resonance frequency decreases with increasing inductance, corresponds to the qubit. The other two modes are no real

Table 1: Dimensions of the simulated qubit on a sapphire chip in a waveguide. The waveguide is modelled as a box with the dimensions given in this table.

	Waveguide	Sapphirechip	Qubit
(Pad) Height	11 mm	11 mm	400 $\mu\text{m}$
(Pad) Width	23 mm	3,2 mm	300 $\mu\text{m}$
Length/Thickness	20 mm	0,43 mm	"sheet"
Pad Distance	\	\	200 $\mu\text{m}$
Lumped element dimensions	\	\	200 x 10 $\mu\text{m}$
Inductance Sweep $L_J$	\	\	3-7 nH

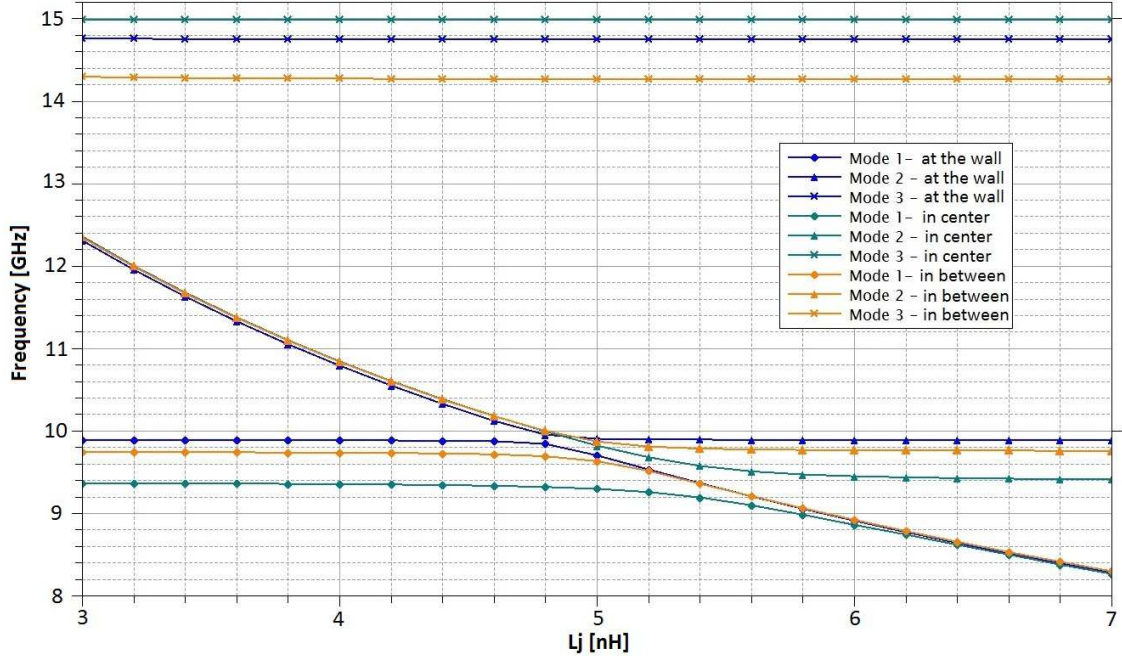


Figure 11: First three resonant modes of the simulated waveguide-qubit-system for three different positions of the qubit in the waveguide. One position is at the wall, a second is in the center of the waveguide and a third one is located 2 mm away from the waveguide wall.

modes. They are the "artificial" modes coming from the confinement in y-direction. What we can see is, that when the energies of the qubit and the virtual waveguide mode come close to each other or reach resonance, the energies shift. In fig.11 this so called *avoided crossings* for the qubit and the first artificial mode is visible for the three different positions of the qubit in the waveguide.



"If I have seen further than others  
it is only because I stood  
on the shoulders of giants"  
*Isaac Newton*

## 7 From Theory to Fabrication

This section gives an overview of the parameters coming from theory to create a working qubit and translate them to design and fabrication parameters. In the second part a numerical example to find the right parameters is given.

### 7.1 Qubit Parameter

With all the theory in the back of our mind we can now think of what properties we want from our qubit and how we can achieve them. How should we design our qubits to get the right parameters so that we can measure them in a waveguide or cavity?

In fig.12 the circuit diagram of the anharmonic circuit and how it can be translated into the qubit design, is shown. The green and the dashed red line indicate the inductance and capacitance of the

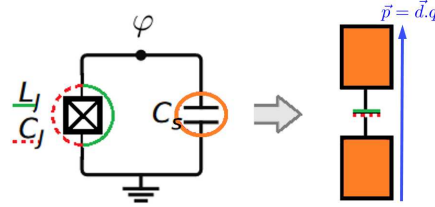
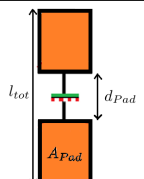


Figure 12: Schematics of how the electrical circuit with the Josephson junction can be translated into the design of a qubit. The pad widths and the distance between them define the shunt capacitance  $C_S$  (red line). The junction itself defines the nonlinear inductance  $L_J$  (green line) and is also as a small capacitor with the capacitance  $C_J$  (red dashed line). The length of the whole qubit, marked with the blue arrow, acts as a dipol which defines the coupling of the qubit to the electric field in the waveguide.

Josephson junction. The orange colour marks the shunt capacitance. By changing these elements in the qubit design we change the inductance and capacitances in the circuit and therefore the resulting energies of the system. We can think for example about the size of the qubit pads  $A_{Pad}$  and their distance  $d_{Pad}$  to tune the shunt capacitance. In addition the total length of the qubit  $l_{tot}$  act as a dipol and plays a role in the coupling to the waveguide. The size of the junction area has an influence on the inductance  $L_J$  and contributes with a small capacitance  $C_J$  to the total capacitance. Those parameters, and how to change them, are summarized, together with the oxidation parameters from the fabrication process (see sec.9.4.1), in tab.2.

However, to build a Transmon, we can't arbitrarily change the energies. As we saw in section 4.2,

Table 2: Parameter to tune the qubit.

Design and fabrication parameter		Affected qubit parameter	
Pad distance	$d_{Pad}$	$C_s$	
Pad size	$A_{Pad}$		
Total length	$l_{tot}$	Coupling to WG	
Junction area	$A$	$\frac{1}{A} \propto R_n \propto L_J$	
Oxidation in fab.	$t_{ox}, p_{ox}$	$(t_{ox} \cdot p_{ox})^x \propto R_n$	

the condition to reach the Transmon limit is  $E_J \gg E_C$ , or more concrete  $\frac{E_J}{E_C} > 50$ , according to [14]. From the formula of the resonant frequency of the harmonic oscillator  $\omega_r = \frac{1}{\hbar} \sqrt{8E_J E_C}$  one

can rewrite this condition in terms of  $E_C$  and get

$$\frac{E_J}{E_C} = \frac{\hbar^2 \omega_r^2}{8E_C^2} > 50 \rightarrow \frac{\hbar^2 \omega_r^2}{E_C^2} > 400 \rightarrow \frac{\hbar \omega_r}{E_C} > 20 \rightarrow \boxed{\frac{\hbar \omega_r}{20} > E_C} \quad (16)$$

The "new" condition now is, that the resonance frequency divided by 20 has to be larger than  $E_C \approx \alpha$ .

In addition to a simulation, a tangible value which can directly be compared to the fabrication parameters and enables a look at the qubit parameters, even before cooldown, is the normal state resistance  $R_n$ . In fig.13 the measured normal state resistances for different design and fabrication parameters of the qubits are plotted. The area of the junctions scales indirect proportional to

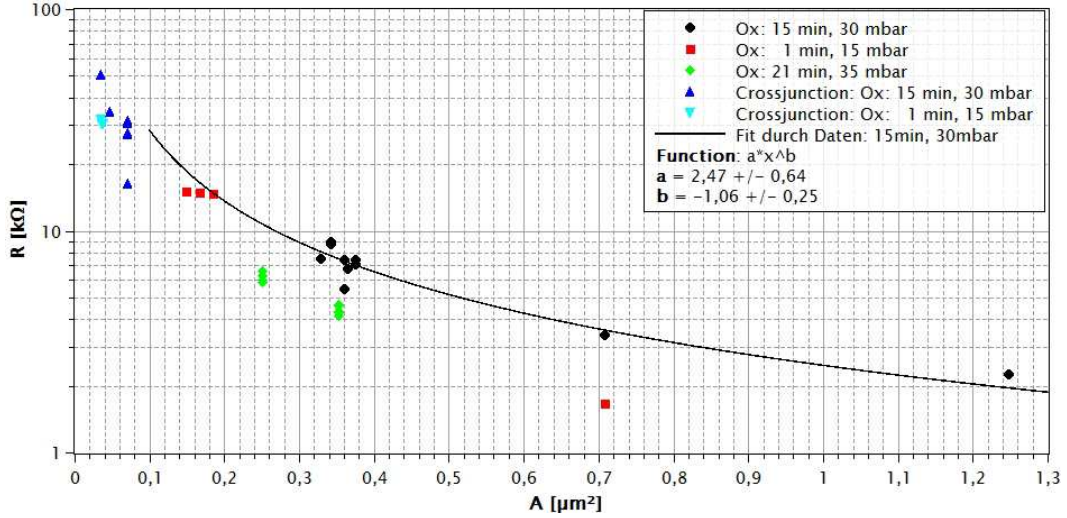


Figure 13: Junction areas of different qubit batches and their normal state resistances. The fit line ( $y = (2,47 \pm 0,64) \cdot x^{(-1,06 \pm 0,25)}$ ) represents the  $\frac{1}{A}$  dependency of the resistance  $R_n$ .

the resistance. A bigger junction area leads to a smaller value for the resistance and a smaller inductance of the junction.

To make the connection between the resistance  $R_n$  and the inductance of the junction  $L_J$  we can start with two relations for the critical current. One from the comparison of the linear inductor term  $E_L = \frac{1}{L} \left( \frac{\Phi_0}{2\pi} \right)^2$  (see equ.(8)) and the anharmonic inductor term  $E_J = I_C \frac{\Phi_0}{2\pi}$  (see equ.(11)), which leads to a connection between critical current and inductance

$$I_C = \frac{\Phi_0}{2\pi L}.$$

On the other hand we can use the Ambegaokar-Baratoff formula (see equ.4), which connects the critical current with the normal state resistance

$$I_C = \frac{\pi \Delta}{2e} \frac{1}{R_n} \cdot 0,87. \quad (17)$$

By combining those formulas we find the equation

$$R_n = \frac{\pi \Delta}{2e} \cdot 0,87 \cdot \frac{2\pi L_j}{\Phi_0}.$$

Collecting all the constant parameters to a value  $\beta$

$$R_n = \underbrace{\frac{0,87\pi^2\Delta}{e\Phi_0}}_{\beta} \cdot L_j \quad (18)$$

and calculating  $\beta = 847 \cdot 10^9$  1/s, we find the linear connection between the normal state resistance and the inductance of the junction

$$R_n [k\Omega] = 0.847 \left[ \frac{1}{s} \right] \cdot L_j [nH] \quad (19)$$

The values of the constants in the Ambegaokar-Baratoff formula are  $e = 1,602 \cdot 10^{-19}$  C ,  $\Phi_0 = 2,068 \cdot 10^{-15}$  Wb and the band gap is chosen to  $\Delta = 2,04 \cdot 10^{-4}$  eV (this is a value the group of Ioan Pop measured at KIT). For the aluminium we are using we haven't measured the band gap directly so far, but we determined the value for the product  $\Delta \cdot 0,87$  from equ.17. In section 11.3.2 fig.81 we plotted  $I_C$  against the normal state resistances and got  $\Delta \cdot 0,87 = 1,966 \pm 0,073 \cdot 10^{-4}$  eV. Trusting the constant value 0,87 we get a band gap of  $\Delta = 2,26 \pm 0,08 \cdot 10^{-4}$  eV.

## 7.2 Numbers for a simulated qubit

Let's say we want to fabricate a qubit that works at about 8 GHz, as the waveguide has its usable frequency range around 8 GHz. According to the simulation (see fig.11), we therefore need an inductance of about 7 nH. The resonant frequency of the qubit mode at 7 nH, resulting from the simulation is  $f_1 = 8,28$  GHz.

The simulation doesn't solve for the real system, with the nonlinear Josephson junction and the therefore anharmonic potential, but for a harmonic oscillator. As we saw in theory, the difference in the energy levels of the harmonic and the anharmonic potential can be "corrected" by  $E_C$ . By knowing  $E_C$  we can recalculate the resonance frequency of the real system. For  $E_C = \frac{e^2}{2C_\Sigma}$  we first need to know the capacitance

$$C_\Sigma = \frac{1}{L_j(2\pi f_1)^2} = \frac{1}{7 \cdot 10^{-9}(2\pi \cdot 8,28 \cdot 10^9)^2} = 52,78 fF$$

and can then calculate

$$E_C = \frac{(1,602 \cdot 10^{-19})^2}{2 \cdot 52,78 \cdot 10^{-15}} = 366,9 MHz.$$

We can check, if this value for  $E_C$  would lead to a Transmon, with the condition (16)

$$\frac{8,28 GHz}{20} > 366,9 MHz \rightarrow 414 MHz > 366,9 MHz.$$

The condition is therefore fulfilled and we can proceed with these parameters. The resonance frequency of the anharmonic qubit can, according to equ.14, be expected to be

$$\omega_{01} = 7,91 GHz.$$

From equation 19 we know what the resistance of the qubits at room temperature should be

$$R_n = 0.847 \frac{k\Omega}{nH} \cdot L_j = 5,93 k\Omega.$$

From the graph in fig.13 we can get a first guess for the parameters that need to be used in the fabrication. We can see what the junction area  $A$  should be and what to choose for the oxidation parameters, pressure  $p_{Ox}$  and time  $t_{Ox}$ , to create the tunnel barrier of the junction. More about this in sect.9.4.1. For a resistance of about 6 k $\Omega$  this could be for example  $A = 0,25 \mu m^2$ ,  $p_{Ox} = 35$  mbar and  $t_{Ox} = 21$  min.

"What really matters is intuition."  
*Albert Einstein*

## 8 Different ways to fabricate Josephson junctions

Before starting with the fabrication of qubits, this section gives a quick overview of the most common designs of Josephson junctions that are used for patterning the structures with an electron-beam. The first part explains the so called *Dolan-Bridge junction*, followed by the *Bridge-free junction* where one also can find some calculations for the angle under which the junction should be evaporated. The last part shortly introduces a very simple design to create Josephson junctions, the so called *Crosstype junctions*.

### 8.1 Dolan-Bridge junction

For completeness I also describe here the Dolan-Bridge technique to create a Josephson junction, although I never used this technique for the junctions so far.

As the name indicates, for a junction fabricated with the Dolan-Bridge technique, the evaporation mask includes a bridge. In fig.14 ii) the bridge is shown from a side view. This suspended bridge is used to disconnect the two evaporated superconducting layers of the junction from each other. To create the undercut structure of the bridge, two different polymer layers with different sensitivities to the electron-beam are used. In fig.14 this is indicated with the orange and gray layers. After the lithography the layers of superconducting material are evaporated in the pattern. They come from two different angles and the junction builds up under the bridge (see fig.14 iii)-vi)). Some say, that

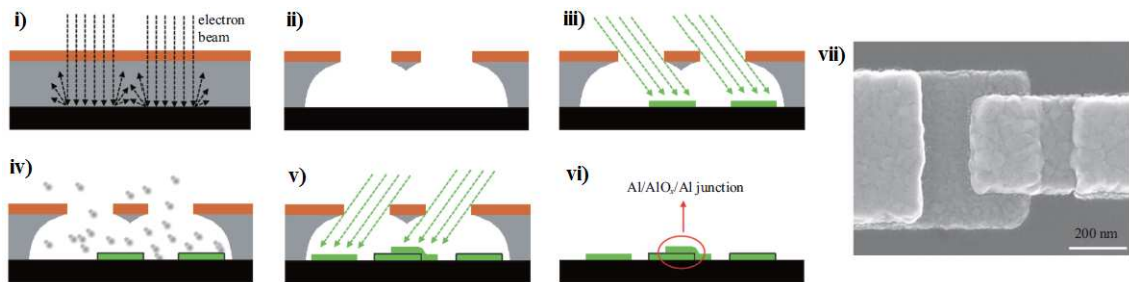


Figure 14: In i)-vi) the fabrication steps for a Dolan-Bridge junction are shown. The pictures are taken from [22]. They used a layer of PMMA/MA (polymethyl methacrylate/methacrylate), coloured in gray, and on top a layer of PMMA (orange). i) shows the electron beam lithography step where the design is written in the polymer. ii) shows the resulting evaporation mask after developing. In iii) the first evaporation is shown. Followed by an oxidation step in iv) and the second evaporation of aluminium shown in v). In vi) the junction after the lift off is marked with the red circle. In vii) a top view of the junction under an electron microscope is shown.

this is one advantage of the Dolan-Bridge technique, that the junction is protected by the bridge from for example falling dirt etc. Fabrication wise the Dolan-Bridge mask has its advantages in the insensitivity to exact undercuts. It therefore is less sensitive to dose variations, compared to the bridge free technique where the defined undercut is an important parameter to get a working junction. For the Dolan-Bridge the junction should work, as long as a suspended bridge is created and stable enough to not collapse during the fabrication process. In fig.14 vii) the top view of a Dolan-Bridge junction under the microscope is shown.

### 8.2 Bridge-free junction

The junctions fabricated during my master thesis are nearly all fabricated with the Bridge-free technique. The principle is similar to the Dolan-Bridge. A mask of two polymer layers with different sensitivities to the electron beam is coated by e-beam evaporation with a superconducting material from two angles. The procedure steps are summarized in fig.15. In ii) the design for the

junction is shown. The difference to the Dolan-Bridge is to avoid the suspended bridge. This has the disadvantage of higher sensitivity to dose variations. The undercut, created at the locations of the cables, and the evaporation angle have to fit quite well to each other. For the Dolan-Bridge the junction is evaporated into the undercut. For the Bridge-free junctions, the connecting wire from the junction to the pads is evaporated into the undercut, the junction area is not covered at all. Therefore a better cleaning of the junction area can be achieved in the bridge free case. Another advantage of the Bridge-free technique is the easier size scaling of the junctions compared to the Dolan-Bridge technique. A good control, knowledge and characterization of the doses for different polymers, thicknesses and designs is advantageous to quickly get good results.

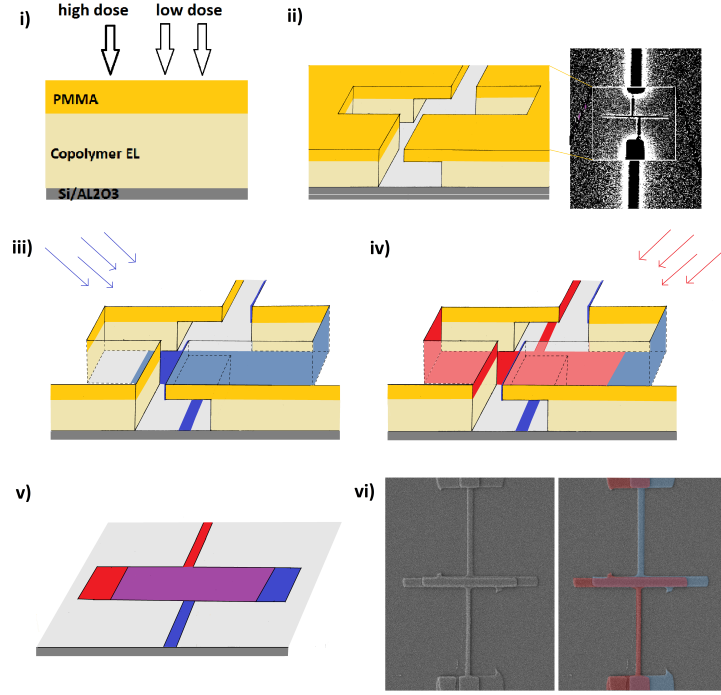


Figure 15: i) The two polymer layers are already spincoated on the substrate, here silicon (Si). With different doses during the electron beam lithography an undercut can be created at the locations of the cables. In ii) the resulting mask after developing is shown. On the left a cut through the mask near the junction area is shown. On the right a top view of the junction area after developing is shown under an e-beam microscope. In iii) the first aluminium layer evaporated under an angle  $\Theta$  with one connecting cable on the substrate and the other one on the polymer wall is sketched. iv) shows the second aluminium layer, after oxidation, evaporated under an angle  $-\Theta$ . In v) the final junction after the lift off is sketched. The purple area indicates the effective junction area. In vi) you can see the final junction imaged with the e-beam. On the left there is the original picture and on the right one can see the same picture with false coloured aluminium layers. The picture is taken with the parameters: magnification (Mag) = 16.24 Kx, acceleration voltage (EHT = Extra High Tension) = 2.00 kV, working distance (WD) = 9.6 mm, Signal = SE2, Aperture Size = 30  $\mu\text{m}$ .

### 8.2.1 How to find the right evaporation angle in the example of a Bridge-free junction

In fig.16 the mask of a bridge free junction is sketched. The dimensions of the undercut are labelled. The height of the Copolymer layer  $h$ , the height of the PMMA layer  $g$ , the designed width of the trench  $d$ , the designed width of the undercut  $u$  and the total width of the designed area  $s$  on the substrate to evaporate on. With this values one can calculate how the evaporation angle should be chosen and how wide the evaporated cable  $x$  would be in the end.

Let's start with two situations that define your minimal evaporation angle  $\alpha_{min}$ . Your evaporation

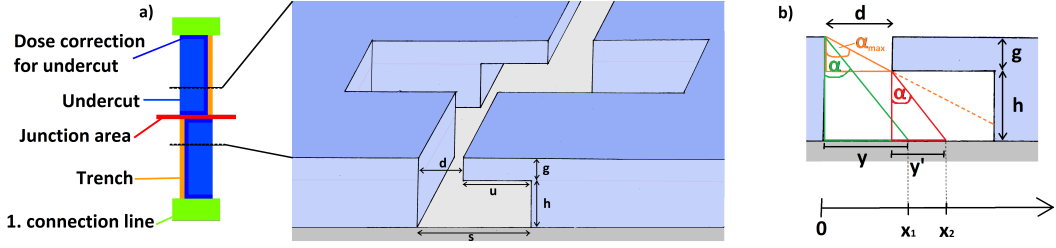


Figure 16: In a) the junction part of the design and a labelled schematic of the evaporation mask of a Bridge-free junction in 3D, are sketched. The colours in the design indicate the different dose factors for the e-beam lithography. In b) you see a cross-section of the undercut part of the mask and the possible evaporation angles.

angle needs to be larger than this to avoid an extra cable. Furthermore, you can determine your  $\alpha_{max}$ , the angle at which everything is evaporated onto the undercut overhang and nothing on the substrate anymore. In fig.17 a) these two situations are illustrated. With simple geometry one finds the relations

$$\alpha_{max} = \arctan\left(\frac{d}{g}\right)$$

and

$$\alpha_{min} = \arctan\left(\frac{d}{g+h}\right)$$

In fig. 17 b) two situations in which the evaporation angle is chosen between  $\alpha_{min}$  and  $\alpha_{max}$

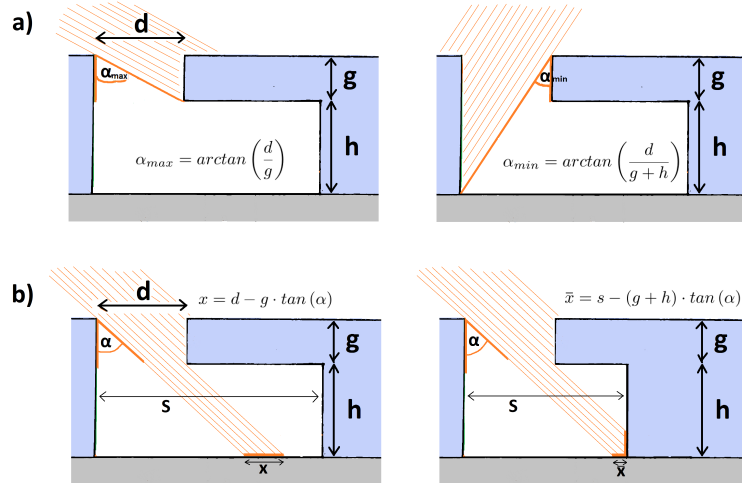


Figure 17: Situations for the evaporation process which can be seen as the boundary conditions for a working junction. In a) the maximal and minimal angles, for the aluminium evaporation, are shown. To get a working junction the evaporation angle must be chosen between this  $\alpha_{min}$  and  $\alpha_{max}$ . In the picture on the left in b) the situation when everything is set correctly is shown and the formula to calculate the width of the cable  $x$  is given. In the picture on the right the undercut is not deep enough and the cable is partially evaporated onto the wall. Therefore the cable is narrower than in the optimal case. Also the formula to calculate this width of the cable  $\bar{x}$  is given.

are sketched. On the left, the thickness of the evaporated cable  $x$  for a given angle  $\alpha$  can be calculated using the red and green triangle in fig.16 (b). It's defined as the difference between the positions  $x_2$  and  $x_1$  indicating the borders of the evaporated "beam" of Al reaching the substrate under an angle  $\alpha$ . On the right hand side of fig.17 b) the undercut is a bit too small

so that the cable is evaporated only partially onto the substrate. The width of the evaporated cable is therefore smaller than expected. From the geometry one can extract the following relations:

<p><b>green triangle:</b> (see fig.16 (b))</p> $\tan(\alpha) = \frac{y}{g+h}$ $x_1 = y = (g+h) \cdot \tan(\alpha)$	<p><b>red triangle:</b> (see fig.16 (b))</p> $\tan(\alpha) = \frac{y'}{h}$ $y' = h \cdot \tan(\alpha)$ $x_2 = d + y'$
--	---

For the thickness of the cable  $x$ , on the wafer ( $x_2 < s$ ), you get the relation

$$x = x_2 - x_1 = d - g \cdot \tan(\alpha) \quad (20)$$

For the 2<sup>nd</sup> case in fig.17 b), where the undercut is not wide enough to evaporate the whole cable onto the wafer ( $x_2 > s$ ), you set  $x_2 = s$  and the relation for the thickness of the cable then reads

$$\tilde{x} = s - x_1 = s - (g+h) \cdot \tan(\alpha) \quad (21)$$

The maximum angle that can theoretically be reached, without evaporating on the wall ( $x_2 = s$ ), can be calculated with

$$\alpha_{x_2=s} = \arctan\left(\frac{s-d}{h}\right). \quad (22)$$

Cables evaporated under an angle smaller than this, have to be calculated with equ.20. Cables evaporated under an angle bigger than  $\alpha_{x_2=s}$  have to be calculated with equ.21.

If you measure a cable size smaller than the value you get from equ.20, your undercut is with high probability too small or your angle is too big for this undercut.

In the fabrication process the designed lengths and widths are most likely not exactly the ones that come out in the end. Due to backscattered electrons in the e-beam lithography and the proximity effect (more about this in section 9.2), the edges of the design could be washed out a bit. On the one hand this can be positive, because you have a bit wider range for your angle before the cable is evaporated on the undercut wall, but on the side without the undercut it makes it more likely to evaporate a second undesired cable onto the substrate because the wall is washed away a little bit.

To give some numbers, let's calculate the angles and cable widths for our qubit design. In tab.3 the parameters from the design and from measurements are given. The heights of the polymers  $h$  and  $g$  are measured with a profilometer. The widths of the trench  $d$  and the undercut  $u$  are taken

Table 3: Table with the dimensions and parameters of our junction to give an example for the formulas presented in this chapter.

Given parameters:		Calculated parameters:	
$\alpha$	30° (30°)	$\alpha_{max}$	36,87° (51,34°)
$d$	150 (250) nm	$\alpha_{min}$	11,77° (19,15°)
$h$	520 (520) nm	$\alpha_{x_2=s}$	53,39° (49,09°)
$g$	200 (200) nm	$x_1$	415,69 (415,69) nm
$u$	0,7 (0,6) $\mu$ m	$x_2$	450,22 (550,22) nm
$s$	850 (850) nm	$x$	<b>34,53 (134,53) nm</b>
		$\tilde{x}$	434,31 (434,31) nm

from the design (in more detail presented in section 10.7.1, fig.69), and are in our case  $d = 150$  nm and  $u = 0,7 \mu$ m. The parameter  $s$  calculates from the trench width  $d$  and the undercut  $u$ . The evaporation angle  $\alpha$  is 30°. All the other parameters, the angles  $\alpha_{max}$ ,  $\alpha_{min}$ ,  $\alpha_{x_2=s}$  and the distances  $x_1$ ,  $x_2$ ,  $x$  and  $\tilde{x}$  are calculated with the formulas given before. In brackets the numbers for the same junction with a 100 nm wider trench are given.

For these numbers, the condition  $x_2 < s$  is fulfilled and also the angle  $\alpha$  lies between  $\alpha_{min}$  and  $\alpha_{max}$ . Therefore the cable width calculated with equ.20 is expected to be  $x = 34,53$  nm. Due to the much larger angle  $\alpha_{x_2=s} = 53,39^\circ$  than  $\alpha_{max} = 36,87^\circ$ , it can be concluded, that the undercut

is much bigger than needed.

If we measure the cable widths of the fabricated junctions under the electron beam microscope with the included measuring tool in the Raith software, we get a mean value of  $153 \pm 22$  nm for the first evaporated cable and a value of  $123 \pm 21$  nm for the second cable. The difference of the two cable widths is  $30 \pm 15$  nm. This is due to the thickness of the first evaporated layer. It seems that theory and measurements doesn't fit together very well. But one has to have in mind, that this calculations are done with the design dimensions of the junctions. If we for example make  $d$  about 100 nm wider and therefore the undercut about 100 nm smaller, we get the values given in brackets in tab.3. For  $x$  we now get 134,53 nm, which is much more comparable to the measurements. With a bit too much dose it can happen easily that the trench in the mask is wider than designed.

To illustrate the evaporation angles and the distances on the wafer, for the given dimensions of the polymer layers and the designed trench in tab.3, they are plotted against a varying undercut width  $u$  in fig.18. In the first plot, we can see the values for  $\alpha_{max}$  and  $\alpha_{min}$  and the angle  $\alpha_{x_2=s}$ , at

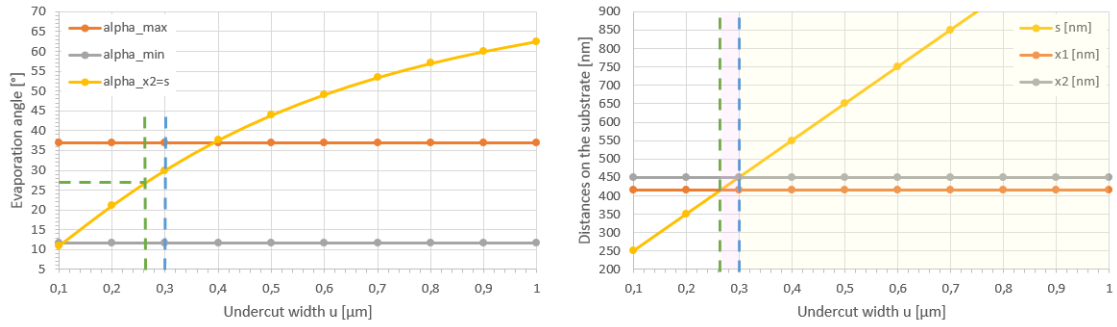


Figure 18: Plots to show how the evaporation angle and the design of the junction and the undercut play together to get a working junction and how the widths of the cables can be calculated. The dimensions are taken from tab.3. On the left  $\alpha_{max}$ ,  $\alpha_{min}$  and the angle at which the evaporation starts reach the polymer wall  $\alpha_{x_2=s}$  are plotted for different undercut widths  $u$ . For angles between the orange and the gray line ( $\alpha_{max}$  and  $\alpha_{min}$ ) the evaporated cables reach the substrate and we get a working junction. In the plot on the right the distances of the two edges of the cable from the polymer wall, as sketched in fig.16 b) ( $x_1$  and  $x_2$ ) and the whole distance to the undercut wall  $s$  are plotted for different undercut widths  $u$ . The distance between the orange and gray line therefore shows the width of the cable. The blue dashed line indicates the point where the cable is evaporated just next to the undercut wall ( $x_2 = s$ ). On the right hand side of this point, the area coloured in yellow, the width of the cable calculates with equ.20. For the small area, coloured in pink, on the left hand side of this point the cable width calculates with equ.21. The green dashed line indicates the point from where on the whole cable is evaporated onto the undercut wall. For smaller undercut widths (white area) the junction doesn't work because no cable is evaporated on the substrate.

which the cable is evaporated directly adjacent to the undercut wall. This angle  $\alpha_{x_2=s}$  grows with increasing undercut  $u$ . The point where it "crosses" the angle  $\alpha_{max}$  is the upper limit for a working junction. Above this point the junctions aren't working because all of the aluminium is evaporated onto the undercut overhang (see fig.17 a)). In between  $\alpha_{max}$  and  $\alpha_{min}$  there are three possibilities how the cable could be evaporated. First, the whole cable is evaporated on the substrate. This is the case where all the designed widths and lengths fit to the evaporation angles and the result comes out as expected. Second, just a part of the cable is evaporated on the substrate and the other part is evaporated onto the polymer wall. This case is sketched in the picture on the right in fig.17 b). The last thing that can happen is, that the whole cable is evaporated onto the polymer wall. In this case the junction isn't working because there is no cable to connect the junction area with the pads.

Let's chose an angle of  $30^\circ$ . From the left plot in fig.18 we can see that the minimum required undercut to evaporate the whole cable on the substrate is  $0,3 \mu\text{m}$ , as marked with the blue dashed line. Drawing this line also in the plot on the right of fig.18, it is exactly at the point where  $s = x_2$ , as expected. For undercut widths on the right hand side of this point, the width of the cable



calculates with equation 20 (yellow marked area). On the left hand side of this point there is a small area, marked with pink, at which the undercut is a bit too small. The cable is just partially evaporated on the substrate. There the width of the cable can be calculated with equ.21. For even smaller undercuts, indicated by the white area in the plot, the whole cable is evaporated on the undercut wall and no cable reaches the substrate.

### 8.3 Crosstype junction

A crosstype junction, compared to the Dolen-bridge and the Bridge-free junction, is easy to fabricate because no undercut is needed. Therefore just one polymer layer for the mask is enough. As shown in fig.19, for the crosstype junction you need to evaporate the two layers of the junction under an angle of  $90^\circ$  with respect to each other, to get separated connecting wires for the different layers. In the region where the "cables cross" the evaporated layers on top of each other create the junction area. With this crosstype technique it is possible to fabricate very small junctions.

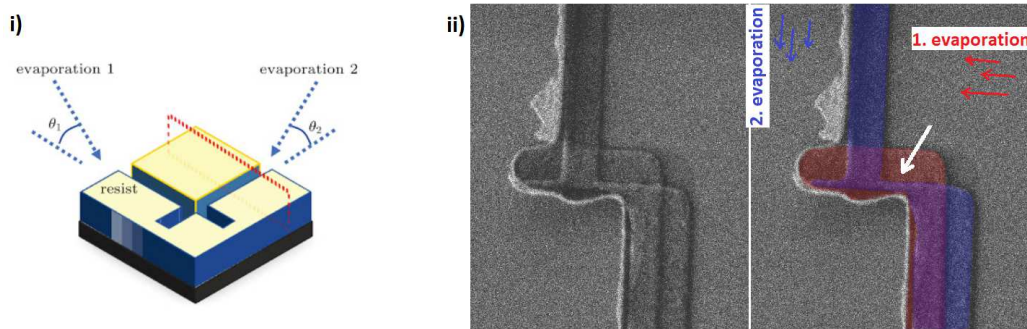


Figure 19: In i) an evaporation mask for the crosstype junction is sketched. The picture is taken from [23]. For this junction no second layer for an undercut is needed. The two aluminium layers are evaporated under an angle of  $90^\circ$  with respect to each other. In ii) one of the first tries to fabricate such a crosstype junction is shown. The picture was taken with the parameters: Mag = 35.65 Kx, EHT = 1.00 kV, WD = 6.6 mm, Signal = SE2, Aperature Size =  $30 \mu m$  under an e-beam. On the left one can see the original picture and on the right with false coloured layers. The red layer indicates the aluminium from the first evaporation and the blue layer indicates aluminium from the second evaporation. The purple area is the area where two layers of aluminium were evaporated. For a working junction each layer has to be connected just from one side. This is not the case for this junction, as the second layer is also connected to the blue coloured line going downwards, as marked with the white arrow. It is therefore shorted and doesn't work.

"The universe can create itself out of nothing."  
*Stephen Hawking*

## 9 Fabrication of qubits

In this section I'm going to present the processes and steps that are needed to fabricate superconducting qubits. Due to the size of such qubits, especially the Josephson junctions, in the  $\mu\text{m}$  to nm range, the whole fabrication should be done in a clean environment, on it's best a cleanroom. When I started my master thesis the new cleanroom at the IQOQI was more or less just opened and we were the first people which had the opportunity to work there. Being the first out of three groups from the university which participate in the cleanroom it was quite a nice time having the cleanroom for us alone. On the other hand there was no one who already knows how things work and so it was on us to find out how to do things. Over time more and more machines start running and we got used to them.

There are a few steps in fabricating superconducting qubits. Especially for sapphire, compared to silicon, there are additional steps as sapphire is non-conductive and therefore needs an additional conductive layer to do electron beam lithography. Without this layer the surface would charge up quickly and one can't do lithography as the beam gets deflected. Roughly speaking the steps which are needed to be done are

- Clean the wafer
- Spincoat resist layers
- *Sputter gold*
- Electron Beam Lithography
- *Remove gold layer*
- Develop structures
- Evaporate junction layers
- Lift off residual resist layers with unwanted aluminium layers

The steps written in *italic* are just done for non conductive substrates like sapphire. In the following I'll give a short description of the procedure steps and the parameters I used.

### 9.1 Wafer preparation

#### 9.1.1 Clean the wafer

The first step to do with every wafer, is to clean the wafer and make sure that every wafer has the same starting point. Even if they are completely new out of the box, or reused. The process for cleaning changed a bit over time. In the beginning we did it in three steps.

The first step was to put the wafer in a glass with Aceton, to get rid of all the organic stuff, and put it in the *Sonicator* for 10 min at 100% and 35 Hz. Afterwards we rinse the wafer immediately with Aceton while transferring it in a glass with Isopropanol. We then sonicate again for 10 min at 100% and 35 Hz. As a last step, we rinse the wafer with Isopropanol while putting it in distilled water. We shake it a little bit in the water and rinse it a last time with the distilled water before blow drying the wafer with nitrogen.

The crucial thing is, that the wafer always sees liquid, especially on the side on which one likes to write on. Neither Aceton, nor Isopropanol, nor the water should get a chance to evaporate on the wafer and stay behind as some kind of residue.

After some time, we got a *SenTech* machine, where we could clean the wafer with an oxygen plasma. The advantage of this is, that the wafer has no contact with liquids anymore and therefore no leftovers from the solvents can stay behind. We did a "soft- $O_2$ -plasma" cleaning for 300 seconds and just added this step after the cleaning with the solvents.

For the wafers presented in the following chapter 10, this was done for the "Test on Silicon" and

"KC003329" wafers.

For "KC003326" we skipped the steps in the Sonicator and put the wafer 10 min in Aceton before rinsing it with Aceton. Then we put the wafer 10 min in Isopropanol and rinse it with Isopropanol and then with distilled water. Afterwards we blow dry it with nitrogen. Then again the "soft- $O_2$ -plasma" cleaning was done.

After the plasma cleaning step, we immediately continue with spincoating the resist layers onto the wafer. Due to the plasma treatment, the wafer gets hydrophilic and we saw the problem, that the resist crawls underneath the wafer during spinning. Therefore we had to change the way how to spincoat the resist on the wafer.

In my case, the plasma cleaning brought no obvious improvement in the fabrication, so I decided to change back to just clean it with solvents. I even skipped the 10 min in Isopropanol and stayed with just **10 min in Aceton** and the **rinsing with Aceton, Isopropanol, distilled water and the blow drying with nitrogen**. This was done for the wafers "KC003361", "KC003364", "KC003368" and "KC003369" discussed in chapter 10.

In tab.4 the described steps for the presented wafers are summarized. The steps I finally stick to after a long trial are marked in gray.

Table 4: Summary of the described steps to clean the wafer. The steps for each of the presented wafers in chapter 10 are listed. They are processed from top to bottom. In gray the steps I stick to, after a long trial, are marked.

Step:	Silicon	KC29	KC26	KC61	KC64	KC68	KC69
Aceton sonication	✓	✓					
Aceton 10 min			✓	✓	✓	✓	✓
Aceton rinsing	✓	✓	✓	✓	✓	✓	✓
Isoprop. sonication	✓	✓					
Isoprop. 10 min			✓				
Isoprop. rinsing	✓	✓	✓	✓	✓	✓	✓
Shake in distilled water	✓	✓					
Distilled water rinsing	✓	✓	✓	✓	✓	✓	✓
Blow drying	✓	✓	✓	✓	✓	✓	✓
$O_2$ plasma cleaning	✓	✓	✓				

### 9.1.2 Spincoat resist layers

After cleaning the wafer, we immediately continue with spinning two layers of resist for the e-beam lithography, with a spincoater (Model WS-650MZ-23NPPB). A picture of the spincoater and the used hotplate is shown in fig.20. As already mentioned, we need two layers of resist to



Figure 20: Picture of the spincoater and the hotplate which are used for qubit fabrication.

do Bridge-free junctions. Two polymers with different sensitivities, to obtain an undercut in the structures written with the electron-beam, are required. For the first layer we use the Copolymer

MMA (Methyl methacrylate, exact: MMA(8.5)MAA EL 13 from MicroChem<sup>TM</sup>). As second layer we spincoat PMMA (Polymethylmethacrylate, exact: 950 PMMA A4 from MicroChem<sup>TM</sup>) which is a long chain polymer. With PMMA very high resolution can be achieved in the development, because only the very smallest fragments get developed and only the primary electrons of the electron beam reach the threshold to break a polymer chain.[24] In tab.5 the steps and parameters for the spincoating process I used are summarized. For silicon, the wafers are now ready to expose

Table 5: Recipe steps and parameters to spincoat the polymer layers on the wafer.

Step	Resist	Ramp rate [rpm/s]	Spin full speed [rpm]	Spin time [s]
1	Copolymer EL-13	1000	2000	100
2	"bake" 5 min at 200°C on hotplate			
3	A-4 PMMA	1000	2000	100
4	"bake" 10 min at 200°C on hotplate			

the structures in the e-beam. For sapphire, we have to sputter the conductive layer, in our case gold, on top of the resist.

To get an idea how the revolutions per minute (rpm) of the spincoater influence the polymer thickness, I did a test series with the Copolymer EL-13 on silicon. I spincoated five wafers, each with the same amount of material, the same spincoat duration of 1:40 min and an acceleration of 1000 rpm/s, but different full speed rpm values. After baking the resist 5 min at 200°C on the hotplate I made three scratches on each wafer and measured the height with a profilometer. This procedure I did twice. The averaged values of all measurements for the different rpm values are plotted in fig.21. In fig.22 four of the used wafers are shown. The wafer spincoated with 3 000 rpm

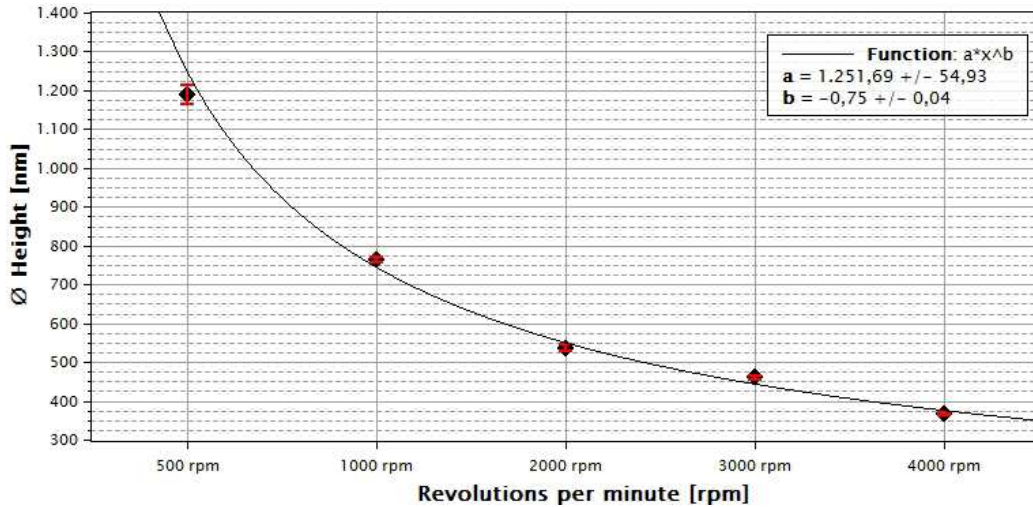


Figure 21: Spincoated copolymer EL-13 heights on silicon, depending on the revolutions per minute of the spincoater. The dependence is a power law  $y \sim x^{-0,75}$ .

isn't shown, as it broke during the second time measuring. One can see, that for the used amount of material and these settings of the spincoater, the minimum value for the revolutions per minute to fully cover the wafer with the Copolymer is somewhere between 1 000 and 2 000 rpm. Therefore it follows, that in this case, the maximum height of the Copolymer that can be achieved over the whole wafer is  $< 780$  nm.

### 9.1.3 Sputter gold

For non-conductive substrates a conductive layer is used to conduct away the electrons and avoid charging under the electron-beam. In fig.23 (a) the sputter coater, used to sputter the conductive layer, is shown. In our case we sputter gold onto the resist on top of a sapphire wafer. The

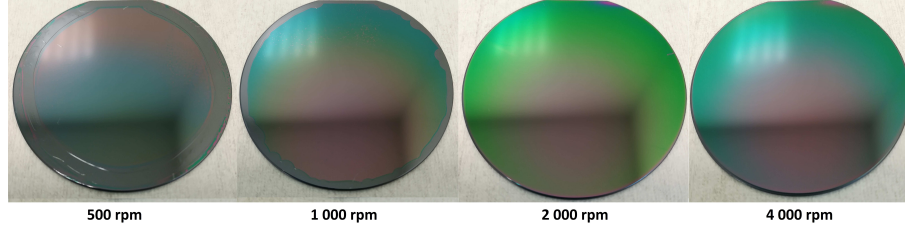
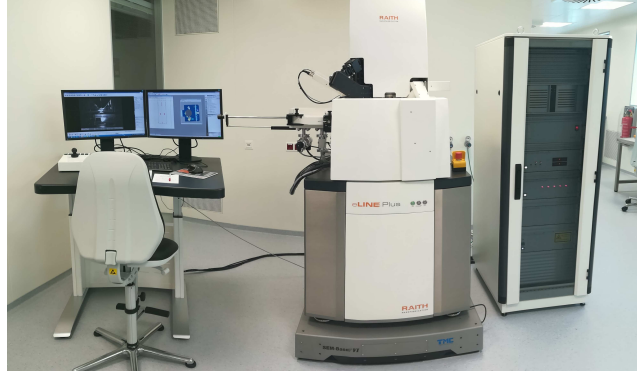


Figure 22: Silicon wafers spincoated with the copolymer EL-13. Spincoating parameters: time: 1:40 min, acceleration: 1 000 rpm/s, full speed: different for each wafer as labelled below the wafer. With too low rpm the wafer is covered only partially with resist.



(a)



(b)

Figure 23: (a) Picture of the gold sputter coater used to sputter a thin layer of gold on top of the wafer to avoid charging of the surface under the electron beam. (b) Picture of the e-beam machine used to write the qubit structures in the resist on the wafer.

challenge is to find the right settings for a gold layer which is just thick enough that the surface doesn't charge too quickly under the electron-beam. If the surface charges quickly, the writefield alignment for the e-beam lithography is very difficult to do. The parameters I used to sputter the gold layer are listed in tab.6.

Table 6: Parameters used for sputtering gold on top of the resist.

<b>Table position:</b>	at the very bottom
<b>Duration:</b>	170 s
<b>Power:</b>	10 mA
<b>Pressure:</b>	0,6 mBar

## 9.2 Electron-beam Lithography

Electron-beam lithography (EBL) is one of the big steps in fabricating superconducting qubits. Especially for us, as we all were more or less new in this business and also the machine (a eLINE Plus from *Raith*, shown in fig.23 (b)) was new in the cleanroom, it was quite challenging to get used to the machine and find out how it works, despite two weeks of tutorial and training. In the following I first give the most important theoretical background informations to understand how the EBL is working. Afterwards I describe the different steps one has to do and with which parameters we used the machine to do lithography for the qubits and what the problems were that we had.

### 9.2.1 Theoretical background

In nanofabrication EBL is one of the most important techniques which can create arbitrary patterns on the nanometer scale. The resist we are using is a positive tone resist. This means, that the structures, written with the electron beam, can be washed away with a solvent. In contrast, for a negative tone resist, the structures stay behind and the rest of the resist goes away. With the positive tone resist we therefore create the mask for the structures.

During exposure the polymer chains of the resist get broken up into smaller, more soluble fragments, as sketched in fig.24 (a), which dissolve during the developing step. The most common positive resist used is PMMA, which we also use as the second polymer layer. With its long polymer chains it takes many electrons to cut them before the fragments become significantly soluble. This is why PMMA can be developed with high resolution. Few of the scattered electrons lead to sufficient exposure to break the chains. In fig.24 (b) the distribution of PMMA fragment sizes for different *doses* (unit for how much charge is deposited per square centimeter [ $\mu\text{C}/\text{cm}^2$ ]) at 10 keV is shown. With increasing dose, the average fragment size decrease and the solubility in the developer increases. In our case we use layers of different polymers to have two different sensitivities to the electron beam and achieve a defined undercut in the resist without overexposure.

As the electrons enter the resist, a few things can happen. First of all the electrons can be directly reflected back to the source. Those electrons have no effect on the resist, but are used for imaging, as we will see later. Second, we get inelastic collisions with the resist. The inelastic collisions result in ionization and leads to *secondary electron* generation, as sketched in fig.24 (a). The secondary

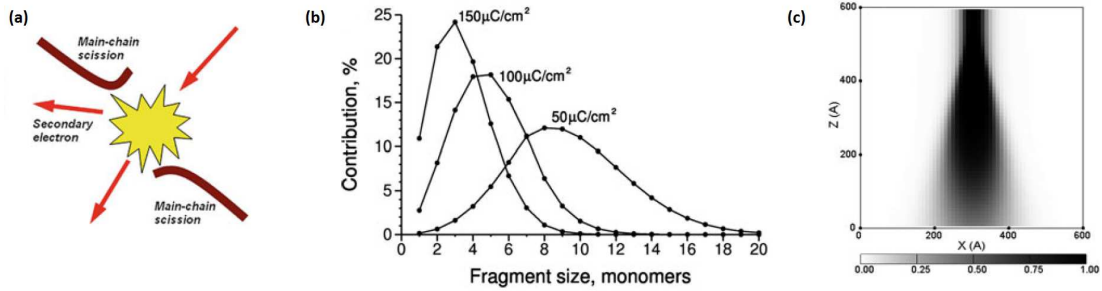


Figure 24: (a) Breaking of the polymer chain during exposure. (b) Contribution of different fragment sizes for different doses at 10 keV. (c) Cross section of the spatial distribution of fragments smaller than 10 monomers within the resist. Z(A) is the height of the polymer. All pictures taken from [24].

electrons have a short range, but may limit the resolution of the EBL in the end by breaking chains nearby. In addition also a series of low energy elastic collisions occur, which deflect the electrons a bit. This *forward scattering* broadens the beam. It therefore also influences the resolution and increases with increasing thickness of the resist.

In addition to this scattering events, most of the electrons pass completely through the resist and enter the substrate. Some electrons manage to go through enough "large angle collisions" to re-emerge back into the resist, in an area larger than the beam diameter. At high energies, these *backscattered* electrons can cause exposure at distances of a few micrometer away from their initial entry point and lead to the so-called *proximity effect*. Structures at that position then become overexposed due to this extra dose.

Fig.24 (c) shows a cross section of the spatial distribution of polymer fragments smaller than 10 monomers. Z(A) is the height of the polymer. One can detect the broadening of the electron beam due to the elastic collisions with the resist.

For understanding the relationship between exposure time, dose and development, the distribution of fragment sizes is an important factor.

In [24] the authors did test gratings on a 65 nm thick PMMA layer on silicon with a voltage of 10 keV for different doses. They observed different morphologic regimes of the PMMA structures which are shown in fig.25. For low doses the limiting factor for good results is underexposure. With increasing dose the gratings tend to build micelles (spherical amphiphilic structures with a hydrophobic core and a hydrophilic shell [25]), or collapse. At high doses overexposure is the

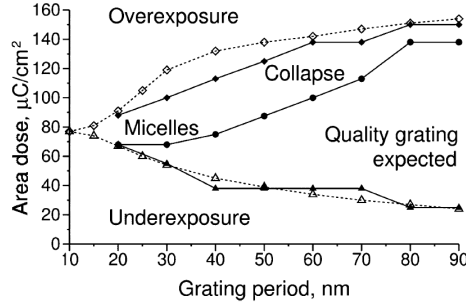


Figure 25: Different morphologies in PMMA for various grating periods and area doses at 10 keV. Filled symbols are experimental results whereas open symbols represent numerical modelling. Triangles show the boundary for underexposure, diamonds the boundary for overexposure and the circles show the boundary for collapsing or producing micellized patterns. Picture taken from [24]

limiting factor for good gratings. Although that are somehow obvious and expected results, there is an interesting take away. One can see that there is some kind of dose window between the different limitations. This window represents the robustness of the process and the reproducibility of the gratings. With decreasing grating period this dose window gets smaller and smaller, up to a minimum reasonable dose window which characterizes the resolution. [24]

### 9.2.2 Writing qubits with electron-beam lithography

Here I'll explain the main steps doing lithography and what to pay close attention to. In principle the machine can be used as a microscope or for lithography. For imaging you "just" need to optimize the parameters with which you can change the resolution of the beam, like the focus, the astigmatism, the aperture alignment and the beam shift. All the other steps, like defining the coordinate systems, the writefield alignment and all the things one has to think about for the designed structures, can be skipped for imaging.

For lithography, first of all, one has to design the qubit structures. This can be done before working with the machine. There are different programs to do this. I decided to do it with the Raith software which is also used on the e-beam computer to do lithography. Some of the features like the matrix copy, where one can easily do dose variations, are exclusive in this software. Fig.26 (a) shows an example of how such a design of a qubit can look like. By double clicking on an *element* of the design the "Edit"-window (fig.26 (b)) shows up where one can set the corresponding attributes. Each element of the structure is assigned to a so called *layer*. The layers can be chosen to be written with different apertures, one aperture after the other. For each element one can also set a different *dose factor* with which the overall dose is multiplied. Notice that it shouldn't be zero, otherwise no dose would be deposited.

After designing the structures and preparing the wafer, as described in the sections before, one can mount the wafer on the so called *stage*, as shown in fig.27 (a), which can then be loaded into the machine. Remember where you put the waferflat, to have an axis where you easily can define a new coordinate system on the wafer (U,V,W), in addition to the coordinate system of the stage (X,Y,Z). This new coordinate system is needed on every sample. The electron beam is moving in these coordinates. By defining this so called *global U-V-system*, the sample is therefore adjusted to the stage. The beam also has to be adjusted to this new coordinate system, which can be done in the so called *writefield alignment* procedure. We will come to a more detailed explanation a bit later.

There is also the *local u-v-system*, an additional coordinate system one can define on the wafer. It can be used to refind your position on, for example, a large periodic structure within the design. In fig.27 (a) an example of a local u-v-system and also the global U-V-system and the X-Y-Z-coordinate system of the stage are drawn.

Fig.27 (b) shows an overview of the different possible coordinate systems one can use. The Transformation A between the stage and the sample is given by defining the origin and the U-axis of the global U-V-system. The same for Transformation B, which is given by defining the origin and

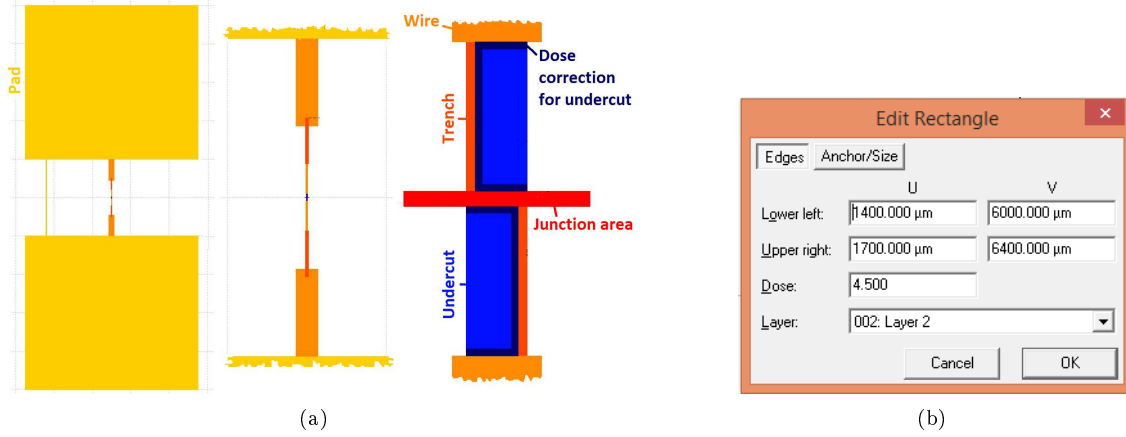


Figure 26: (a) Example of a qubit design in the Raith software. Each element shown has a different colour which indicates a different dose factor given to this element. The design of the junction shown here is that of a bridge free junction. (b) Screenshot of the "Edit"-window in the Raith software to set the properties of an element in the design.

the  $u$ -axis of the local coordinate system. Transformation C is in principle the writefield alignment procedure. The user does this alignment graphically, as explained below, and the software calculates possible correction factors for zoom, shift and rotation of the beam axis according to the defined global coordinate system.

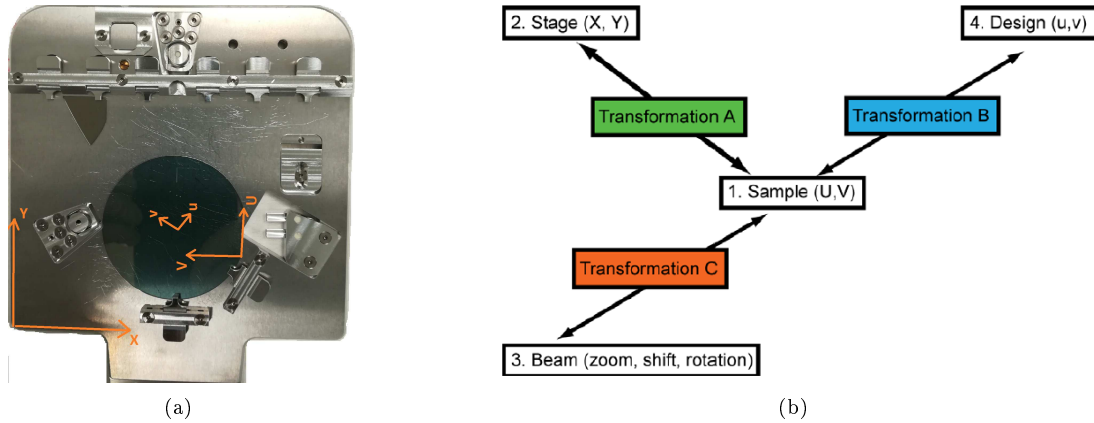


Figure 27: (a) Picture of the stage with a mounted wafer. The  $X$ - $Y$ -coordinate system of the stage, a global  $U$ - $V$ -coordinate system with the wafer flat as  $U$ -axis, and a possible local  $u$ - $v$ -coordinate system are shown. (b) An overview of the different coordinate systems. "Transformation A" and "Transformation B" are done by defining an origin and the  $U$ -/ $u$ -axis of the corresponding coordinate system. Transformation A connects the coordinates of the stage with the wafer. Transformation B connects the coordinates of the wafer with a possible structure on the wafer or within the design. The writefield alignment corresponds to the "Transformation C". It aligns the "beam-coordinates", to the coordinates of the sample. Picture taken from [26].

After defining the coordinates, the image has to be optimized. Therefore, the first thing to do, is to set the acceleration voltage (EHT) and the aperture you want to work with. The optimization is done with directly reflected electrons, meaning with the picture one gets with the InlenseDuo detector. There are different options to optimize the resolution. One can change the focus, the astigmatism, the aperture alignment and the beam shift. In the program you can save these settings in a predefined parameter set or just create a new one and save them there.

To do the optimization, you need a small particle or artefact. This can be created for example



by scratching the surface on the edge of the wafer. In fig.28 structures of a scratched gold layer on sapphire, before and after the different beam optimizations, are shown. The first picture in a)

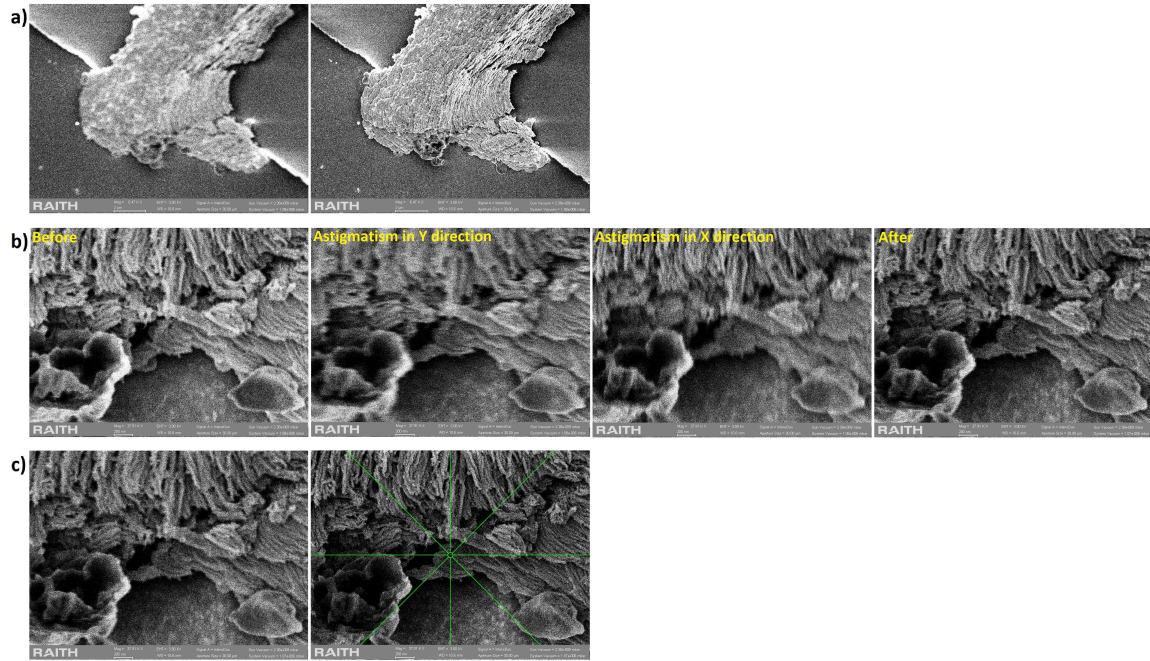


Figure 28: In a) the difference of a badly focused and a well focused picture is shown. This is an optimization one can easily do to get nice pictures - playing with the focus for even higher and higher magnifications. In b) the picture is even more zoomed in and optimized for the astigmatism. The first picture is before correction, the second and third show extremely misaligned astigmatism values. In the last picture you can see the corrected one. Starting with this last picture of b) in c), the improvement of the picture after the aperture alignment is shown. For more explanations see the main text. All pictures are taken with the settings: WD = 10.6 mm, Signal = InlenseDuo, Aperture Size = 30  $\mu\text{m}$ , EHT = 3 kV.

is the picture you see by just magnifying the structure. The second one is the same picture after changing the focus of the beam. This already clearly improves the resolution of the picture.

In b) I zoomed in on the bottom part of the structure. On the first picture, the focus is already optimized. Now I want to optimize the astigmatism of the picture. The best thing to do this is to find a particle which you know has a round shape. On round particles you can see best how the change in the astigmatism changes the resolution of the picture. Here I didn't used a round particle, but instead used the huge amount of different structures on the picture. On the second picture, the misalignment of the astigmatism in y-direction is shown. The resolution gets worse and the picture seems to stretch in x-direction. On the third picture the same misalignment is done in x-direction and shows the stretching of the picture in y-direction. After some time of optimization, one ends up with settings which provide the best resolution. By optimizing again the focus, one gets the last picture in fig.28 b). Comparing it to the first picture we can see, that the overall resolution is a bit better. Also the egg-shaped structure in the bottom right corner for example is now a bit more stretched in y-direction as a result of the astigmatism correction.

In fig.28 c) the last picture in b) gets even higher resolution by optimizing the aperture alignment. For this, again, a defined particle, marked with the green crosshair shown on the second picture, is used. The alignment is done with the so called *wobble mode*, where the focus is changed constantly through the surface. This leads to a wobble of the picture, if the aperture is not perfectly aligned. To align the aperture, one has to find the settings where the picture in the wobble mode doesn't move any more. The result of the aperture alignment is shown on the second picture. One can see, that the resolution is even better than before. The last optimization, is the beam shift. In our case, the best results are achieved by setting the beam shift to zero.

After this image optimization, one can start to align the beam to the global coordinates with the

writefield alignment. To explain this procedure, it is useful to first introduce a few terms and definitions used in the e-line software to place design elements and do lithography.

First, there is the so called *working area*, which is set automatically around all the structures in the design. As the name indicates it defines the area in which the beam is "working". One can also define it by hand which is sometimes needed to avoid *stitching* in the design. Stitching appears on the edges of a *writefield*, when the beam moves from one writefield to another (more about this later). So what is a writefield? The working area is divided into writefields, predefined from  $1 \mu\text{m}^2$  to  $2 \text{mm}^2$  and connected to a corresponding magnification. Within a writefield the stage with the sample doesn't have to move. The area of the writefield can be reached by just deflecting the electron beam. The more the beam is deflected the smaller the resolution, as the beam broadens due to the growing angle under which it "hits" the polymer. Therefore, if small structures with high resolution need to be written, it is better to choose a small writefield. It can be helpful to

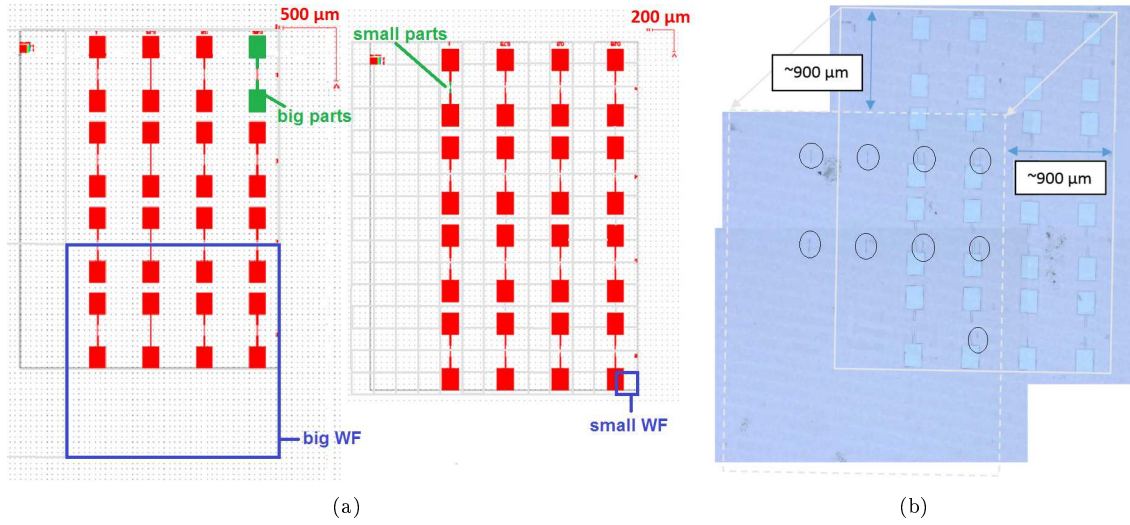


Figure 29: (a) Screenshots of the design. It is turned upside down to better compare it to the microscope picture. (b) Optical microscope pictures of the structures that were written. The black circles indicate the small structures. The small and big parts of the qubit design in (a) (coloured in green) are written with different writefield sizes. One of each writefield size is shown by the blue square. They respectively have a side length of  $2000 \mu\text{m}$  and a side length of  $200 \mu\text{m}$ . As shown in (b), the big and small structures are shifted by half of the big writefield minus half of the small writefield, which is  $900 \mu\text{m}$  in this case. This shift is due to the automatic placement of the center points of the writefields at the origin of the global coordinate system and has to be compensated manually before writing.

define different writefield sizes, when very big and very small structures are within the same design. The advantages of big writefields are, that they can avoid stitching problems and can help you save time. By using bigger writefields for the bigger structures, the number of movements of the stage from writefield to writefield, can be reduced. This moving time is the slowest time scale in the lithography process. In fig.29 one of our first tries to write whole qubit structures with two different writefield sizes is shown. For the big structures  $2000 \mu\text{m}$  writefields, and for the small structures  $200 \mu\text{m}$  writefields are used. One can see, that they are shifted by about  $900 \mu\text{m}$  in U- and  $900 \mu\text{m}$  in V-direction against each other.

This problem can be understood by looking at fig.30 where the placement of writefields is sketched. The software places the center points of the writefields automatically to the global (0;0)-point. This leads to a shift between the design elements written in the small writefields and those written in the big writefields (see (a)). This shift has to be corrected manually in the *position list* (a list including all the tasks and properties for a whole lithography process). As shown in fig.30 (b), the shift, to correctly overlap the structures again, is half of the big writefield size minus half of the small writefield size. In the example before, this shift fits to the observations ( $\frac{2000}{2} - \frac{200}{2} = 900 \mu\text{m}$ ).

Now, as we know what writefields are and how they are used in the software, we can run the

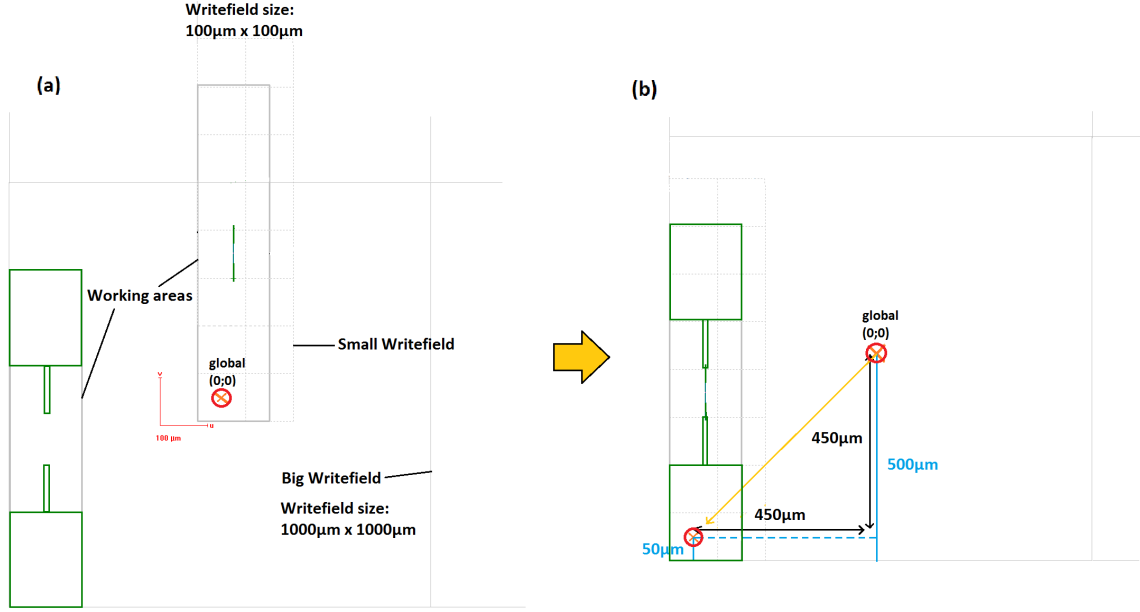


Figure 30: A qubit design written with a  $100 \mu\text{m}^2$  writefield for the small structures and a  $1000 \mu\text{m}^2$  writefield for the big structures is shown. With the orange crosses the center of the writefields are marked. The red circles indicates the starting points of the beam. In (a) the starting points for the beam, which are the center points of the writefields, are placed at the same coordinate, in this case the (0;0) point. This leads to a shift between the big and small structures which has to be compensated manually. In (b) it is shown that the small writefield is shifted by  $(-450\mu\text{m}; -450\mu\text{m})$  in U and V to overlay the structures.

writefield alignment procedure to align the beam to the writefields. In our case, as we have a laser interferometer stage, we can use the laser stage as measuring standard and can get a very precise alignment. The writefield alignment has to be done for each of the used apertures!

In the figures 31 and 32 the steps of the writefield alignment procedure are shown. In fig.31 a) the theoretical movement of the stage during the procedure is sketched. The "mark" indicates the position of the electron beam, the small rectangle ("scan around mark") indicates the area in which the beam scans a picture of the particle (placed in the center of the writefield) from each corner of the writefield, by deflecting the beam. The particle should have a prominent feature, as indicated with the green cross hair in fig.31 b). This point should be clearly visible, not only in the zoom, but also from further away. It is the point to which the pictures of the "scan around marks" are corrected. In the example in fig.32 the procedure for a  $1000 \mu\text{m}$  WF and the "scan around mark" with a side length of  $100 \mu\text{m}$  was accomplished. On the left, pictures of the chosen particle from each of the four scanning positions (see fig.31 a)) are shown. The green cross indicates the center of the picture and should match with the structures marked on the particle in fig.31 b). This is not the case on all of the four pictures. Therefore the positions need to be corrected. This is done by moving the center of the picture to the point where it should be. To identify the shift, the green cross marks change to blue ones, as shown on the four pictures on the right. From this manual corrections, the software calculates correction factors for a zoom, a rotation and a shift in U and V direction. In this example one can see that also the blue crosses are not exactly at the position marked in fig.31 b). It is just a first correction in the right direction. To improve the alignment, the same procedure can be done with even smaller and smaller "scan around marks".

If the beam is not properly aligned during the writefield alignment procedure, it can lead to stitching errors of the design. In fig.33 it is sketched how the design elements could be shifted due to misalignments of beam coordinates, represented with the writefields, to the global U-V-coordinates. Fig.33 i) shows the case, where the writefields are perfectly aligned. The beam writes in perfectly aligned writefields and therefore no stitching errors appear. In ii) just the V-axis of the beam is

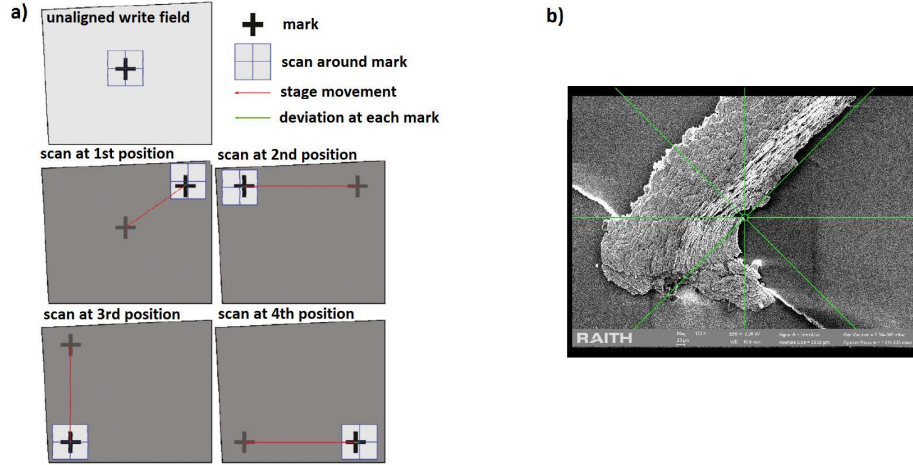


Figure 31: a) Steps of the writefield alignment procedure. A particle to do the alignment is placed in the center of the writefield. Then, the beam moves to each corner of the writefield and scans from there a small area around the particle. If the structures in the center of this scans doesn't match with the structures of the particle in the center of the picture chosen before, the picture has to be corrected. From this graphical alignment the software calculates correction factors for the zoom, the shift and the rotation of the coordinate system of the beam. Picture taken from [26] and modified. b) An artefact on a particle, chosen with the green cross mark, to do the writefield alignment.

not the same as for the global U-V-coordinate system. The parts of the design which fall across two writefields get shifted against each other. In iii) both axes are misaligned, which additionally can lead to overlaps of the structures.

To avoid stitching errors, and make sure that there is in the end no gap in the structures, one can design a little overlap between the design elements. In fig.34 there are examples of situations given, where an overlap in the design could be useful. The positions of possible stitching are marked with the green circles. In a) the structures are too long to fit in any of the predefined writefield sizes. b) shows the case, where small and big design elements aren't written in the same writefields and/or with the same apertures. This can lead to stitching errors, either due to misalignment of the writefields, or the apertures, or both. In c) multiple structures are periodically placed over the wafer. The periodicity doesn't match to the periodicity of the writefields. This leads to stitching of some of the structures and could be solved with either a smart placement of the design structures, or by defining a second, a bit larger working area in  $-U$ -direction. This would shift the structures such, that all of them lie within one writefield. This additional shift of the structures, due to the bigger working area, has to be corrected in the U-V-coordinates in the position list! In general, to increase the probability to get a working qubit, it should be a rule to avoid stitching in the design.

If now everything is aligned properly, one can set the last patterning properties: the *beam current*, the *Area Dwell Time*, the *Area Step Size* and the *Area Dose*. In tab.7 a summary of the values I used for the lithography is listed.

To summarize, the main steps for the lithography are:

- 0.) (Design the structures)
- 1.) Define the global U-V-coordinate system on the sample
- 2.) Optimize the picture
- 3.) Adjust the beam to the global coordinates with the writefield alignment procedure
- 4.) Set the patterning properties

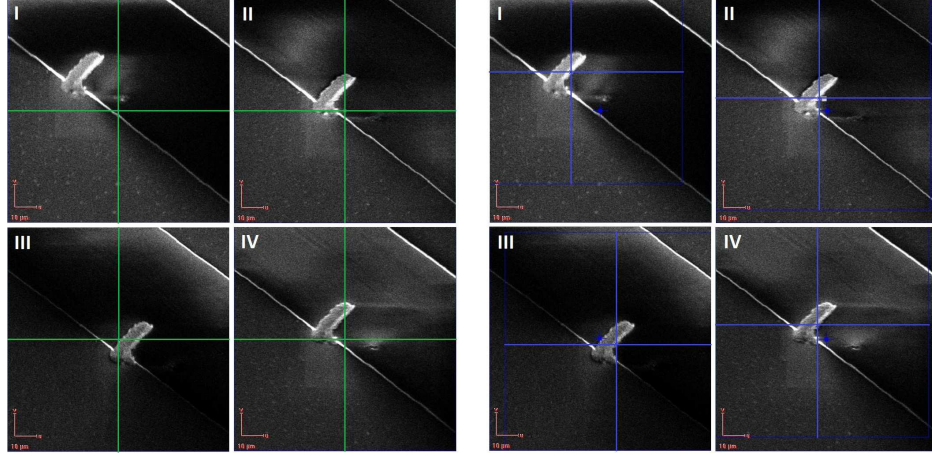


Figure 32: Writefield alignment for a 1000  $\mu\text{m}$  big writefield and a "scan around mark" of 100  $\mu\text{m}$ . On the left, the chosen particle is scanned from the four corners of the writefield. The green crosses should be at the same position on each picture. This is not the case. It therefore has to be corrected as shown on the four pictures on the right with the blue crosses.

Table 7: Summary of the parameters used for electron-beam lithography. The beam current is remeasured every time before patterning. From this value the Dwell Time is calculated.

Parameters for electron-beam lithography:			
Lithography settings	Mode:	Meander mode	
	EHT:	30 kV	
	Working distance:	10 mm	
		big structures	small structures
Patterning properties	Aperture:	120 $\mu\text{m}$	10 $\mu\text{m}$
	Writefield size:	1000 x 1000 $\mu\text{m}$	100 x 100 $\mu\text{m}$
	Magnification:	130 x	1300 x
	Beam current:	5,35 $\pm$ 0,03 nA	34,9 $\pm$ 0,2 pA
	Area Step Size:	0,02 $\mu\text{m}$	0,002 $\mu\text{m}$
	Area Line Spacing:	0,02 $\mu\text{m}$	0,002 $\mu\text{m}$
	Area Dose:	80 $\mu\text{C}/\text{cm}^2$	80 $\mu\text{C}/\text{cm}^2$
	Area Dwell Time:	59 $\pm$ 1 ns	91 $\pm$ 1 ns

The possible shifts one has to take into account in the position list are summarized in tab.8. The numbers are from an example with a 1000  $\mu\text{m}$  and a 100  $\mu\text{m}$  big writefield, and a working area that is in  $-U$ -direction about 50  $\mu\text{m}$  larger than the automatically placed working area.

Table 8: Summary of the possible shifts one has to take into account in the U-V-coordinates in the positionlist. The values are from the example above.

	small WF	big WF
Starting coordinates [mm]	(0;0)	(0;0)
Shift from...		
Writefield position [mm]	(+0 ; +0)	(+0,45 ; +0,45)
Working area [mm]	(+0 ; +0)	(-0,05 ; +0)
Positionlist coordinates [mm]	(U+0 ; V+0)	(U+0,4 ; V+0,45)

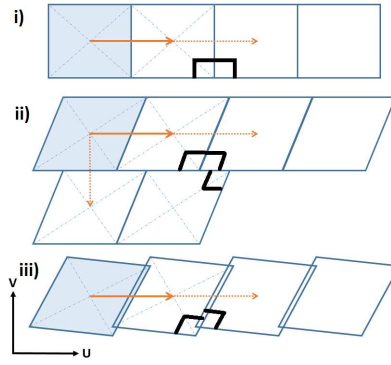


Figure 33: A few writefields in the U-V-coordinate system, "stitched" together. The orange arrows indicate the stage movement. In i) the writefields are properly aligned to the U-V-coordinate system. When the beam moves from one writefield to the other they fit perfectly together without a gap or an overlay. In ii) the writefield is aligned properly to the U-axis, but tilted against the V-axis. This leads to a shift of the structures in the U-direction. In iii) both axis are not aligned to the U-V-coordinate system. It leads to gaps and overlays of the writefields and therefore shifts the structures in U- and V-direction. Not properly aligned writefields therefore lead to stitching errors in the designed structures, when they fall across two writefields.

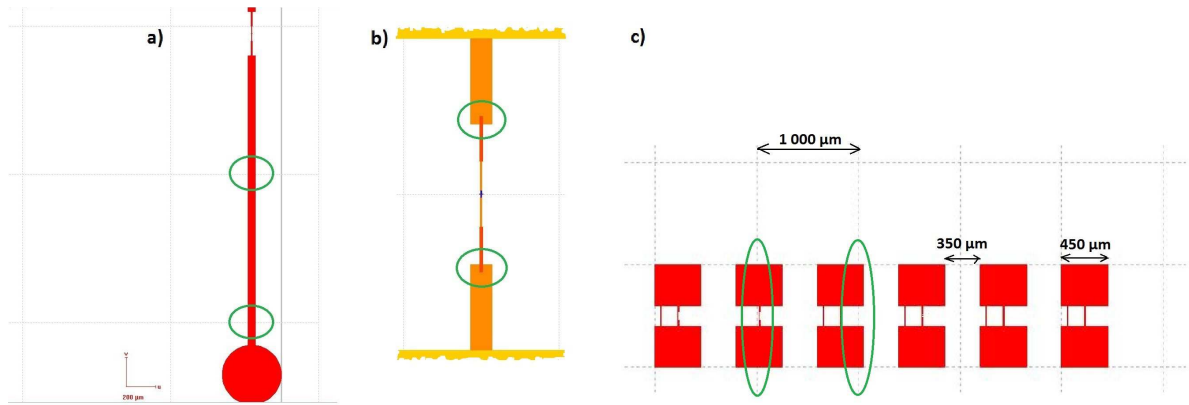


Figure 34: Cases where it could be useful to design an overlap in the structures to avoid stitching errors. Green circles indicate the positions in the design where stitching errors could appear. In a) the structure is bigger than the biggest writefield. In this case the structures has to be stitched. In b) an overlap is designed between elements which are written with different apertures. If the writefields, written using different apertures, are not properly aligned to each other, this could lead to shifts between the elements and therefore to stitching errors. c) The structures are designed and aligned such, that the sum of the structure width and the distance between the structures does not always add up to the writefield width (in this case  $1000 \mu\text{m}$ ). At some point the structures fall across the writefield and need to be stitched at these locations.

## 9.3 Development

### 9.3.1 Remove gold layer

After the lithography, the structures has to be developed. For sapphire wafers, the gold layer has to be removed before. This is done in a Lugol solution we mix ourself. The recipe is shown in Tab.9. In fig.35 a picture of the orbital shaker with the lugol solution is shown. After one minute on the orbital shaker, when all of the gold is gone from the wafer, we rinse it with distilled water. Be careful that nothing evaporates on the wafer and be quick enough that the transition between the liquids is somehow smooth.



Table 9: Recipe to mix the Lugol and remove the gold layer.

Chemical:	$I_2$ (Iodine)	$KI$ (Potassium iodide)	$H_2O$
Ratio:	1 :	4 :	40
Amount we use:	2 g	8 g	80 ml
Mix the solution for minimum 3 hours on the orbital shaker at 80rpm.			
To remove the gold layer put the wafer in the Lugol solution and put it again on the orbital shaker at 80 rpm for 1 min.			

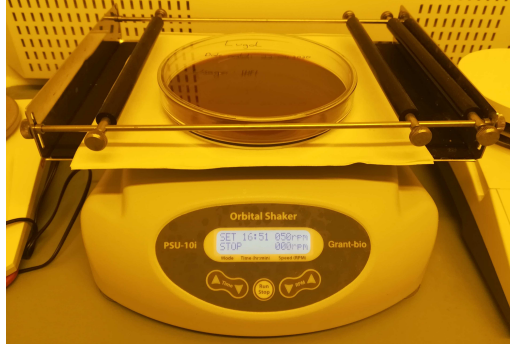


Figure 35: Picture of the orbital shaker with the lugol solution to remove the gold layer.

### 9.3.2 Develop structures

Theoretically the polymer chains of the resist, which are broken up with the electron beam, get washed out. The fragments of the polymer get surrounded by the solvent and form a gel as the molecules start to interact. The thickness of the gel depends on the fragment size and on the strength of the solvent. Once the fragments are completely surrounded by the solvent, they start to diffuse into the solvent.

This process can be described by the diffusivity

$$D \sim n^\alpha \exp(-U/kT),$$

with the activation energy  $U$ , the Boltzmann constant  $k$  the temperature  $T$  and a factor  $n^\alpha$  which describes the mobility of fragments with size  $n$ .  $\alpha$  represents the properties of the medium in which the fragments dissolve and varies from 1 in dilute solutions of small molecules to 2 for longer polymer chains in denser solutions.

As already mentioned in section 9.2.1 the averaged size of fragments depends as well on the exposure dose as on the location where it gets exposed. The diffusivity can therefore be written as

$$D = cd^\alpha \exp(-U/kT),$$

where  $c$  is a location-dependent model coefficient of proportionality and  $d$  is the exposure dose. According to Ficks law for diffusion, the removal of the resist is associated with the diffusion length of the PMMA fragments  $(Dt)^{1/2}$ . As a result, one can expect the proportionality  $\Delta x \approx dt^{1/2}$ , with the developing time  $t$ , for the development trench  $\Delta x$ . The optimal dose and time are therefore inverse proportional and should be chosen correspondingly for optimal performance. [24]

What we do in the clean room, is to develop the structures in a mixture of water and Isopropanol in a ratio of 1:3, cooled in a so called *Chiller* to 6°C (see fig.36 a)). Held with a pincette on the waferflat we move the wafer for 1 min and 45 s in the solution and stop the development immediatly by putting the wafer in water. It is important to take care that the wafer is covered with liquid the whole time as well as possible to avoid evaporation on the wafer. Developing in general is a crucial step in the fabrication process. Small changes in the temperature or time of the development can cause big differences in how the structures come out. Especially the sharpness and size of the undercut are affected by the changes. In fig.36 b) structures after the development step are shown.

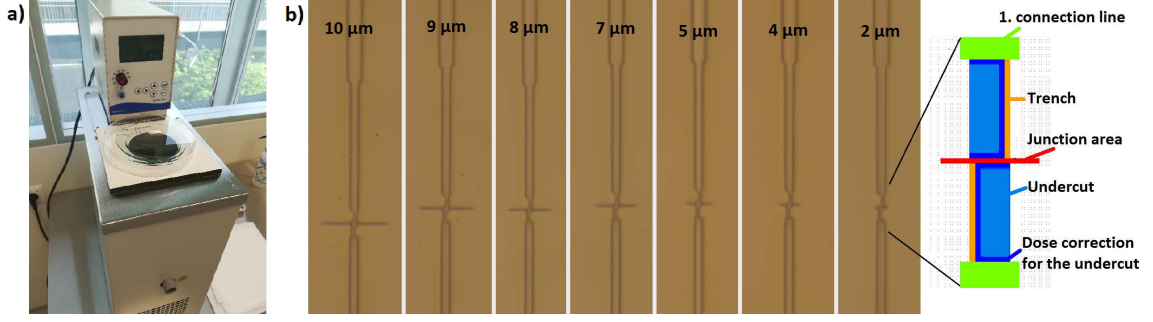


Figure 36: a) Picture of the Chiller to hold the wafer in a tempered mixture of water and Iso-propanol. b) Junction masks after developing on silicon. Picture taken with an optical microscope with a magnification of 100x. The doses and the junction width of 100 nm is the same for all junctions. The length of the junction is labelled on top of the picture. The design for the junction areas and the undercuts is shown on the very right. In the microscope pictures you can see that the red junction area, the green connecting lines to the qubit pads and the orange lines, are "washed away" in the developing step. The blue areas are the undercut areas. They are not visible in the pictures due to the top view on the junction mask.

## 9.4 Metal deposition

### 9.4.1 Evaporate junction layers

After the development, the mask for the junctions to evaporate the aluminium (Al) layers is ready. The evaporation system we are using is from the company *Plassys* and therefore in the following also called Plassys as common noun for the system. In fig.37 (a) a picture of the machine is shown. In this fabrication step one sets the properties of the junction. One defines the thickness of the aluminium layers, the time  $t_{ox}$  and pressure  $p_{ox}$  to create the oxide tunnel barrier between the two junction layers and if it is a static or a dynamic oxidation. All these settings can change the behaviour of the Josephson junction as discussed in section 7. In fig.37 (b) a sketch of the machine with its main parts, the two chambers, the rotating table, the ion gun, the electron gun to evaporate the crucibles, the different gas inlets and the different pumps, is shown. The same sketch is also visible on the screen of the machine to show what's going on. Before starting the evaporation

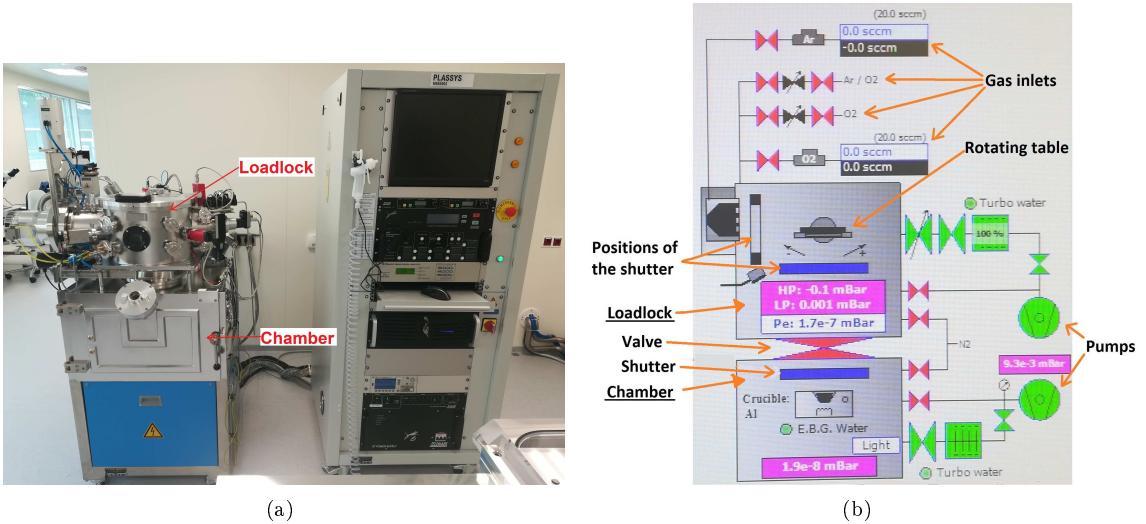


Figure 37: (a) Picture of the Plassys to evaporate the Al layers to create the qubit. (b) Sketch of the main components of the Plassys. The same sketch is also visible on the screen of the machine to see in real time what's going on.



the wafer has to be put into the machine. Watch out which way the junctions are orientated so that the Al layers get evaporated from the right direction. Have in mind, that the table turns the wafer upside down before moving to the right evaporation angle. Therefore the structures are facing to the bottom of the loadlock during the process. The aluminium is evaporated by an electron gun in the chamber and can reach the wafer, if the shutter and the valve are open.

But let's start at the beginning and have a quick overview of the main steps of the process. First of all there are two pumping steps, one for the *Load lock* and one for the *Chamber*, to make sure the process starts at the same pressure every time. For the Load lock we pump for 3 h to get a pressure of about  $1,7 \times 10^{-7} - 2 \times 10^{-7}$  mbar. The next step is a "Descum" step, a low-temperature  $O_2$ -based plasma process, to remove possible leftovers of resist in the mask. The parameters for the Descum step are shown in tab.10. Also the parameters for all the other steps can be found there.

The Descum step is followed by a "Getter" step which collects remaining gas molecules with titanium (Ti) to improve the vacuum. In our case the Ti evaporation with a rate of 0,2 nm/s takes 2 min.

Now the first layer of Al can be evaporated onto the wafer. The evaporation rate in the process is set to 1 nm/s. The thickness of the layer and the angle under which the evaporation takes place can be set individually from sample to sample. In fig.38 a) the different thicknesses of both of the aluminium layers for the different wafers are plotted. The first evaporation comes from the left

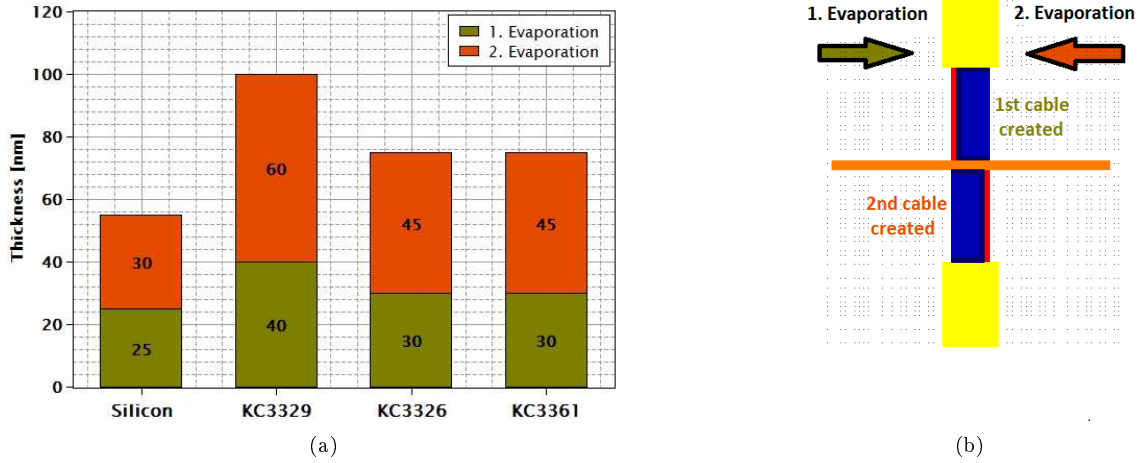


Figure 38: In (a) the thickness of the two evaporated aluminium layers for the different wafers are plotted. In (b) the junction design, and the order and directions of the two evaporations of the aluminium layers are sketched.

and creates the first junction layer and the upper connecting cable to the pads. The angle under which this layer is evaporated is  $30^\circ$  for all of the wafers. After the first evaporation, static  $O_2$  oxidation for 21 min under 35 mbar leads to the tunnel barrier for the electrons.

Then the second layer of aluminium is evaporated under an angle of  $-30^\circ$  for all of the wafers. It creates the top layer of the junction and the connecting line to the lower pads and comes from the right. In fig.38 b) the design of the junction with the evaporation directions is shown.

There is the idea, that the aging of the qubits can be stopped or slowed down by a capping layer of oxide. From the wafer KC003361 on, we therefore included an extra oxidation step for 3 min under 20 mbar at the end of the evaporation process, to create a controlled oxidation layer. At the end of the process, the wafer can be unloaded and one can continue with the lift off step.

A first estimation of how the oxidation pressure and time, to create the tunnel barrier, changes the behaviour of the junction, can be made from resistance measurements at room temperature of the junctions  $R_n$  by fitting the relation

$$R_n \sim (t_{ox} P_{ox})^x. \quad (23)$$

Table 10: Summary of the parameters used for the aluminium evaporation procedure in the Plassys.

Descum step:		Getter step:		Evaporations:		Oxidation:	
Voltage:	200 V	Material:	Ti	Material:	Al	Press.:	35 mbar
Current:	10 mA	Evap. rate:	0,2 nm/s	Thickness:	see sect.10	Time:	21 min
Ar flow:	10 sccm	Duration:	2 min	Angle:	$\pm 30^\circ$	<b>Capping layer:</b>	
O <sub>2</sub> flow:	5 sccm			Evap. rate:	1 nm/s	Press.:	20 mbar
Time:	1 min					Time:	3 min

The question is, what the value of  $x$  is in this relation. By measuring the normal state resistance of some samples with different oxidation times and pressures one can extract  $x$  with a fit through the data.

In [27] the authors found that the resistance depends more on the oxidation time than on the oxidation pressure. For  $t_{ox}$  and  $P_{ox}$  they got the values  $x = 0,65$  and  $y = 0,43$  ( $t_{ox}^x \cdot P_{ox}^y$ ).

#### 9.4.2 Lift off residual resist layers with unwanted Al layers

The lift off step is the last step in fabricating superconducting qubits. In this step the polymer mask with the aluminium on top, is taken off, so that just the qubit structures stay behind. This lift off procedure changed a bit over time, to improve the result. In the beginning we just put the wafer in Aceton over night. The next try to improve the lift off, was to put it on the orbital shaker at 50 rpm for some time, to hopefully remove the mask a bit quicker. Another try was to heat the Aceton up to 60°C, to improve the time of the lift off even more. All those "tricks" turned out to not improve the result. The final procedure for the lift off step I used, was to put the glass with the Aceton and the wafer a few minutes in the Sonicator, leave the wafer again in Aceton over night, and do the sonication a second time before rinsing the wafer with Aceton, Isopropanol and distilled water. The exact recipe is given in tab.11. In fig.39 pictures of the lift off are shown.

Table 11: Procedure steps for the lift off.

Step	Description	Time	Frequency	Power
1	Leave wafer in Aceton	5 min		
2	Sonication	1 min	35 kHz	20%
3	Leave wafer in Aceton	over night		
4	Sonication	1 min	35 kHz	20%
5	Rinse with Aceton, Isopropanol and distilled water.			

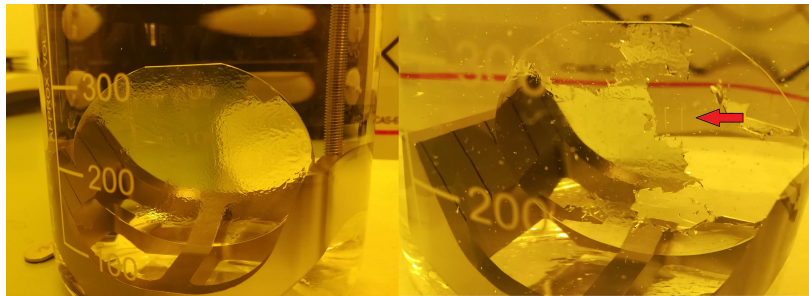


Figure 39: Pictures of the wafer placed face down in Aceton to do the lift off of the polymer mask and the unwanted Al layer. In the picture on the right, marked with the red arrow, the qubit structures are already visible.

## 9.5 Measuring the normal state resistance of the junctions

As discussed in section 7, by measuring the resistance of the qubits at room temperature, one can get a first estimate, if the qubits are working and if they are in the right frequency regime they are designed for.

There are three possible outcomes for the resistance measurements. First, there is the possibility to measure nothing. This means that your junction is open and not connected at all. Something in your fabrication process must be wrong. Second, if you measure a very small resistance close to zero you have to assume that there is a direct connection between the qubit pads. This also points to a problem in fabrication where a small short has been created somewhere. Finally you can measure a value for the resistance in the few  $k\Omega$  range. The exact value depends on your design. Your fabrication process seems to work and the qubit should be measurable in the waveguide.

In fig.40 a sketch and a picture of the set up for the junction-resistance-measurements are shown. By putting small needles on each of the pads of a qubit, the resistance can be measured with a multimeter. In addition a  $10\text{ k}\Omega$  resistance is connected in series with the qubit and the multimeter to prevent high voltages which could lead to a short in the qubit. Through a microscope one can see the qubits and can guide the needles on the pads. In fig.41 the average of all the measured

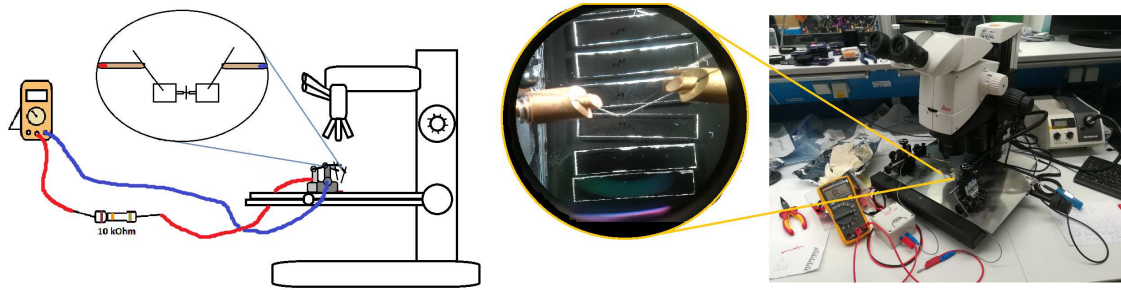


Figure 40: A sketch and a picture of the set up for measuring the normal state resistances of the qubits.

resistances for the  $2\text{ }\mu\text{m}$  and the  $2,5\text{ }\mu\text{m}$  long testjunctions of the wafer KC003368 are plotted for different dates over a period of nearly five months, at which the junctions were remeasured to see if and how the resistances change over time. The error bars are the standard deviations of the averages. For this wafer a capping oxidation step at the end of the evaporation procedure to prevent the aging of the qubits was added. The resistances measured on 07.06.19 are the testjunctions excluding the junctions which were put in the fridge. On 13.06.19 the remaining junctions from the cooldown were measured. Below the chart a few additional dates are marked which may be interesting for the evolution of the resistances. After dicing they were put back into the desiccator until they were used to cool down. One can see, that the resistances grows over time, but seems to saturate at some point. In this period of nearly five months the junction resistances for the  $2\text{ }\mu\text{m}$  long junctions changed from  $4,8\pm0,4\text{ k}\Omega$  to  $6,7\pm0,6\text{ k}\Omega$  and for the  $2,5\text{ }\mu\text{m}$  long junctions from  $3,3\pm0,2\text{ k}\Omega$  to  $4,6\pm0,2\text{ k}\Omega$ . So both designs aged by about 40%. The huge decrease of working junctions after dicing is due to the fact, that they were dicing marks and were just diced away.

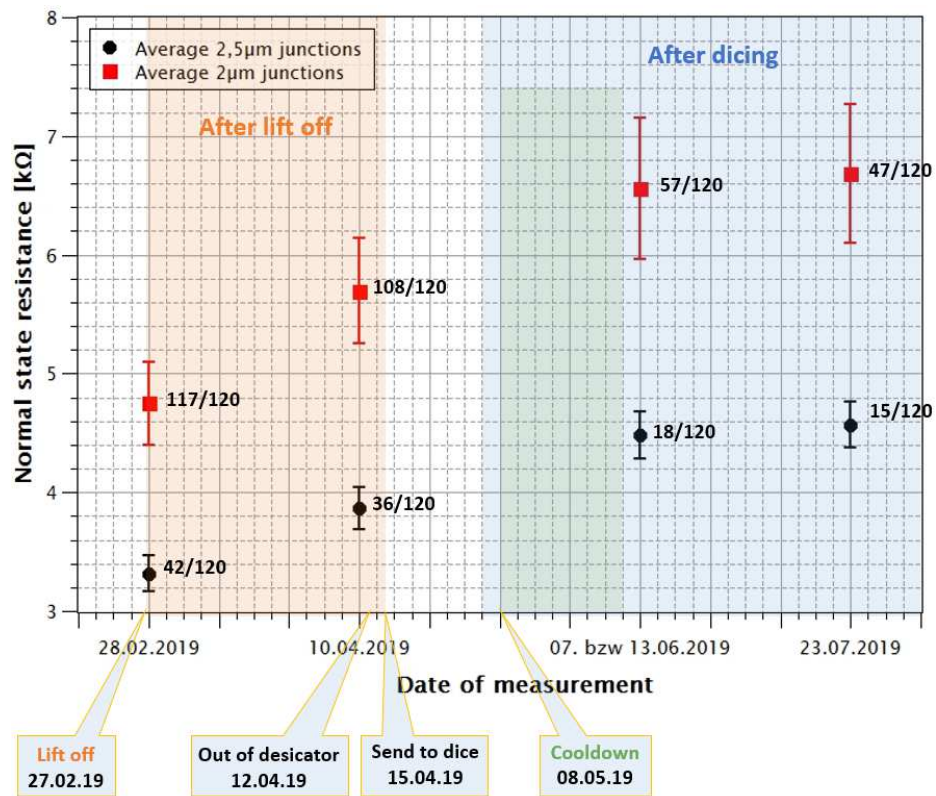


Figure 41: Normal state resistances of the wafer KC003368, measured over time. The numbers next to the data points are the number of working junctions out of a total of 120 junctions, for each junction size. The error bars are the standard deviations of the average. In the bubbles below the chart a few additional dates are marked, which may be interesting for the increase of the resistance and the decrease of junctions that are alive over time.

"Continuous improvement is better  
than delayed perfection."  
*Mark Twain*

## 10 Fabrication progress

In this section the fabrication progress is presented with examples on a selection of wafers. Before we start let's mention a few general things that are the same for each wafer.

The e-beam pictures in the following are either taken with the "InlenseDuo" detector, where the electrons are reflected back directly from the junctions to where they came from, or with the "SE2" detector, where the image is created with the secondary electrons generated through scattering on the structure.

The recipe for the aluminium evaporation is in general the same for each presented wafer. One can find the exact parameters in section 9.4.1. Just the thicknesses of the aluminium layers have been varied. They play an important role in the design of the junction. The thickness of the first evaporated aluminium layer changes the widths of the trenches and therefore changes the width of the second cable. In some of the following e-beam pictures this is clearly visible, as one cable is thinner than the other one, or in the worst case, no longer connected at all.

### 10.1 Test for different junction sizes on Silicon

The aim of this wafer is to see if the qubit fabrication in general is going to work. To make it as simple as possible we use silicon to avoid the additional gold layer needed on sapphire substrates. As shown in fig.42, in this design there are nine times the same two qubit lines, with junction lengths from  $1\ \mu\text{m}$  -  $10\ \mu\text{m}$ . The dose factors for the different elements are listed in tab.12.

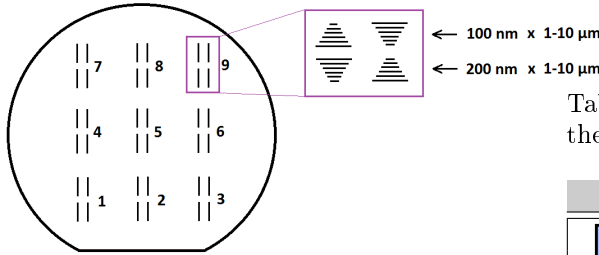


Figure 42: A sketch of the design on the wafer. There are nine times the same four "junction lines" with junction lengths from  $1\ \mu\text{m}$  -  $10\ \mu\text{m}$ . The top two lines are always junctions with a junction width of 100 nm and the bottom two lines are junctions with a width of 200 nm. In one case they go from  $1\ \mu\text{m}$  -  $10\ \mu\text{m}$  from bottom to top and in the other case from  $10\ \mu\text{m}$  -  $1\ \mu\text{m}$ .

Table 12: Dose factors for the junctions on the silicon wafer.

Doses:		
	<i>Pads</i>	4,5
	<i>3.-connection-line</i>	4,5
	<i>2.-connection-line</i>	5
	<i>1.-connection-line</i>	5
	<i>Junction area</i>	7,5
	<i>Trench</i>	6,5
	<i>Undercut correction</i>	1
	<i>Undercut</i>	1,4

Half of them have a junction width of 100 nm and the other half a width of 200 nm, spread over the wafer. In total, we then have  $9 \times 2 \times 2 \times 10 = 360$  junctions which means  $10 \times 2 = 20$  different junctions, each  $9 \times 2 = 18$  times. With this amount of junctions we can already do some statistics. In fig.43 the resistance of every single junction, which wasn't open, is plotted. The positions on the x-axis correspond to the numbered positions in fig.42. In (a) the junctions with a width of 100 nm and in (b) the junctions with a width of 200 nm are shown. The  $1\ \mu\text{m}$  junctions are all open or short, so they are excluded. Also the  $2\ \mu\text{m}$  junctions are excluded because their resistance is so high, that it is difficult to compare to the others. At each position there are two identical junctions. One is marked with a dot and the other one with a cross. The different colours label the different junction sizes. Each colour should therefore have the same normal state

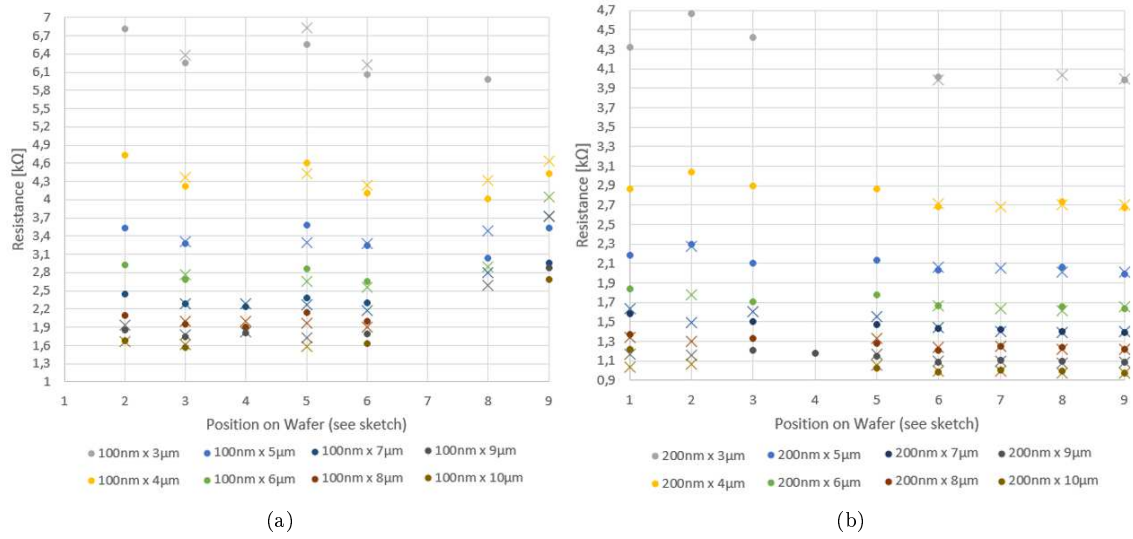


Figure 43: Normal state resistances  $R_n$  of the junctions on the silicon wafer, with a design length of  $3 \mu\text{m}$  -  $10 \mu\text{m}$  at nine different positions on the wafer. In (a) there are junctions with a width of  $100 \text{ nm}$ . In (b) there are junctions with a width of  $200 \text{ nm}$ .  $1 \mu\text{m}$  junctions are all open and also most of the  $2 \mu\text{m}$  junctions. Those which have survived are excluded due to their big resistance, for a better comparison of the resistances of the other junctions. Notice that the design length is not the real length of the junction due to the evaporation angle. At each of the nine positions there are identical junctions. One of them is always marked with a dot and the other one with a cross.

resistance. The averaged resistances for the different junction lengths are plotted in fig.44. In fig.45 the survival rates are plotted depending on the position on the wafer in (a), and depending

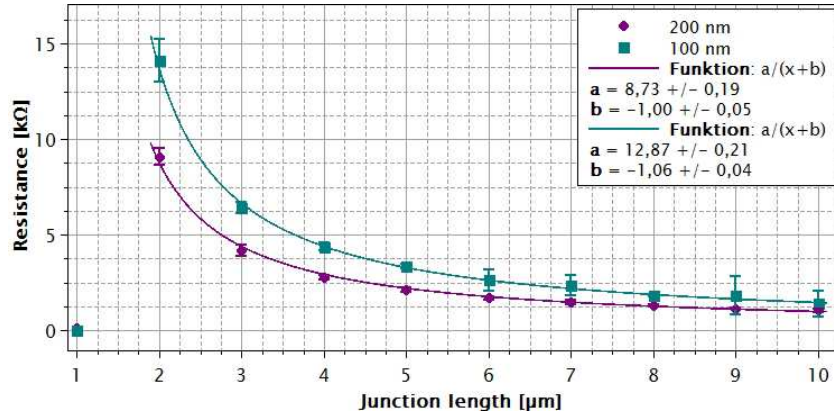


Figure 44: Averaged normal state resistances for the different junction sizes. The fit lines represent the  $\frac{1}{A}$  dependency of the normal state resistance on the junction area. The data points are plotted for the designed junction lengths and widths. The real junction areas are a bit smaller than the designed ones due to the evaporation angle for the aluminium layers and a small reduction of the junction area due to the thickness of the first evaporation layer on the side of the polymer mask. The difference between the designed and real junction area is represented with the fit parameter  $b$ . It is in both cases about  $-1 \mu\text{m}$ . Most of the area gets lost because of the evaporation angle. The real junctions are therefore about  $1 \mu\text{m}$  shorter than the designed junction lengths.

on the length of the junction in (b). We can see in (a), that on the right hand side of the wafer, the junctions are more likely to survive than on the left. This could have different reasons. It could be due to not uniformly spincoated polymer layers. At some point the height of the polymer layer



doesn't fit to the dose factors anymore and the junctions don't come out right. It could also be due to some shifts or changes on the electron beam during lithography. In this case the structures were written in the order the positions are labelled. It looks like the beam improves over time, but then during the movement from one end of the wafer to the other side (from position 3 to 4 and from position 6 to 7) something happened that the qubits aren't working anymore before it improves again. Most of the junctions at position 2 are a bit higher in resistance than the average of those

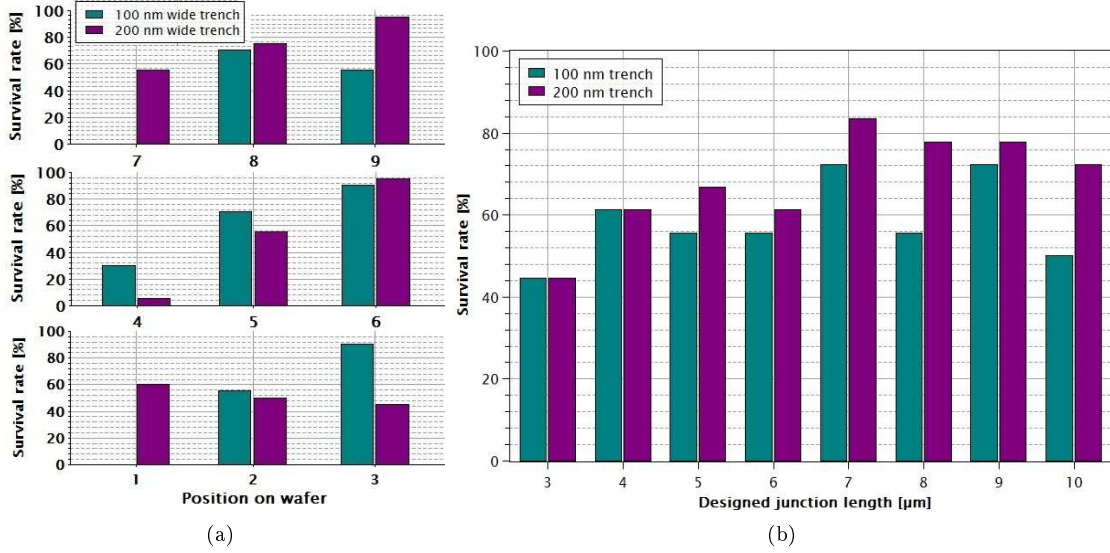


Figure 45: (a) Survival rates of the junctions with a 100 nm wide trench and with a 200 nm wide trench depending on their position on the wafer. The numbers to the wafer position correspond to the position in fig.42. One can see that more junctions survived on the right of the wafer. (b) Survival rates of the junctions with a 100 nm wide trench and with a 200 nm wide trench depending on the length of the junction. For each length the 200 nm wide trench junctions are more likely to survive, which is especially visible for bigger junctions.

junctions at the other positions. All in all, it looks like there are a few positions at which the fabrication failed at some point. The resistance values and therefore the reproducibility over the wafer can change a bit. In general no real tendency, how the resistances or the junctions change over the wafer, is visible.

Comparing the 100 nm wide junction areas with the 200 nm wide junction areas, we can say that in total more of the 200 nm wide junctions have survived. They also seem to be a bit more stable in resistance. In both cases there is a tendency, that bigger junctions survive more often than small ones, as shown in fig.45 (b). Very big junctions, like the 10  $\mu\text{m}$  junctions, then again are more likely to not survive.

## 10.2 Dose test on sapphire - KC003329

On this wafer a dose test was written to get an idea at which doses to start, to get a working qubit on sapphire. In fig.46 the design of the "qubit chains" on the wafer is shown. There are two rows with twelve columns. In the upper row the junctions have a trench width of 120 nm, in the lower row they have a trench width of 150 nm. Each column consists of ten contiguous qubits with junction lengths from 1  $\mu\text{m}$  to 10  $\mu\text{m}$ . The very first and the very last column are qubits fabricated with the "old doses" from the silicon wafer (see. tab.12), to compare them to the new ones. The design with the old doses was put on each side of the wafer to see if there is a variation of the dose across it. For the rest of the columns the dose factor for each element of the qubit is increased by +0,25, every column from left to right. Therefore, beside the first and last columns, there are no two identical qubits. There are 200 junctions with different dose factor combinations. In tab.13 the dose values for the different columns are shown.

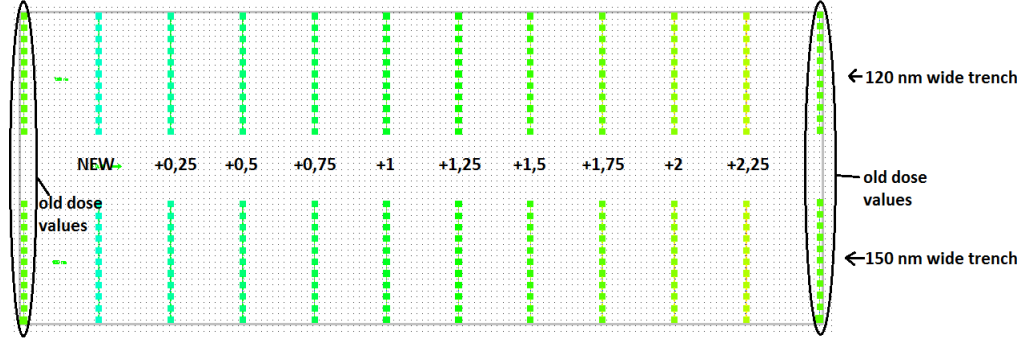


Figure 46: A screenshot of the design for the dose test which is written on the sapphire wafer KC003329. There are two rows with 12 lines of 10 qubits each with junction lengths from  $1\text{ }\mu\text{m}$  -  $10\text{ }\mu\text{m}$ . The very first and last lines are qubits with the dose values from tab.12. Between them the dose values increase by +0,25 from line to line, starting with the 'NEW dose' values from tab.13.

Table 13: Dose factors for the different design elements of a qubit on the sapphire wafer KC003329. The dark yellow marked values are those which are chosen to look the best and are set as the new dose factors for the next fabrication.

Dose:		+0,25	+0,5	+0,75	+1	+1,25	+1,5	+1,75	+2	+2,25
	2,75	3	3,25	3,5	3,75	4	4,25	<b>4,5</b>	4,75	5
	3,25	3,5	3,75	4	4,25	4,5	<b>4,75</b>	5	5,25	5,5
	3,75	4	4,25	4,5	4,75	<b>5</b>	5,25	5,5	5,75	6
	4	4,25	4,5	<b>4,75</b>	5	5,25	5,5	5,75	6	6,25
	4,25	4,5	4,75	5	<b>5,25</b>	5,5	5,75	6	6,25	6,5
	4,75	5	5,25	5,5	<b>5,75</b>	6	6,25	6,5		
	<b>1</b>	1	1	...						
	<b>1,4</b>	1,4	1,4	...						

**Pads, 3.- & 2.-connection-line:** In fig.47 the pads, the 3.-, the 2.- and a small section of the 1.-connection-lines to the junctions are shown for a selection of dose values. In the first picture one can clearly see the rough edges of the pad due to a too low dose. Also the transition to the 3.-connection-line is not developed at all and the 2.- and 1.-connection-lines also seem to be not perfectly developed. With increasing doses the edges of the pad get smoother and the corners turn from round corners into well pronounced sharp corners. The gap between the pad and the 1.-connection-line closes and also the lines itself become more pronounced. For a working qubit it is not really important to have good looking pads, but to know and make sure that you get what you design, it can be helpful to know how the different dose values come out in the used resist. In general, it should be as little dose as possible, to reduce back scattered electrons and the proximity effect, but as much as necessary, to develop with a high probability all the structures you want. Even if there is a bit of variation in the polymer thickness, or writefield alignment, or other not 100% perfectly reproducible procedure steps, you want to get your designed structures. Comparing the pictures, the elements marked with the blue arrow are chosen to be a good compromise between too low dose and too high dose. There the elements come out clearly, are connected to the other elements, but are not those with the highest dose values. They are somewhere in between and should be tolerant to some range of irregularities in fabrication. Those are the starting points for the next qubit fabrication and are also marked as the bold values coloured in dark yellow in tab.13.

**1.-connection-line & Junctions:** To find the dose values for the 1.-connection-line and the junction areas the  $8\text{ }\mu\text{m}$  long junctions for a selection of dose values are shown in fig.48. For the junctions with the 120 nm wide trench there are pictures after developing and after lift off. With those one can compare what is seen under the microscope after developing to what comes out in the end. One can get an idea how the structures should look like already after developing. For the



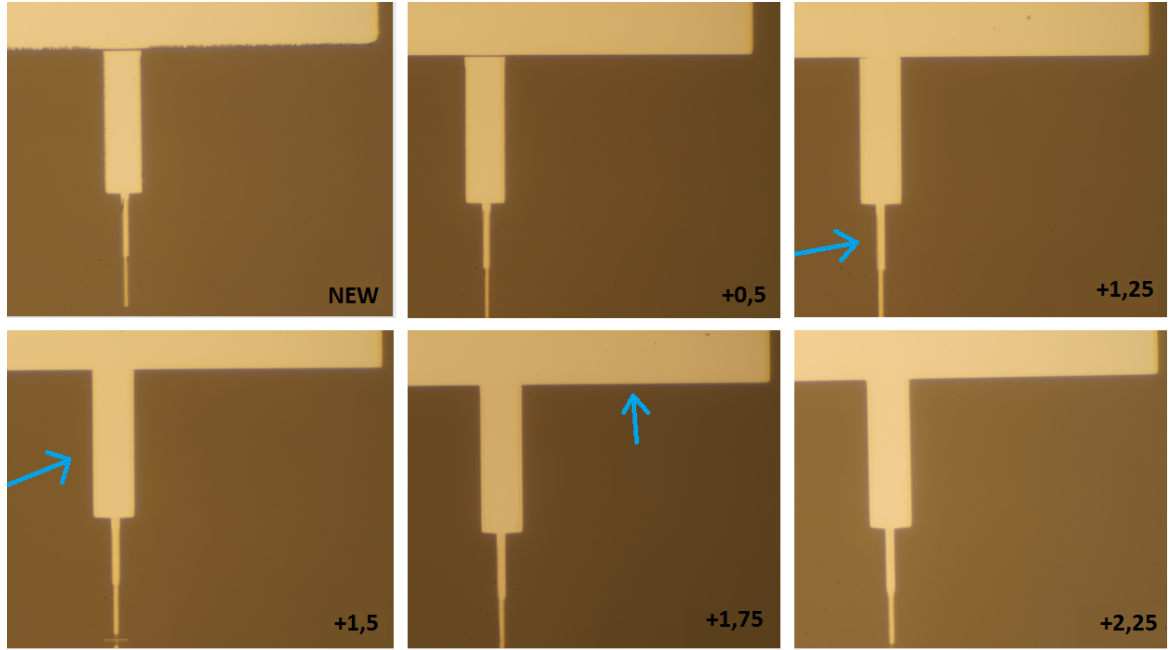


Figure 47: Microscope pictures of parts of the qubits on the sapphire wafer KC003329 written with different dose factors. One can see the lower end of the pad, the third, the second and a small section of the first connection line to the junction. The blue arrows mark the design elements with the corresponding dose which are chosen to look the best and will therefore be used for the next fabrication.

junctions with the 150 nm wide trench just the pictures after lift off are shown.

On the first pictures after developing one can already see, that there is too low dose to create a structure. The junctions are barely visible in the polymer as the chain breaking in the polymer only happened on top of the polymer layer. Going to the dose factor of 'NEW dose + 0,5' it looks like there is enough dose. Comparing it to the pictures after lift off, we see that it really creates a junction the first time, but it doesn't look very sharp edged and well pronounced. Increasing the dose factor by another +0,25 leads to junctions that look quite good, at least under the optical microscope. To be save within varying polymer layer thicknesses we choose the dose factor 'NEW dose +1' to be the starting point in the next dose test. It is marked with a blue arrow in fig.48.

For the 1.-connection-line it is more difficult to find a good dose factor for the junction area just from the pictures after developing. Comparing them to the pictures after lift off we can see, that the lines get thicker and thicker with increasing dose. A visible difference can be seen between the dose factors 'NEW dose +0,5' and 'NEW dose +0,75'. From this value up to the last dose factors the thickness doesn't seem to change a lot. On the last pictures with the highest dose factors there is with high probability much more dose than needed. Looking back, already a dose factor of 'NEW dose +0,75' creates nice cables with well pronounced edges. This dose factor (again marked with the blue arrow) is chosen to be the starting point for the dose test of the 1.-connection-line in the next fabrication run.

**Trenches:** For the trenches one has to be a bit more careful, as the cables created through this small gap are not "directly" evaporated at the position of the trench, but underneath a nearby overhang in the polymer mask. Not just the dose of the trench could have an influence on the outcome, but also the size of the trench, the thickness of the evaporated aluminium and the length of the junction area as well as the intentional and unintentional undercut. It is therefore the most sensitive part of the qubit to small changes in the fabrication.

The thickness of the evaporated aluminium changes the width of the trench. Is the trench too thin (or the aluminium too thick) it can happen, that the first evaporated aluminium layer closes the trench for the second cable so that it couldn't be created. One ends up with just one connecting

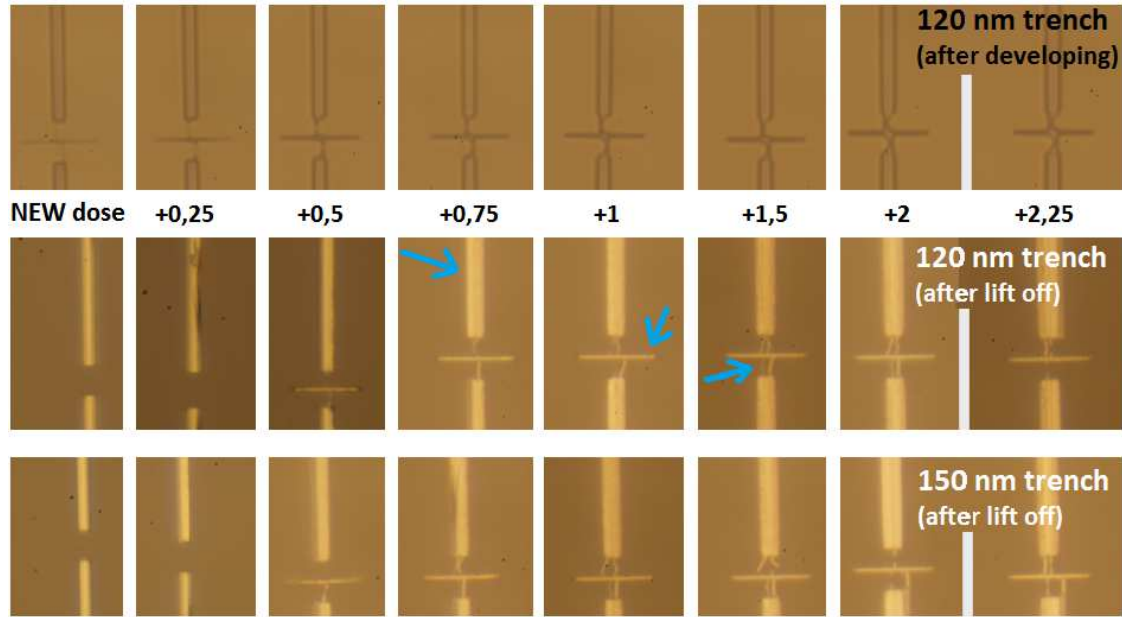


Figure 48: Microscope pictures of the  $8\ \mu\text{m}$  junctions for different dose factors. The first row pictures are the junctions with a  $120\ \text{nm}$  wide trench after developing. The second row are the same junctions, now after lift off. The third row are the  $8\ \mu\text{m}$  junctions with a  $150\ \text{nm}$  wide trench after lift off. With the blue arrows the design elements (the 1. connecting line, the junction area and the trench) with the corresponding dose values are marked which will be used in the next fabrication run.

cable. In this case, one evaporates either less aluminium or designs the trench a bit wider. The evaporation rate and the trench therefore depend on each other.

The length of the junction has a small influence on the outcome of the trench. As shown in fig.49 (c) we can see a difference in the structure of the undercut overhang for different junction lengths. The picture above is a microscope picture of a  $10\ \mu\text{m}$  long junction after developing. The bottom picture shows a  $2\ \mu\text{m}$  long junction. With the arrows the parts which show the undercut overhang are marked. For the  $10\ \mu\text{m}$  long junction this undercut overhang has a rounder shape than for the  $2\ \mu\text{m}$  long junction. Both junctions are written with the same dose factors. The difference therefore has to be due to the size of the junction area. More dose because of the bigger junction area increases the proximity effect on the trench. The undercut near the junction sees more dose if the junction area is bigger. This is visible in the round corners of the undercut near the junction. The dose factor used as starting point for the dose test on the next wafer ('NEW dose +1,5') is marked with the blue arrow in fig.48. For this dose four wires are clearly visible connecting the junction area with the 1.-connection-line. Even if the cables doesn't come out correctly, we don't go to higher doses as it could be due to the thickness of the aluminium layers. For this evaporation the first layer is  $40\ \text{nm}$  thick and the second one has a thickness of  $60\ \text{nm}$ . Compared to the previous evaporation where the layers were  $25\ \text{nm} + 30\ \text{nm}$ , this time the aluminium is nearly twice as thick. For the next wafer we again reduce the thickness to  $30\ \text{nm} + 45\ \text{nm}$ .

**Why are there four cables?** Comparing the four cables of the junctions in fig.48 we see that some of them are aligned more in the center of the 1.-connection-line and others are further out. Especially at the last pictures with the highest dose factors, one can see, that the outer lines are not always at the same place, but seem to move a bit. The inner ones are stable at their position and have a cut in the middle. This cut is also visible a bit enlarged in fig.49 (a) and (b). It turns out that the lines with the cut are the lines we want. The additional "wobbling lines" are not the "real" connecting cables. But why some of them have a cut at all? And what are these extra lines? In fig.49 (a) an optical microscope picture of a junction after lift off and after developing is shown. The cut seems to be quite in the middle of the evaporated cable. Something has to be in the

middle of the undercut overhang (marked with green) that prevents the aluminium to reach the wafer during evaporation. The proximity effect of the junction area and the 1.-connection line would result in an excess dose at the end of the undercut. In the middle between the 1.-connection-line and the junction area the proximity effect would be the smallest. This means that the undercut there is smaller than on the sides. If the undercut is too small, the aluminium gets evaporated just on the polymer wall of the mask. And doesn't reach the wafer. This would result in a "cut" in the connecting line. The cut in the center is therefore probably due to the round shape of the undercut overhang.

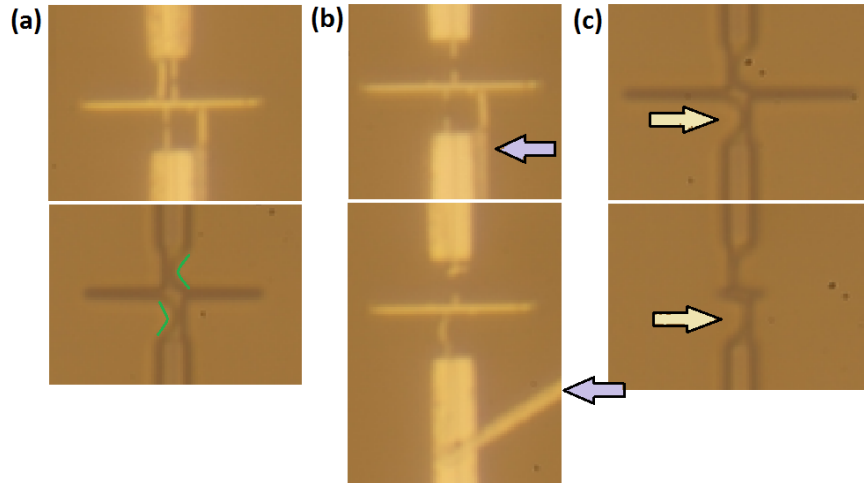


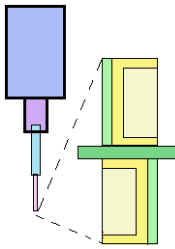
Figure 49: (a) Four lines connecting the junction area with the 1.-connection-line. Two of them have a cut in the middle. Those are the lines we want. If we compare the lines to the polymer mask, shown below, we can suspect that the cut originates from the undercut structure in the polymer mask (marked with green). If the undercut is too small, the aluminium is just evaporated on the mask and can't reach the wafer to create the cable. (b) Following the theory of evaporated aluminium on the wall of the polymer mask, it could either fall down on the structures, fall in the other direction away from the structures as on the picture above (see violet arrow), or stand away as visible on the picture below (also marked with a violet arrow). (c) shows the difference in the shape of the undercut, for a 10  $\mu\text{m}$  long junction and a 2  $\mu\text{m}$  long junction. The undercut structures are marked with the yellow arrows. The doses are the same for both junctions. The rounder edges of the undercut structure for the 10  $\mu\text{m}$  junction is probably due to the proximity effect coming from the bigger junction areas.

**What are these "wobbling lines"?** To find out what these extra cables are and where they come from let's have a look at the pictures in fig.49 (b) and the upper picture in (a). Sometimes the lines are just next to the cables with the gap, sometimes they are further out and continue along the side of the 1.-connection-line and sometimes they point away in random directions. In (b) these features are marked with the violet arrows. Most likely these extra lines are aluminium evaporated on the wall of the qubit mask. It should be removed during the lift off step, but somehow stay behind. If it is strongly connected to the aluminium layer on the wafer so that it doesn't lift off, it could fall on the structures (fig.49 (a)), open up (upper picture in fig.49 (b)), or point away (picture below in fig.49 (b)) because just a part of the aluminium sticks to the aluminium on the wafer. The wobbling lines therefore are with high probability the aluminium layers from the wall of the polymer mask. If this residual aluminium connects the "wrong" junction layer and connection-line it can result in a short of the junction and the junction wouldn't work. Therefore the goal for the next fabrication run is to get rid of this extra lines.

### 10.3 Having a closer look with the e-beam - KC003326

On this wafer another, a bit smaller dose test, but in general designed like the one in fig.46, is written. Starting with the dark yellow marked dose factors of tab.13, the doses for the 1.-connection-line, the trench and the junction area, are varied by increasing the dose factor about +0,25 each time, as you can see in tab.14. The difference to the previous dose test is, that now the dose factors for the trench and the doses for the junction area and the 1.-connection-line are higher than before. The proximity effect on the undercut should be higher and the undercut therefore a bit wider. This should hopefully avoid the gap in the connecting cables. The "old doses" used for the very first and the very last line are again the values from tab.12. In addition to the pictures

Table 14: Dose factors for the wafer KC003326.

Doses:		NEW	+0,25	+0,5	+0,75	+1
	<i>Pads</i>	4,5	4,5	...		
	<i>3.-connection-line</i>	4,75	4,75	...		
	<i>2.-connection-line</i>	5	5	...		
	<i>1.-connection-line</i>	4,75	5	5,25	5,5	5,75
	<i>Junction area</i>	5,25	5,5	5,75	6	6,25
	<i>Trench</i>	5,75	6	6,25	6,5	6,75
	<i>Undercut correction</i>	1	1	...		
	<i>Undercut</i>	1,4	1,4	...		

with an optical microscope also e-beam pictures of the junctions are shown. With the e-beam pictures we now have a more detailed look at the junctions and can better see what's going on.

**Aluminium bars next to the junction:** Let's start with the "wobbling lines" that appeared on the previous wafer and see if we find them again on this wafer. In fig.50 optical microscope pictures of the 6  $\mu\text{m}$  long junctions with a trench width of 120 nm, after developing and after lift off, are shown for the different dose factors. In addition there are also pictures of the junctions under the e-beam microscope. Focusing on the pictures after lift off there seem to be again some extra lines. This time even closer to the wanted evaporated cables. Also on the e-beam pictures this extra lines are visible. They are marked in green on the first picture, but can be found on each one.

In fig.51, e-beam pictures of junctions taken under different inclinations of the beam, are shown. Those provide a different view on the junctions and a better spatial representation of what's going on. (a) is zoomed in on one of this extra lines, again coloured in green. In the previous chapter we had the theory, that these extra lines are aluminium layers from the wall of the polymer mask. Looking at this picture in fig.51 (a) this theory is confirmed. It looks like the aluminium layer has detached from the wall which was washed away during the lift off and fell over in the direction of the evaporated connecting cable. On two corners we can also see the connection of this aluminium layer to the 1.-connection-line and to the junction itself. Looking at the design it makes sense, that these aluminium layers come from the wall of the polymer mask. They appear just on the side of the connecting cable where the trench is written. The connection to the junction area and the 1.-connection-line could be an indication of too much dose that creates an unwanted undercut. If the evaporation from the side that should completely go on the wall of the trench reaches the wafer, it would be connected to the junction area, as it is the case for this junctions.

On the previous wafer we also saw this "extra lines" further away from the connecting cable or even pointing away in random directions. Also this can be seen on the e-beam pictures and explained with the same theory. Marked with the blue circles in fig.50, there sometimes appear white edges on the 1.-connection-line and at the ends of the junction area. Again a zoom on the junction (see fig.51 (b)) shows what's going on. The white areas we found, are features that point away from the qubit structures on the wafer. On the first picture the aluminium layer from the polymer wall of the upper trench hasn't folded up, but still stands upright. The one of the trench below the junction area folded over onto the evaporated cable. If this aluminium layer falls in the other direction, away from the evaporated trench, it would be visible as the extra lines further out. Also

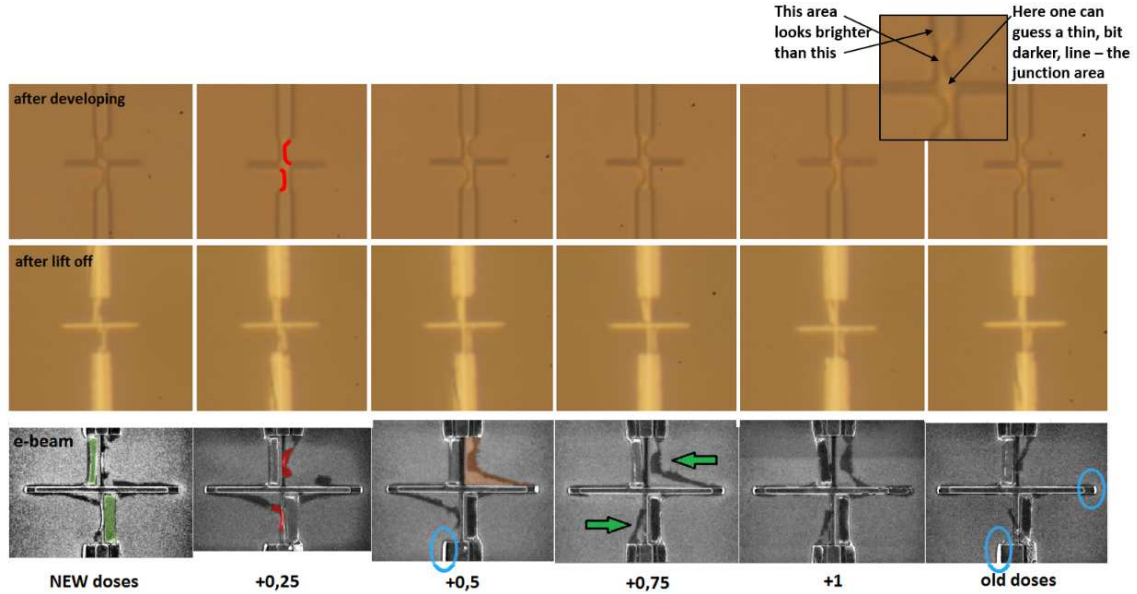


Figure 50: In the first two rows there are optical microscope pictures of the  $6\mu\text{m}$  long junctions with a trench width of 120 nm, after developing and after lift off, for different dose factors. In the last row there are e-beam pictures of each junction after measuring the normal state resistance. The e-beam pictures were taken with the settings: WD = 8.6 mm, Signal = InlenseDuo, Aperture Size =  $30\mu\text{m}$ , EHT = 3 kV. The coloured features are described in the text.

at the ends of the junction area the extra parts of aluminium from the polymer wall could stick to the structures on the wafer.

**Shadows on the e-beam pictures:** On the e-beam pictures in fig.50 there are further artefacts visible that should not be there, like the shadow-like black structures, marked on one picture with the green arrows. In the pictures, showing the junctions with the 'NEW dose' and the 'NEW dose +0,25' values, these "shadows" are even on top of the connecting cable. With increasing dose, they seem to move away from the cable. The junction with the 'old dose' factors looks the best, regarding these shadows. On the zoomed in pictures of fig.51 a) and b) these shadow structures are also visible. They are false coloured in blue. They have a rough edge on the side away from the cable, and a more sharp edge on the side close to the cable. If we look close enough, also under the aluminium layers that flipped over, there seems to be such a shadow structure. Especially in the picture in b) it looks as if the shadows were standing initially like a bridge collapsed onto the wafer.

My hypothesis to this shadows is, that they are the aluminium oxide layers of a bit of aluminium, that settles down underneath the undercut, while evaporating the cable into the undercut (The whole wafer is upside down during the evaporation and tilted by an angle of  $30^\circ$ ). According to this theory, the oxide layer has to start to loosen from the polymer mask during the lift off and remains on the substrate as now really some kind of shadow of the undercut. If this hypothesis is true, this shadows show more or less exactly where and how deep the undercut is developed, without looking directly into the undercut. In conclusion, this means that, by looking again at the e-beam pictures of fig.50, the undercut extends to the ends of the junction area. The whole area bordered by the junction area, the cable and the shadow (indicated with the orange area on the third e-beam picture), is an undercut in the written polymer mask.

Having a look at the undercut of a stitching error on the pads, marked with the red arrow in fig.51 c), makes this "big" undercut areas near the junction conceivable. Even there an undercut is visible, though the dose is much lower than for the structures of the junction.

**Additional shadows, or the same as those next to the junctions?** In fig.52 e-beam pictures of a part of the 1.- and the 2.-connection-cable in a) and the corner of a pad in b) are shown. On

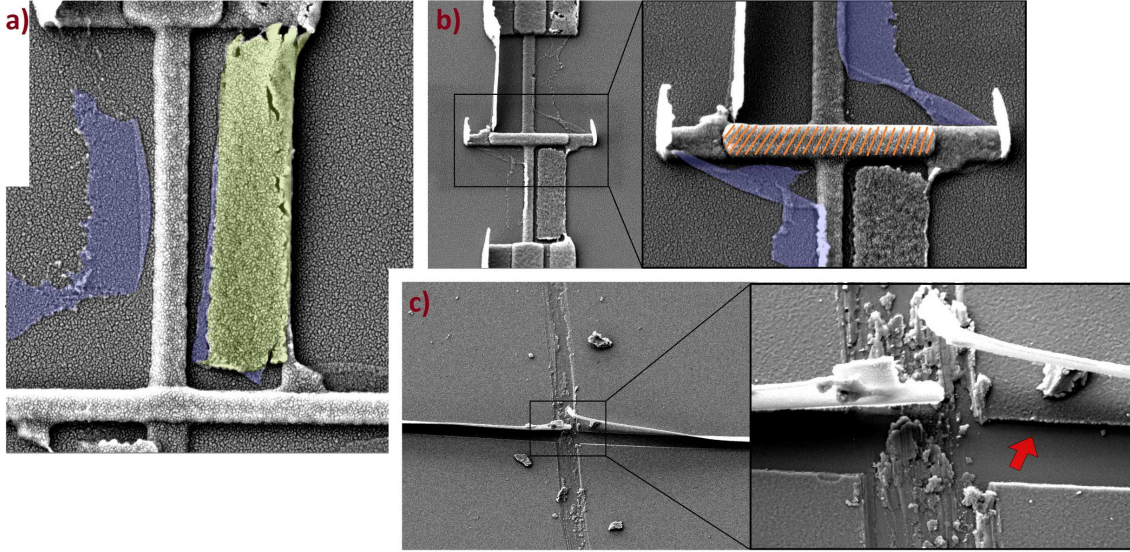


Figure 51: All of the pictures are taken with the following settings for the e-beam: Signal = SE2, Aperture Size =  $30\text{ }\mu\text{m}$ , EHT = 3 kV. Just the working distance (WD) is a bit different. For (a) I used WD = 6 mm, for (b) WD = 7,6 mm and for (c) WD = 7,8 mm. In a) a zoom on the upper cable of the  $2\text{ }\mu\text{m}$  long junction with a trench of 150 nm for the 'old dose' values under an angle of  $30^\circ$  is shown. (Notice that the junctions with the old dose values are designed mirrored. For them the lower cable is evaporated first.) The collapsed aluminium layer of the trench wall, coloured in green, is nicely visible. On the other side of the cable, coloured in blue, one can see the shadow like structure. It is just visible with the high resolution of the e-beam. In b) the  $2\text{ }\mu\text{m}$  long junction with the 150 nm wide trench and the 'NEW dose' values under an angle of  $53^\circ$  is shown. The wall of the upper trench is still standing whereas the lower one is already collapsed. Also at the ends of the junction area the evaporated aluminium layers on the wall are still standing and did not lift off. As in a) here also the shadow like structures are visible and coloured in blue. Especially in the zoomed in picture it looks as if it's somehow folded up. We also can see, that the real junction area, marked with orange, is not the same as the designed one. Due to the angle under which the junction is evaporated small parts at the ends of the junction area are missing. In c) a picture of the stitching error on the pad of the same junction as in b) is shown. The line from top to bottom is scratched with the needle used for measuring the resistance of the junction. It cuts the aluminium layer which was on top of the stitching error. On the zoomed in picture it is nicely visible that already the dose factor of 4,5, which was used for this pad, creates an undercut as marked with the red arrow.

the sides again aluminium layers remained behind from the polymer mask. Under these aluminium layers from the wall, structures are visible which look like the shadow structures near the junctions. Unfortunately one can not see, if these shadows are on one side above the folded down Al layers and on the other side beneath the Al layers, or if it is the same on both sides. If it is different on the two sides, the shadows could be, as before, thin oxidized layers of aluminium that settled down on the side of the structure during the evaporation. If it is the same on both sides, then we don't know where this structures come from. Then maybe also the theory for the shadows at the positions of the undercut isn't the right one. To be sure this has to be investigated further.

**Real junction areas:** Another thing, that is now visible on the junction areas with the e-beam pictures, is that the real junction area, marked with orange in fig.51, is not exactly the designed one. Depending on the height of the polymer layers and the angle under which the junction is evaporated there is always some loss of area at the ends of the junction. We measured this missing junction area for a few junctions and get a length of about  $780 \pm 30\text{ nm}$ , which is missing in the length of the junction area for this fabrication process with an evaporation angle of  $30^\circ$ . This should be taken into account when comparing the designed values to the measured values. Later



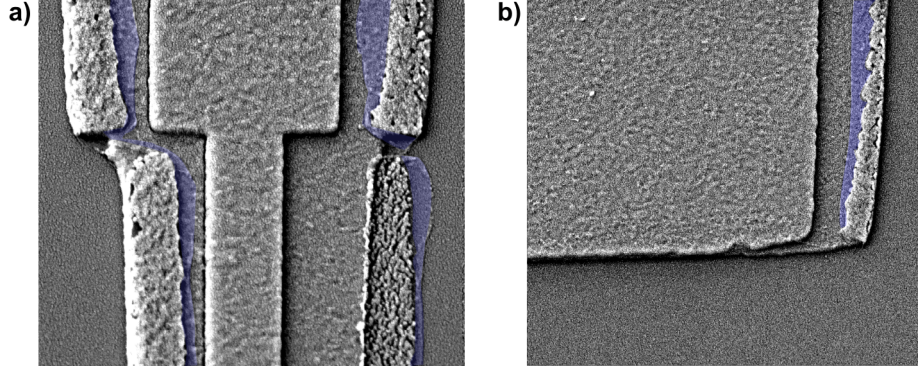


Figure 52: a) E-beam picture of the 2.- and 3.-connection-line with the aluminium layers fallen down from the wall. b) E-beam picture of a corner of a pad. In blue the structures are coloured which look the same as the shadow like structures near the junction. Pictures are taken with the settings: WD = 9.6 mm, Signal = SE2, Aperture Size = 30  $\mu\text{m}$ , EHT = 3 kV.

on we also found out, that the measuring tool in the software of the e-beam machine was calibrated a bit incorrectly. The measured lengths therefore has to be multiplied with a factor 1,25 to get the real lengths. In our case this would be  $975 \pm 38$  nm that are missing in length of the junctions. Looking back at fig.44, where we found that the junctions should theoretically be about 1  $\mu\text{m}$  shorter according to the resistance values, we now found the explanation. It is due to the used polymer thickness and evaporation angle. The measured  $975 \pm 38$  nm fit quite well to the fitted 1  $\mu\text{m}$  from fig.44.

**Different interpretation of microscope pictures:** Comparing the e-beam pictures of the junctions with the pictures after developing in fig.50, the outline of the undercut seems to fit the shadows on the e-beam pictures, as marked with the red lines. But then, why isn't a big spot of aluminium evaporated in the center of the junction area, as it should be according to the round shapes of the outlines? The zoomed in picture in fig.50 provides a closer look at the undercut structures. There seems to be a part which looks a bit brighter than, for example, the developed structures of the 1.-connection-lines. In the center of the junction area, there is a thin line which again looks a bit darker. This means, that we most likely had a kind of wrong interpretation of what we see on the microscope pictures. It seems that the outline of the undercut in the polymer mask after developing shows the upper edge of the undercut in the first polymer layer. The brighter areas show the second polymer layer on top of the first one. They define the sharp and straight edges of the trench and the junction area, despite the big undercut area (orange area in fig.50).

The shadows seem to become smaller with increasing dose. This could be explained by the increasing designed undercut with increasing dose. In the pictures after developing this is visible in the more round shaped structures of the undercut, meaning that the undercut overhang is mainly the second polymer layer, the PMMA, and less of the first evaporated Copolymer MMA.

**Normal state resistances:** In fig.53 the measured normal state resistances of the junctions for the different dose factors are plotted against the designed junction length. The measurement error is about  $\pm 0,1$  k $\Omega$ . For the junctions in (a) the 4  $\mu\text{m}$  and 9  $\mu\text{m}$  long junctions aren't working because of a stitching error at these junctions. For the junctions in (b) stitching errors appear at the junctions with 10  $\mu\text{m}$  and 5  $\mu\text{m}$  length. Comparing the plots for the junctions with the 120 nm wide trench in (a) and the junctions with the 150 nm wide trench in (b), one can see that nearly all of the junctions in (b) are short or open. Just a few of the junctions with the 'NEW dose' factors, and the 1  $\mu\text{m}$  long junction with the dose factor 'NEW dose +1', seem to work. Apparently the wider trench leads to a short in the junction. The highest dose factor for the junctions with the 120 nm wide trench also lead to a short for all junction sizes. For this or higher dose values the gap broadens too much and the junctions get shorted.

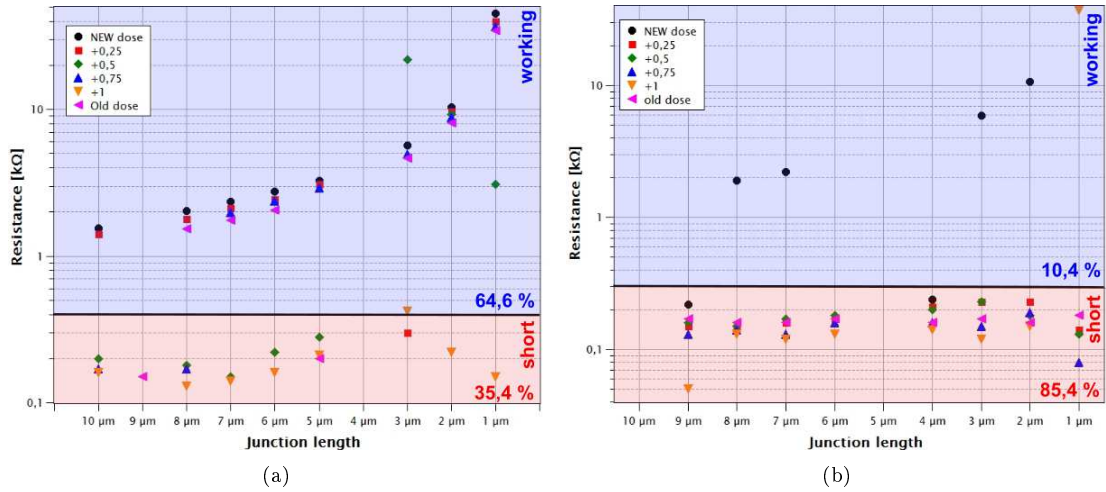


Figure 53: In (a) the normal state resistance of all the junctions from the wafer KC003326 with the 120 nm wide trench, which weren't open, are plotted for the different dose factors. In (b) the resistances of all the junctions with a 150 nm wide trench are plotted. For the 4 μm and 9 μm long junctions in (a) and the 5 μm and 10 μm long junctions in (b) there are no resistances because a stitching error happened at these junctions during the e-beam lithography. The value of 0,3 kΩ is chosen to be the limit for a working junctions. All junctions with a resistance lower than 0,3 kΩ are considered shorted. This region is coloured in red. The region for the working junctions is coloured in blue. The design with the 120 nm wide trench seems to work better than the design with the 150 nm wide trench according to the amount of junctions that had survived and are working in both of the plots. For the 150 nm wide trench junctions in (b) just a few of the junctions with the 'NEW dose' factor and the 1 μm junction with the dose factor 'NEW dose +1' have survived.

**What do the junctions to the resistances look like?** To have a better feeling how the junctions for the measured resistances look like, junctions with a 120 nm trench and the 'NEW dose' values are shown in fig.54. Despite the unwanted aluminium bars near the connecting cable, the junctions seem to work and deliver resistances. If one really wants to use these junctions is another question. Therefore, measuring a normal state resistance is not a 100% indication, that the junction is a good one.

One can also ask, if the resistances are really the ones we want to know - through the junction, or if they are a combination of resistances through the junction AND through the aluminium bar? If the bars are really just oxide, then the resistance is high and the result is only slightly distorted as the main part of the resistance value comes from the junction.



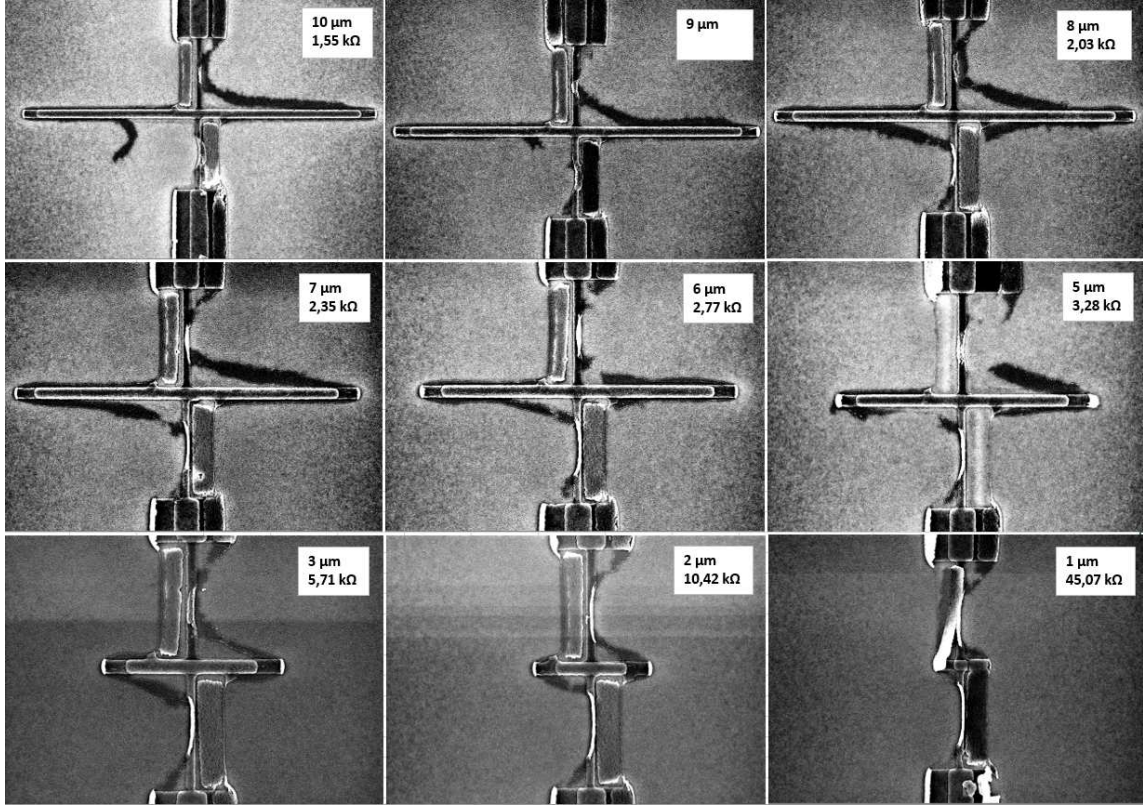


Figure 54: The e-beam pictures were taken with the settings: WD = 8.6 mm, Signal = InlenseDuo, Aperture Size = 30  $\mu\text{m}$ , EHT = 3 kV. Those are the junctions with a 120 nm wide trench and the 'NEW dose' values on the wafer KC003326. The 4  $\mu\text{m}$  and the 9  $\mu\text{m}$  long junctions are not working because of a stitching error during lithography. Here only the 9  $\mu\text{m}$  long junction is shown. For the other junctions the measured normal state resistance is written in the upper right corner. Although there are the shadow like structures on the connecting cables and the aluminium layers of the trench wall next to the cables, the junctions provide useful resistances. Nevertheless these qubits aren't something one wants to use, even though the junctions seem to work.

## 10.4 Reproduction of the previous wafer - KC003361

On this wafer the same design and the same doses as on the wafer KC003326 (see tab.14) were used, but a few small changes in the fabrication steps were done.

**Aging of the junctions:** One of the changes was made because of the "growing" normal state resistance of the junctions over time. This is not only observable for our junctions. Also in the general superconducting circuit community they noticed this kind of "ageing" of the junctions. There is the theory, that this ageing after fabrication originates in a change of the aluminium surface while slowly oxidizing in air. In the previous chapter 9.5 this ageing was shown in the example of the wafer KC003368. There the resistances of the junctions grow about 40% over a period of nearly five months (see fig.41).

In detail, two mechanisms are known which could be responsible for this aging. One is the continuing oxidation of the junction barrier in air. This happens mostly near the circumference of the junction. The other one is that the  $\text{AlO}_x$  barrier is rich of oxygen and just slowly relaxes to the stable  $\text{Al}_2\text{O}_3$  by a diffusive mass transport from the oxygen rich surface to the aluminium. [28]

Therefore we tried to add an extra oxidation step (3 min, 20 mbar) after the aluminium evaporations in the Plassys, as some kind of "capping layer", to immediately stop or prevent this oxidizing and the increasing of the resistances. On this wafer I tried the capping layer the first time and changed the recipe by adding this step. This was then also done for the following wafers. Fig.41 shows measurements from a wafer with this capping layer. There are other ideas to prevent the

ageing of the qubits. Other groups found, that removing organic residues with an ion mill before the evaporation, could play a significant role for the ageing of the junctions. Also a long lift off (about several hours) in hot solvent "anneals" the junction and could prevent the ageing. [28]

**Changes in the lift off:** Another change was done in the lift off step. The wafer was put two times for 1 min at 35 kHz and 20% power in the Sonicator. The first time after 5 min in Aceton, and the second time after another "over night session" in Aceton. With the sonication the lift off was a bit more "brutal" than on the wafer before to hopefully remove the aluminium bars next to the trenches.

**Dirt on the qubits:** In fig.55 a qubit on the previous discussed wafer KC003326 and a qubit on this wafer KC003361 is shown. The difference of the surfaces is clearly visible. There is much

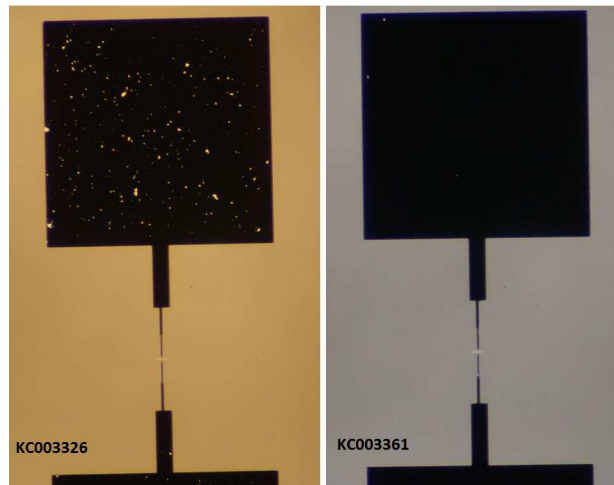


Figure 55: On the left a microscope picture of a qubit on the wafer KC003326 is shown. A lot of small particles are visible on the pads. This dirt can cause losses in the microwave measurements and therefore should not be there. On the right a microscope picture of a qubit from the wafer KC003361 is shown. During the fabrication on this wafer I took care to avoid particles possibly coming from all the liquids the wafer is in contact during fabrication.

more "dirt" and little unwanted particles on the wafer KC003326. These can cause losses in the microwave measurements and therefore decrease the lifetime of the qubit. To improve this I took care to keep the wafer clean during all of the procedure steps. Especially during steps with liquids as mentioned in chapter 9. These steps, where one has to put the wafer out of a liquid like lugol or the developer, seem to be the most critical ones. The point is, that the dirt doesn't add up once it is on the wafer, but can also be removed in each step. Every step is therefore critical on its own. Fig.55 shows the result for taking care of the steps.

**Comparison to previous wafer:** In fig.56 the junctions with the 120 nm wide trench and the 'NEW dose +0,25' on this wafer are compared to the junctions on the previous wafer. Since the design and the dose factors are the same on each wafer, the junctions this time should be a reproduction of the junctions on KC003326, or even better due to less "dirt" deposited during fabrication and the hopefully better lift off. Focusing on the aluminium bars next to the junctions, this time they are either gone completely or lie around further away from the junctions, marked with the blue arrows. Also on the 1.-connection-lines there are less of the extra aluminium layers. This could be an indication that the different lift off really makes an improvement.

**Dose comparison:** In fig.57 a dose comparison for the 5  $\mu\text{m}$  long junctions is shown. This time we compare the e-beam pictures taken with both of the two detectors for imaging available in the e-beam machine. In the upper row, pictures are taken with the InlenseDuo detector for the directly reflected electrons. In the bottom row the pictures are taken with the SE2 detector which

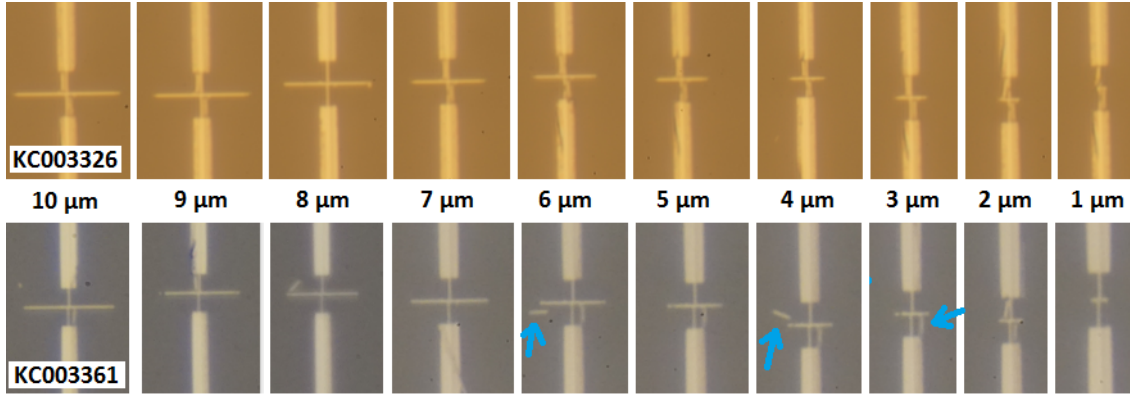


Figure 56: Microscope pictures of the junctions with the 120 nm trench and the 'NEW dose +0,25' factors for different junction lengths. Top row are the junctions from the previous wafer KC003326 shown to compare it to the junctions of this new fabrication run on the wafer KC003361, in the bottom row. The changes in the fabrication process are an extra oxidation step after the aluminium evaporation, sonication during the lift off step and the more carefully wafer handling with regard to small particles that may settle down on the structures.

detect the secondary electrons deflected from the surface. With the InlenseDuo detector nearly everything around the junction is visible. With the SE2 detector features on, or very close to the substrate are visible. Let's have a look at the aluminium bars next to the connecting line. In the SE2 pictures they seem to be gone completely for nearly all of the junctions. Comparing it to the InlenseDuo pictures we see, that this is not the case. They didn't lift off properly and seem to "fly" around, as they still stick to parts of the junction. Even if they are still there, it's an improvement to the last wafer, where all of them were lying next to the connection line.

Instead of the aluminium bars next to the connecting line we can now find that thin lines connect the junction area and the 1.-connection-line. They are marked with the blue circles on the first pictures in fig.57. We didn't recognise these lines on the previous wafer, but maybe just couldn't see them because of the aluminium bars. With these lines we can confirm that the first evaporation comes from the left. The evaporation from the left should create the upper connecting cable but should go onto the polymer wall through the trench connecting the junction area with the lower 1.-connection-line. Instead of being evaporated on the polymer wall the aluminium instead reaches the wafer. The first aluminium layer on top of the polymer mask makes the trench a bit smaller. Therefore the aluminium in the second evaporation doesn't reach the wafer anymore. Comparing the lines for the different doses on the SE2 pictures in fig.57 we can see, that also the second one of those lines appear. This is the point where the dose is that much, that the unwanted undercut at the polymer wall gets so big, that now the aluminium can reach the wafer. For the junctions with the 150 nm wide trench this happens a dose factor of 0,25 earlier than for the junctions with the 120 nm wide trench.

If these lines are really new on this wafer, it means that the fabrication is not as reproducible as we hoped. To get a hint if these lines are really new in this fabrication run, we can have a look at the resistances.

**Normal state resistances:** In fig.58 the normal state resistances of all junctions on this wafer are plotted. One time against the different junction lengths and one time against the different dose factors. The area with the junctions that are working is again coloured in blue, the area with the junctions that are short is coloured in red. The limit is again chosen to be 0,3 kΩ. At first glance one can see, that just a few junctions have survived. For both trench widths nearly all of them are open or short. The junctions with a trench width of 120 nm nevertheless seem to work a bit better. Comparing the dose factors most of the working junctions are written with the 'NEW dose' dose factors. In fig.57 we can see, why this is the case. According to the unwanted lines connecting the junction area with the 1.-connection-line and therefore creating a short, less dose works the best. Comparing the resistances to the resistances of the previous wafer, the fabrication seems to be

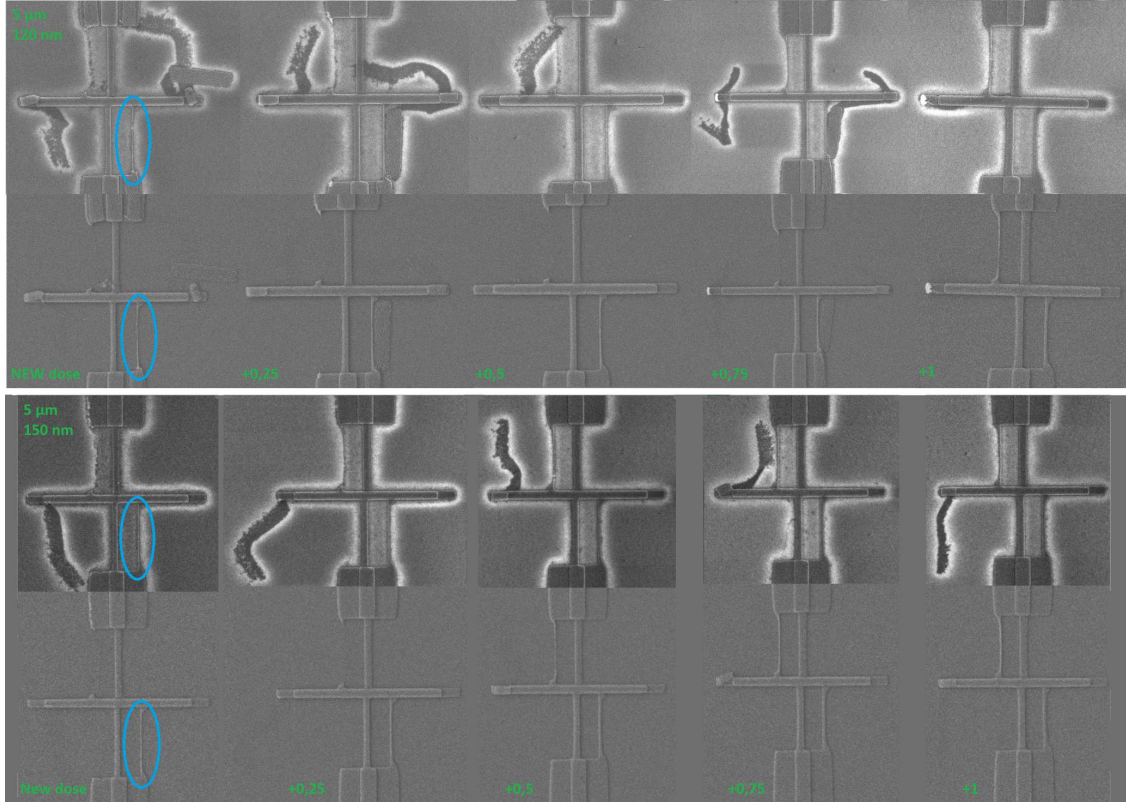


Figure 57: Comparison of the  $5\text{ }\mu\text{m}$  long junctions with a  $150\text{ nm}$  wide trench and different dose factors for the junction area, the trench and the 1. connection line. The dose factors are the same as for the previous wafer KC003326 in tab.14. The unwanted connecting lines are getting thicker and thicker with increasing doses. Also for the first picture with the lowest doses it seems to be too much dose somewhere because the unwanted connecting line appears. The big shadow like things that are floating around are just visible with the InlenseDuo detector and not with the second electron detector SE2. The parameters for the e-beam pictures are: Signal = InlenseDuo/SE2, EHT = 3 kV, WD = 5,6 mm, Aperture Size =  $30\text{ }\mu\text{m}$ . The upper row is taken with the InlenseDuo detector and the bottom row is taken with the SE2 detector.

even worse. For the  $150\text{ nm}$  wide trench junctions the result is about the same. Just a few of the junctions with the dose factor 'NEW dose' have survived. For the junctions with the  $120\text{ nm}$  wide trench there were more than twice as many junctions above the  $0,3\text{ k}\Omega$  limit than this time. Here most of the working junctions are written with the smallest dose factors, the 'NEW dose' dose factors.

One should have in mind, that the value of  $0,3\text{ k}\Omega$  was a choice according to the lowest resistances on the previous wafer. The percentages on the resistance plots refer to this value. Maybe the lowest resistance of the working  $10\text{ }\mu\text{m}$  long junctions would have been a better choice. At least these two wafers can be compared to each other even if the words "working" and "short" do not have to agree with the "real world".

**Compare junction lengths:** In fig.59 e-beam pictures of the  $1\text{ }\mu\text{m}$  -  $5\text{ }\mu\text{m}$  long junctions, a trench width of  $150\text{ nm}$  and the 'NEW dose' factors, once taken with the InlenseDuo and once taken with the SE2 detector, are shown. According to fig.58 the  $1\text{ }\mu\text{m}$ , the  $2\text{ }\mu\text{m}$  and the  $4\text{ }\mu\text{m}$  long junctions work and give acceptable resistances, whereas the other two junctions are short. For the  $5\text{ }\mu\text{m}$  long junction it is clear that this is because of the extra line from the junction area to the bottom 1.-connection-line. For the  $3\text{ }\mu\text{m}$  long junction it could be due to the big particles lying around on the evaporated connecting cable. Also here it is visible, that with increasing junction area, more dose is deposited. Therefore the proximity effect on the trench is also higher. At some



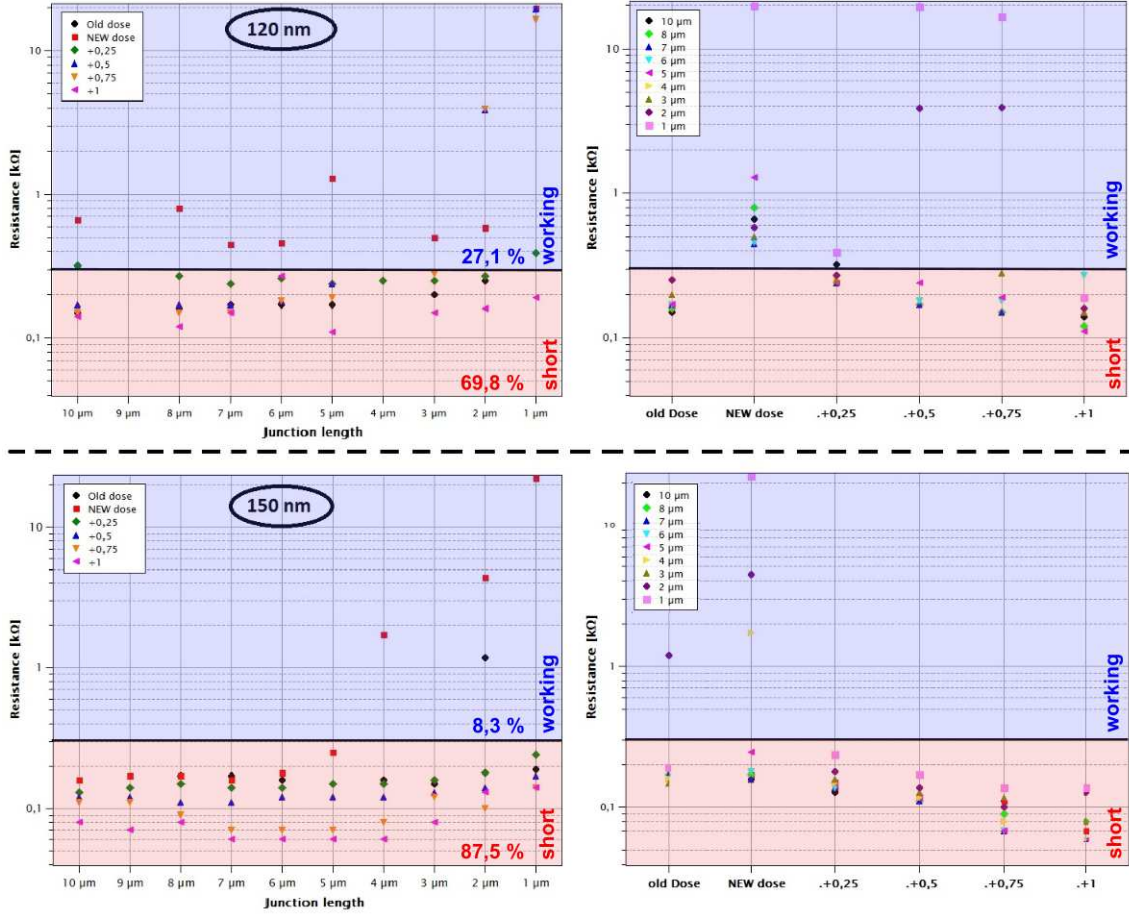


Figure 58: The first two plots are the normal state resistances from the junctions with the 120 nm wide trench. On the left the resistance is plotted against the junction length, on the right plotted against the different dose factors. For the 9  $\mu\text{m}$  long junctions there are no resistances because of a stitching error during lithography. Comparing the junction sizes, the 1  $\mu\text{m}$  and 2  $\mu\text{m}$  long junctions seem to work the best, as there are junctions with different dose factors alive. Their fabrication is therefore more stable for varying dose. Comparing the doses, the 'NEW dose' dose factors lead to the best results comparing all the junction sizes. The lower two plots are the normal state resistances of the junctions with the 150 nm wide trench. Here it looks as if just a few junctions with the dose factors 'NEW dose' and a few with the 'old doses' survived.

point the unwanted undercut is so big, that also this "extra cable" is evaporated on the substrate. One can observe how it builds up at the smaller junctions until it is clearly visible and connected for the 5  $\mu\text{m}$  long junction. Depending on what we want to fabricate in the end, we therefore have to adjust the dose factor to the junction length.

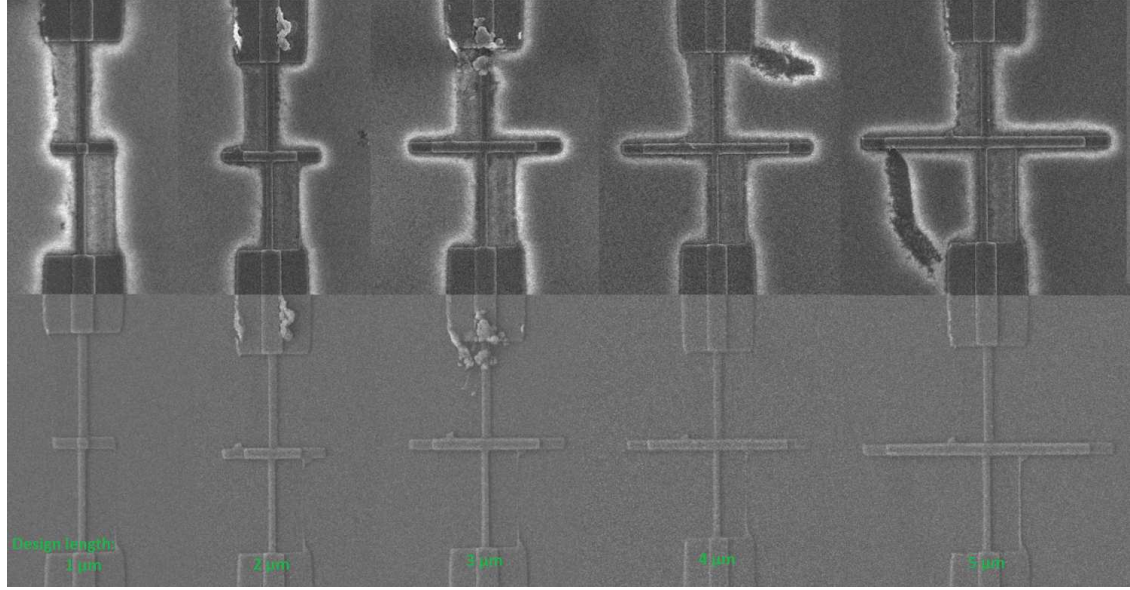
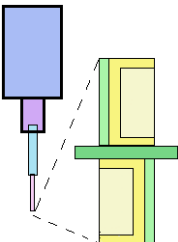


Figure 59: E-beam pictures of the junctions with a trench width of 150 nm and the dose factors 'NEW dose'. The top row are pictures taken with the InlenseDuo detector and the pictures in the bottom row are pictures taken with the SE2 detector. The other parameters for the pictures are: EHT = 3 kV, WD = 5,6 mm, Aperture Size = 30  $\mu$ m.

## 10.5 Last test - KC003364

Despite the small number of working junctions we got, we know why they aren't working. Therefore we are in general close to get a whole wafer of working junctions. The problem we have to get rid off are the aluminium bars and the thin extra lines connecting the junction area and the 1.-connection-line. To do so we have to avoid that aluminium that should go on the wall of the mask also reaches the wafer. This could be done by either reducing the unwanted undercut by decreasing the dose, changing the evaporation angle, or increasing the thickness of the polymer layers. The only change that can be done locally and doesn't affect the already working parts of the qubit, is to change the dose. Compared to the previous dose test we fix the dose factor for the junction area and just vary the dose factors for the 1.-connection-line and the trench. For the trench we lower the starting dose from 5,75 to 5 to hopefully get rid of the extra line. Additionally we compensate this missing "proximity effect dose" at the wanted undercut by increasing the dose factor for the undercut from 1,4 to 1,8. We also add a dose test for junctions with a 120 nm wide trench and an undercut dose of 1,6. The variation for the 1.-connection-line stays the same. A summary of the different dose factor combinations is given in tab.15. How the dose tests are arranged on the wafer is shown in fig.60.

Table 15: Dose factors for the wafer KC003364.

Doses:		NEW	+0,25	+0,5	+0,75	+1
	<i>Pads</i>	4,5	4,5	...		
	<i>3.-connection-line</i>	4,75	4,75	...		
	<i>2.-connection-line</i>	5	5	...		
	<i>1.-connection-line</i>	4,75	5	5,25	5,5	5,75
	<i>Junction area</i>	5,25	5,25	...		
	<i>Trench</i>	5	5,25	5,5	5,75	6
	<i>Undercut correction</i>	1	1	...		
	<i>Undercut</i>	1,8/1,6	1,8/1,6	...		

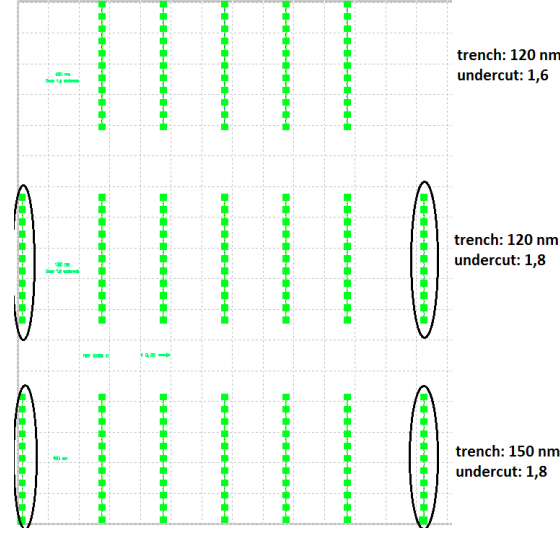


Figure 60: Design on the wafer KC003364. An additional row with a different undercut dose is written. The circled lines are qubits with the dose values of tab.12.

**Microscope pictures:** Let's start again with a look at the microscope pictures. In fig.61 the 5  $\mu\text{m}$  long junctions are shown for the different dose factors and the different trench widths. With the drawn up interpretation of the brighter and darker areas near the junction as the different polymer layers in section 10.3, one would expect a better outcome according to the undercut. The round structures, coloured in red on the first picture, are smaller than on the wafer before. They are nearly gone for the junctions with a 150 nm wide trench and the 'NEW dose +1' dose factor. The overhang of the undercut for those junctions is therefore mostly the second polymer layer. It is unlikely that the evaporated connecting lines are cut in the middle as on the wafer KC003329 or shadow like structures appear next to the cables as on the wafer KC003326.

**Resistances:** In the figures 62, 65 and 67 the normal state resistances of all the qubits on the wafer KC003364 are plotted. For the qubits with the 'NEW dose' factors, coloured in blue, red and green, pictures of the junctions are shown in fig.63, fig.64, fig.66 and fig.68. One last time we take a look at the junctions and see if the changes in the dose factors improve the outcome. According to the resistance measurements and the e-beam pictures we then decide which dose combination would be the best for the qubits we want to fabricate.

**120 nm wide trench, undercut dose factor 1,6:** For these junctions the resistance values (fig.62), especially for the smaller junctions, look quite stable. For the dose factors 'NEW dose' all junction lengths have survived and are in the correct order according to  $R_n \approx \frac{1}{A}$ . With increasing dose (for the trench and the 1.-connection-line) longer junctions seem to get a bit unstable. For the highest dose factors 'NEW dose +1' the junctions longer than 3  $\mu\text{m}$  are short.

In fig.63 e-beam pictures of the 3  $\mu\text{m}$  long junctions for the different dose factors are shown. According to their stable resistances one would expect, that all of them look quite good. But on the pictures one can again see aluminium bars lying around and thin lines that nearly connect the junction area with the 1.-connection-line. Have in mind, that these pictures are taken with the IntenseDuo detector so aluminium bars very close to the surface are visible. Comparing the very first and the very last picture shows the difference between the very first dose factors we were using and the improvement in fabrication with the dose factors we are using now. It is remarkable that already quite small changes in the dose factor have such an big impact on the outcome. For the 1.-connection-line we changed it from 5 to 4,75, for the junction area we changed it from 7,5 to 5, for the trench we changed it from 6,5 to 5 and for the undercut we changed it from 1,4 to 1,6. The dose factors for the trench and the undercut are those with the most impact on the outcome and therefore the most sensitive ones.

In fig.64 we can compare the junction lengths for the dose factors 'NEW dose'. The long junctions

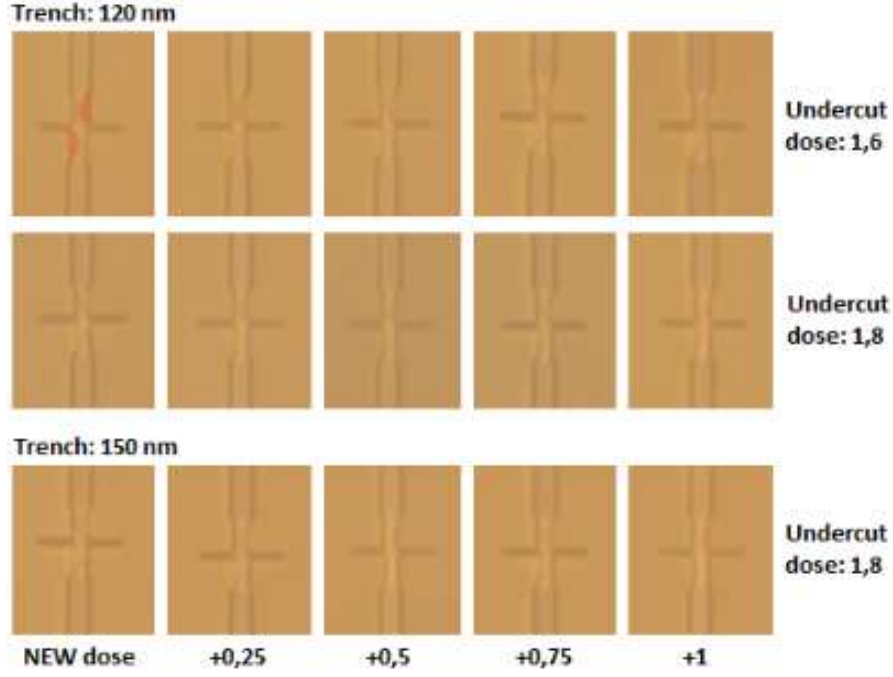


Figure 61: Microscope pictures of the 5  $\mu\text{m}$  long junctions for the different trench widths and dose factors.

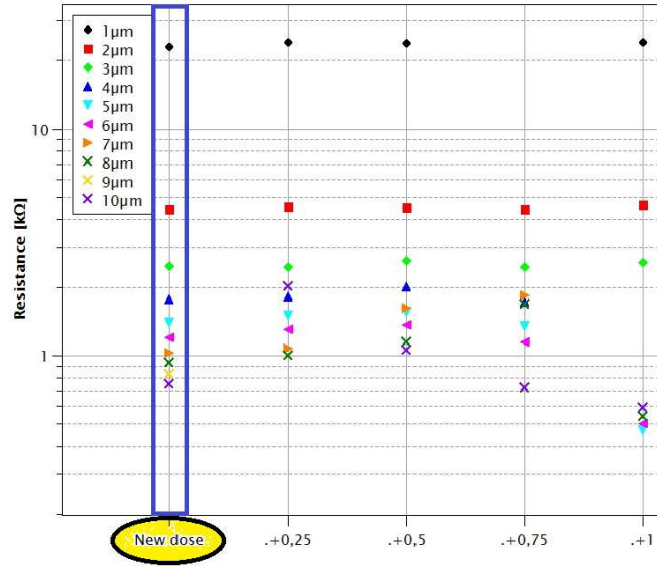


Figure 62: Normal state resistances of the junctions with the 120 nm wide trench and an undercut dose factor of 1,6. The measurement error is about  $\pm 0,2 \text{ k}\Omega$  for all junctions. The pictures of the blue coloured junctions can be found in fig.64. In fig.63 the 3  $\mu\text{m}$  long junctions for the different dose factors are shown. The circled dose factors 'NEW dose' are used to fabricate the qubits to cool down and measure in the fridge.

seem to come out better than the short ones. Therefore the aluminium bars next to the small junctions can't really be explained with too much dose as we did before. The aluminium bars have a somehow better connection to the junction area if the junction is small. It could be because the undercut reaches the ends of the junction area for small junctions whereas for long junctions this isn't the case. But for a full theory this single shot observations are not very reliable and should



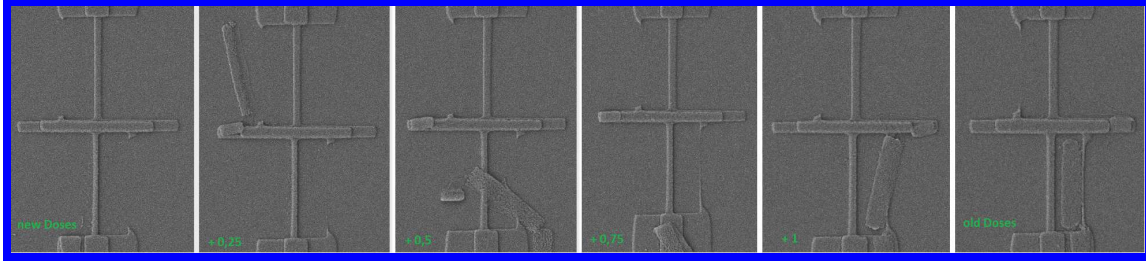


Figure 63: Comparison of the dose factors for a 3  $\mu\text{m}$  long junction with a 120 nm wide design trench. The undercut dose in this case is 1,6.

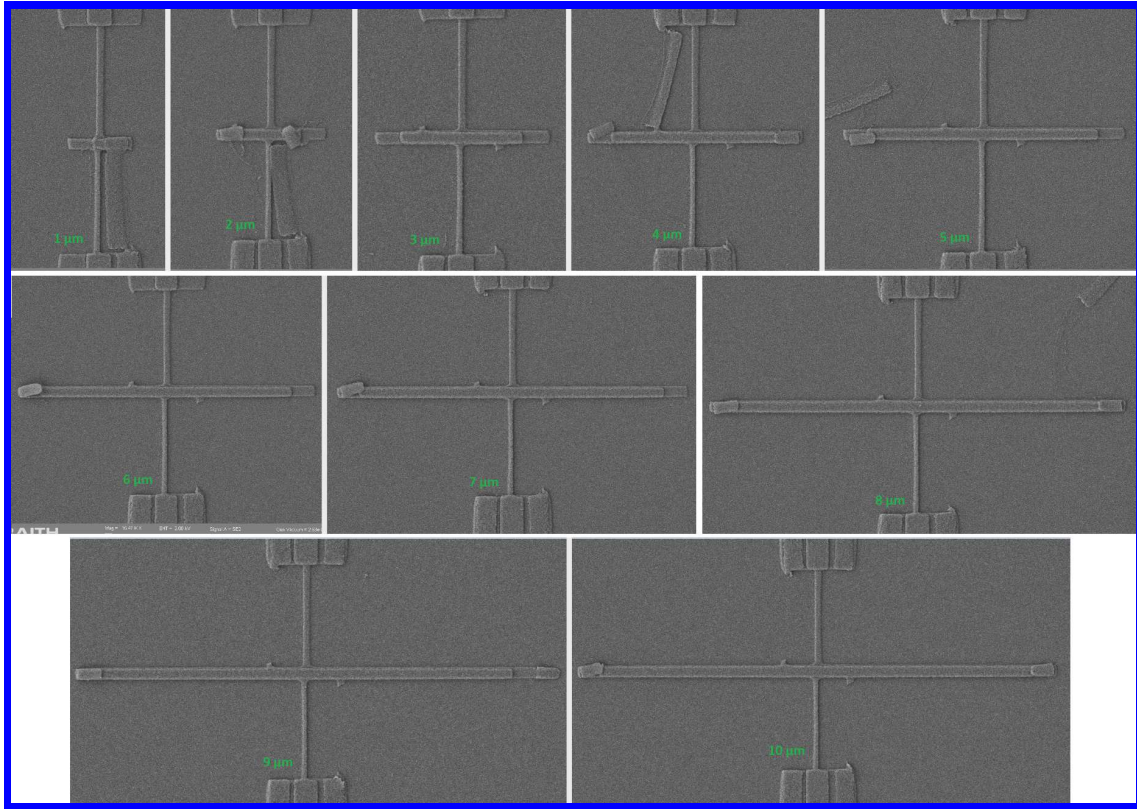


Figure 64: Comparison of the junction sizes for the junctions with a trench width of 120 nm, an undercut dose of 1,6 and the 'NEW dose' dose factors

be investigated further.

**120 nm wide trench, undercut dose factor 1,8:** The only change for this junctions is the dose of the undercut. Due to this small change of just 0,2 in the undercut dose factor we would expect a similar outcome as for the previous junctions. In fig 65 the normal state resistances are plotted and in fig.66 some of the junctions with the 'NEW dose' dose factors are shown.

The longer junctions provide more stability than before according to the resistances. Taking the averaged resistance, for the 10  $\mu\text{m}$  long junctions and the first three dose variations, gives a resistance of  $0,67 \pm 0,03 \text{ k}\Omega$ . We can correct the value of  $0,3 \text{ k}\Omega$  as the limit of a working junction that we have chosen before to this  $0,67 \pm 0,03 \text{ k}\Omega$ . All junctions with resistance values now smaller than  $0,67 \pm 0,03 \text{ k}\Omega$  are short-circuited and don't provide reliable resistances and good working junctions.

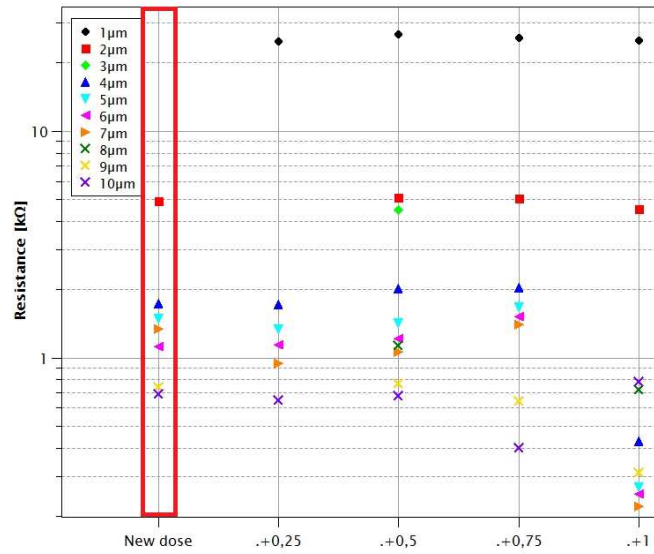


Figure 65: Normal state resistances of the junctions with the 120 nm wide trench and an undercut dose factor of 1,8. The measurement error is about  $\pm 0,2 \text{ k}\Omega$  for all junctions. The pictures of the red coloured junctions can be found in fig.66.

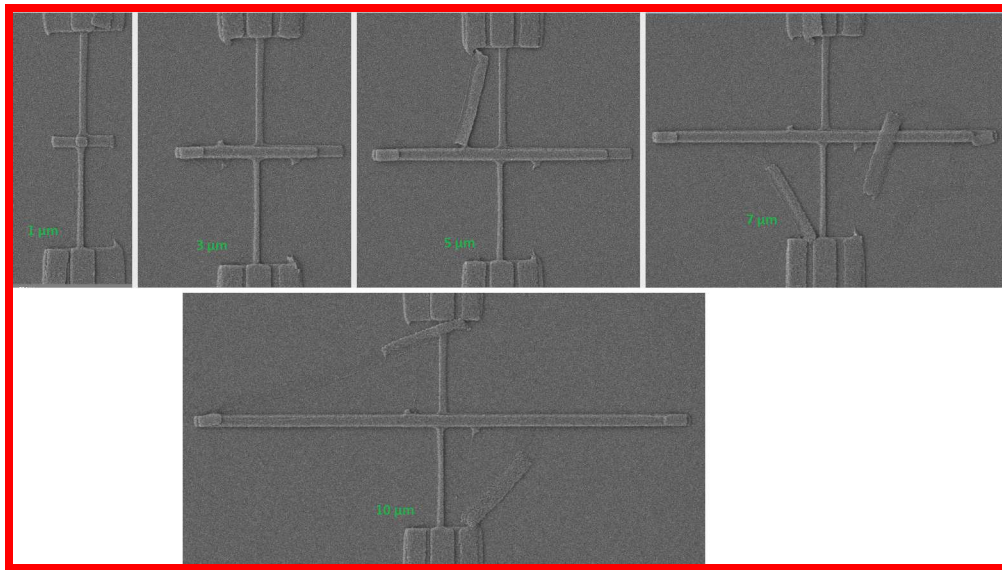


Figure 66: Comparison of the junction sizes for the junctions with a trench width of 120 nm, an undercut dose of 1,8 and the 'NEW dose' dose factors

**150 nm wide trench:** The junctions with the 150 nm wide trench seem to work quite well for the 'NEW dose' and the 'NEW dose + 0,25' dose factors (see fig.67). For higher dose factors all of the junctions, except the 1  $\mu\text{m}$  long junctions, are short-circuited. Having a look at the pictures of the junctions with the 'NEW dose' factors in fig.68, we can explain why this is the case. Already for this lowest dose factors the first evaporation creates the thin short for the longer junctions. We therefore can assume that for the dose factors 'NEW dose +0,5' and bigger, this connection also appears for the small junctions.

Remarkable for the 150 nm wide trench junctions is, that nearly no aluminium bars are around the junction and even on top of the 1.-connection-line no aluminium bars from the wall are visible.

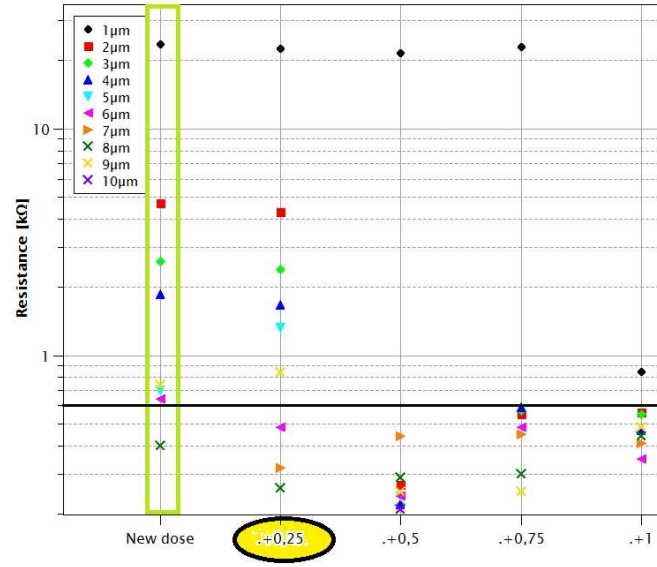


Figure 67: Normal state resistances of the junctions with the 150 nm wide trench and an undercut dose factor of 1,8. The measurement error is about  $\pm 0,2 \text{ k}\Omega$  for all junctions. The pictures of the green coloured junctions can be found in fig.68. The circled dose factors 'NEW dose +0,25' are used to fabricate the qubits to cool down and measure in the fridge.

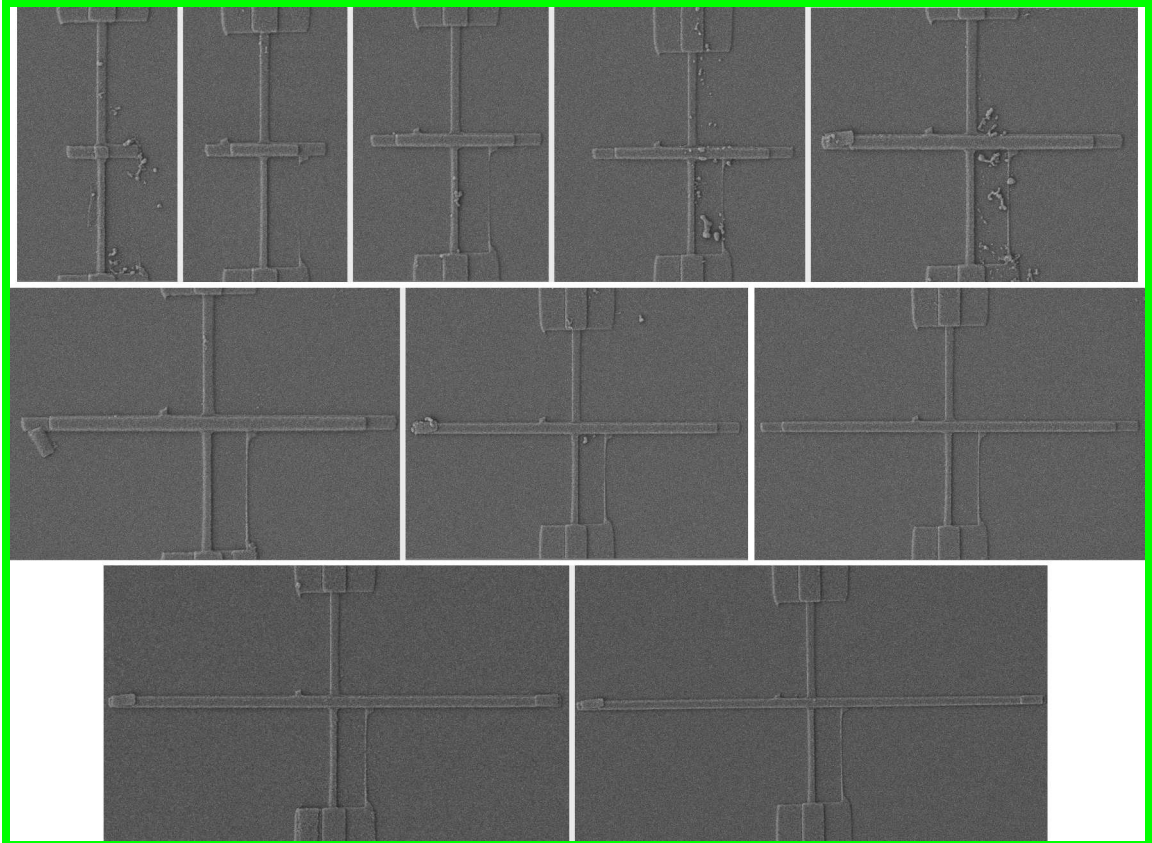


Figure 68: Comparison of the junction sizes from  $1 \mu\text{m}$  to  $10 \mu\text{m}$  for junctions with a trench width of 150 nm, an undercut dose of 1,8 and for the 'NEW dose' dose factors.

**Dose factors and junction lengths to cool down:** In chapter 7.2 we had the example of a transmon that should work at a frequency of 8 GHz. As we will see later, this would be a good choice for the waveguide we want to use. To get a qubit transition frequency of 8 GHz we need a junction with an inductance of about  $L = 7$  nH, corresponding to the simulated capacitance. The resistance therefore should be about 6 k $\Omega$ . According to the measured resistances so far this corresponds to a designed junction length a bit smaller than 2  $\mu\text{m}$ . We know that the junctions age a bit over time, so we decided to make them a bit longer. To have a variety we also decided to write qubits with two different junction lengths.

## 10.6 Take aways of the fabrication progress

Before we now go to the last two wafers with the qubits we want to cool down, here is a short summary of some take aways:

1. Take care of dirt during the fabrication, especially in the steps with liquids!
2. The junction length has an influence on the dose  $\rightarrow$  proximity effect!
3. Be brave in the lift off step! - The junctions won't die that easily!
4. One can see the two different polymer layers already under the optical microscope!
5. For a new design and the probably new dose test  $\rightarrow$  have a closer look on the junctions with the e-beam microscope! Don't completely trust the resistance values, see also how they look like!

## 10.7 Qubits to cool down - KC003368 & KC003369

In this chapter the dose factors, the exact dimensions of the design elements and how the qubit chips are arranged on the wafer, are given. After fabrication the qubit chips has to be diced apart. This was done at the *KIT* (Karlsruher Institute for Technology). In the dicing marks we also integrated junctions to get some statistics to the survival rate and the resistances of the qubits over the wafer. The design was written twice to make sure that enough qubits survive the fabrication and the dicing.

### 10.7.1 Design of the measured qubits

In fig.69 screenshots of the design elements are labelled with the dimensions and coloured corresponding to the dose factors. The  $2,5\ \mu\text{m}$  long junctions have a trench width of  $120\ \text{nm}$  and the

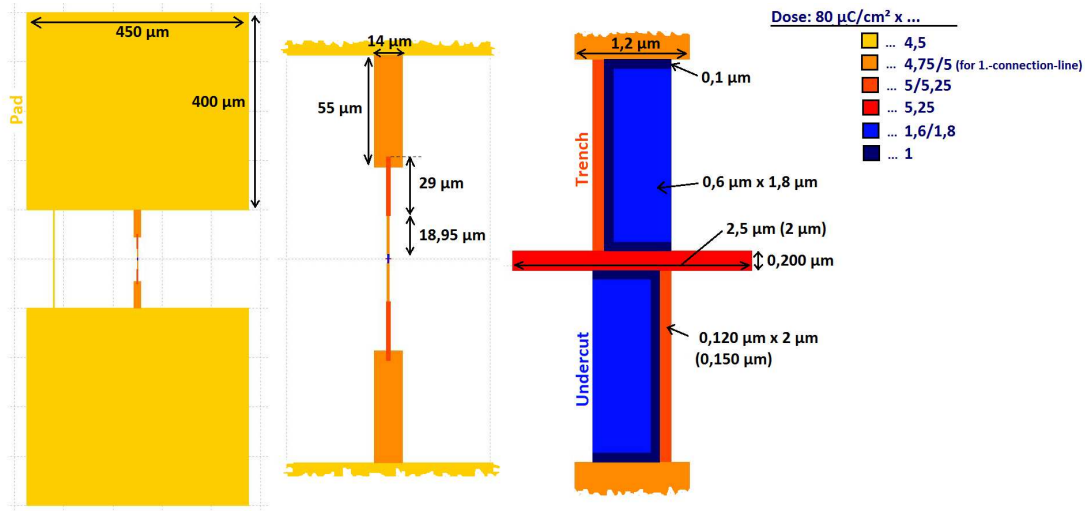


Figure 69: Screenshots of the design elements in the Raith software. The dimensions of the different design elements are labelled. The colours indicate the different dose values with which the structures are written with the e-beam. The dose factor of 1,6 for the undercut corresponds to the sketched qubit with a trench width of  $120\ \text{nm}$  and a junction length of  $2,5\ \mu\text{m}$ . The 1,8 dose factor for the undercut corresponds to the junctions with a  $150\ \text{nm}$  wide trench and a junction length of  $2\ \mu\text{m}$ .

dose factors are given by the first number. For the  $2\ \mu\text{m}$  long junctions the trench has a width of  $150\ \text{nm}$  and the dose factors are the second number. If there is only one number the dose is the same for both qubit designs.

The pads and the 3.-connection-line are written in  $1000\ \mu\text{m} \times 1000\ \mu\text{m}$  writefields with a magnification of  $130\times$  and the  $120\ \mu\text{m}$  aperture. The other design elements are written in  $100\ \mu\text{m} \times 100\ \mu\text{m}$  writefields with a magnification of  $1300\times$  and the  $10\ \mu\text{m}$  aperture.

In fig.70 the design for a fabrication run on a whole wafer with the dimensions of the "qubit chips" is shown. There are two rows of qubit chips. Starting with the  $2,5\ \mu\text{m}$  long junction, the two junction sizes are placed alternating over the wafer so that one can fabricate 20 qubits at the same time. As the qubits in the center are intentionally shortened to not die during the dicing, there were also junctions fabricated between the dicing marks to see if the qubits are working without cutting the short.

**Dicing mark junctions:** From measuring the normal state resistances of the dicing marks, we can get a benchmark of the normal state resistance of the qubits used in the experiment at the center of the chip. In fig.71 the resistances of all the dicing mark junctions, measured in the order shown on the picture in the left corner, are plotted. We can compare if and how the resistances change with their position on the wafer, if there is a difference between the qubits in the first and in the second row on the wafer and see if the resistances on the two wafers are the same. This



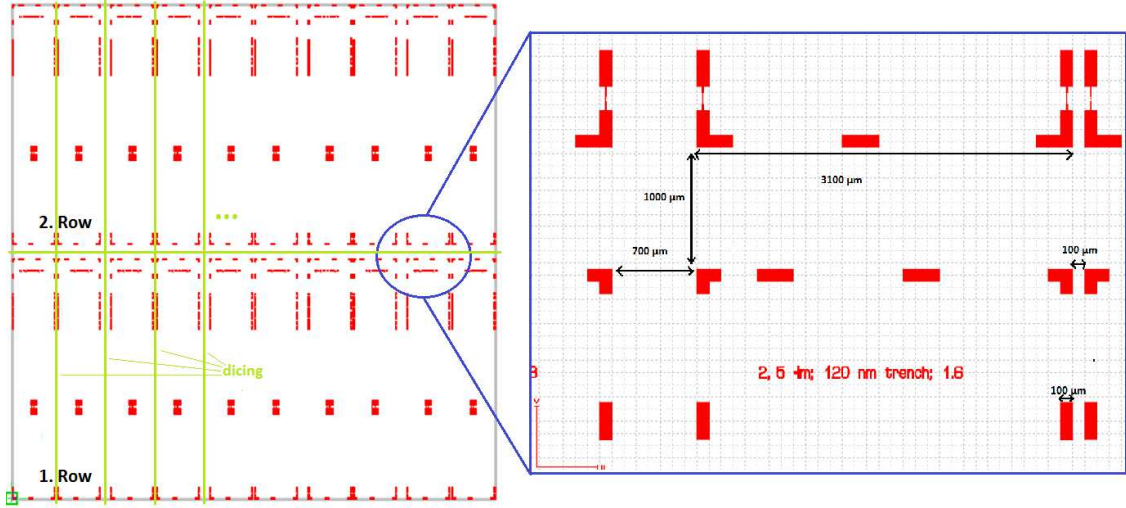


Figure 70: The design of the "qubit chips" on a wafer. One row is alternating between a qubit with a  $200 \text{ nm} \times 2,5 \text{ } \mu\text{m}$  junction area and a qubit with a  $200 \text{ nm} \times 2 \text{ } \mu\text{m}$  junction area. On the edge of each qubit chip there are test junctions which are used as dicing marks and to test if the fabrication process worked. On the right, the dimensions of the chip design are shown. The lines for dicing are marked in green.

will tell us how reproducible our fabrication process is and we can compare the survival rates and resistance spreads of the two different junction lengths. Let's start with the  $2 \text{ } \mu\text{m}$  long junctions. In the second row (purple and yellow triangles) their resistances are visibly higher than those in

Table 16: Normal state resistance statistics of the wafer KC003368 and KC003369.

	2,5 $\mu\text{m}$ , 120 nm	2 $\mu\text{m}$ , 150 nm	2,5 $\mu\text{m}$ , 120 nm	2 $\mu\text{m}$ , 150 nm
<b>1. row:</b>				
$\varnothing R_n [k\Omega]$ :	$3,3 \pm 0,2$	$4,6 \pm 0,2$	$3,2 \pm 0,2$	$4,3 \pm 0,2$
Survived:	55% (33/60)	98,33% (59/60)	91,67% (55/60)	100% (60/60)
<b>2. row:</b>				
$\varnothing R_n [k\Omega]$ :	$3,3 \pm 0,1$	$4,9 \pm 0,3$	$3,27 \pm 0,07$	$4,6 \pm 0,7$
Survived:	11,67% (7/60)	93,33% (56/60)	26,67% (16/60)	81,67% (49/60)
<b>Total:</b>				
$\varnothing R_n [k\Omega]$ :	$3,3 \pm 0,2$	$4,7 \pm 0,4$	$3,2 \pm 0,2$	$4,5 \pm 0,5$
Survived:	33,33% (40/120)	95,83% (115/120)	59,17% (71/120)	90,83% (109/120)
	<b>KC003368</b>		<b>KC003369</b>	

the first row. This is the same on KC003368 and KC003369. For the longer junctions this is not observable, but maybe there are just not enough data points to see it.

A possible explanation could be the drift of some e-beam parameters over time. The time at which a junction is written could therefore make a difference, if the junction design isn't resistant enough against small dose variations. In fig.72 the averaged resistances of the dicing mark junctions on each chip are plotted in the order they are exposed. For both wafers and both junction lengths the resistances tend to grow when they are written at a later time.

Another explanation could be the position of the test junctions on the wafer. For the first row most of the junctions are placed in the middle of the wafer, as for the second row they are more on the edge of the wafer. The fact, that the polymer layers in the center of the wafer are slightly thinner than on the edge could lead to the higher resistances of the test junctions in the second row. Thicker polymer layers lead to smaller junction areas (compared to the junctions with the same dose, but thinner polymer layers) which lead to higher resistances. The qubits in the center of the chip are then probably somewhere between those resistances of the first and the second row.

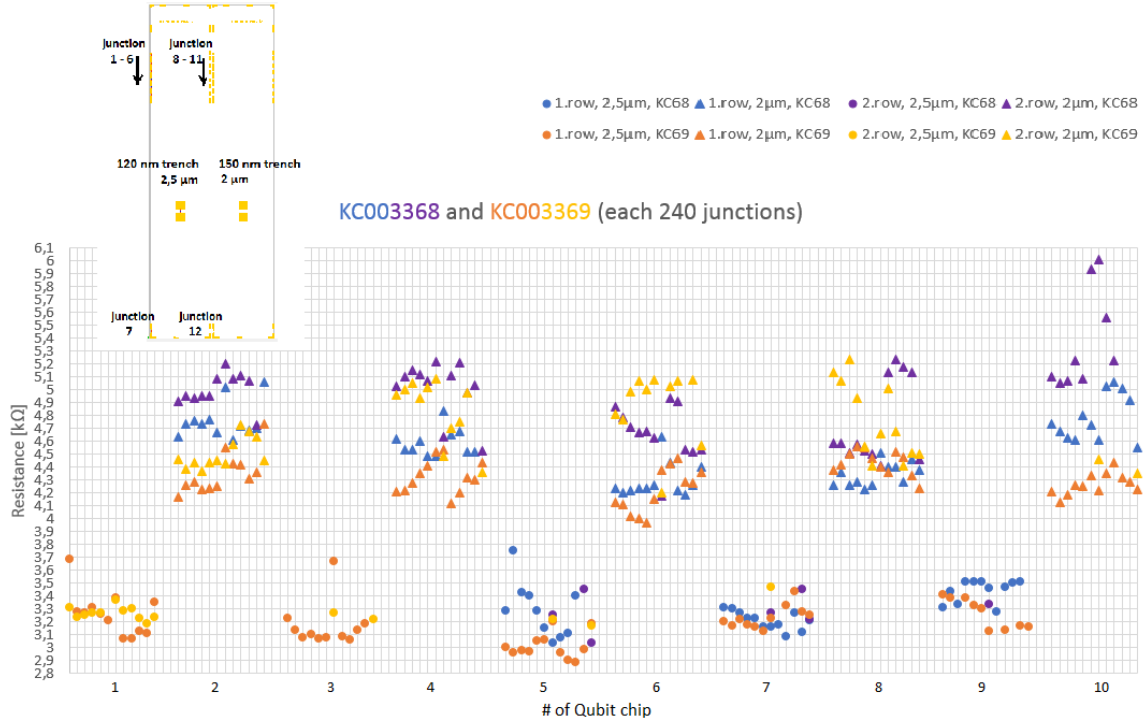


Figure 71: Resistances of the test junctions from the wafer KC003368 and KC003369. From left to right the points correspond to the test junctions according to the position on the wafer. The small picture in the left corner shows the order how the junctions were measured. Each "accumulation" of resistances therefore represent one qubit chip. The two qubit designs are placed alternating over the wafer. The blue and violet points represent the junctions in the first and second row of the wafer KC003368. The orange and yellow points represent the junctions in the first and second row of the wafer KC003369. Circles indicate the  $2,5 \mu\text{m}$  long junctions and triangles indicate the  $2 \mu\text{m}$  long junctions.

On three of the four plots in fig.72 the resistances in the center are a bit lower than on the edges. In the second row on wafer KC003369 this is not visible. It could therefore just be coincidence, that the rest of the resistances fit the theory. To conclude, it is most likely that both explanations play a role and that the resulting change in resistance is a combination of both.

In tab.16 the averaged resistances and the survival rates of the different junction designs for each row on the two wafers are shown. On both wafers more than 90% of the qubits with the  $2 \mu\text{m}$  long junction survived. Their averaged resistance is about  $4,7 \pm 0,4 \text{ k}\Omega$  on wafer KC003368 and  $4,5 \pm 0,5 \text{ k}\Omega$  on wafer KC003369. The  $2,5 \mu\text{m}$  long junctions seem not that reproducible. For those junctions just 33,3% survived on KC003368 and 59,2% on KC003369. Comparing the resistances for the first and the second row on the wafer, we find that notably fewer of the junctions in the second row survived. Also for the smaller sizes fewer junctions in the second row survived.

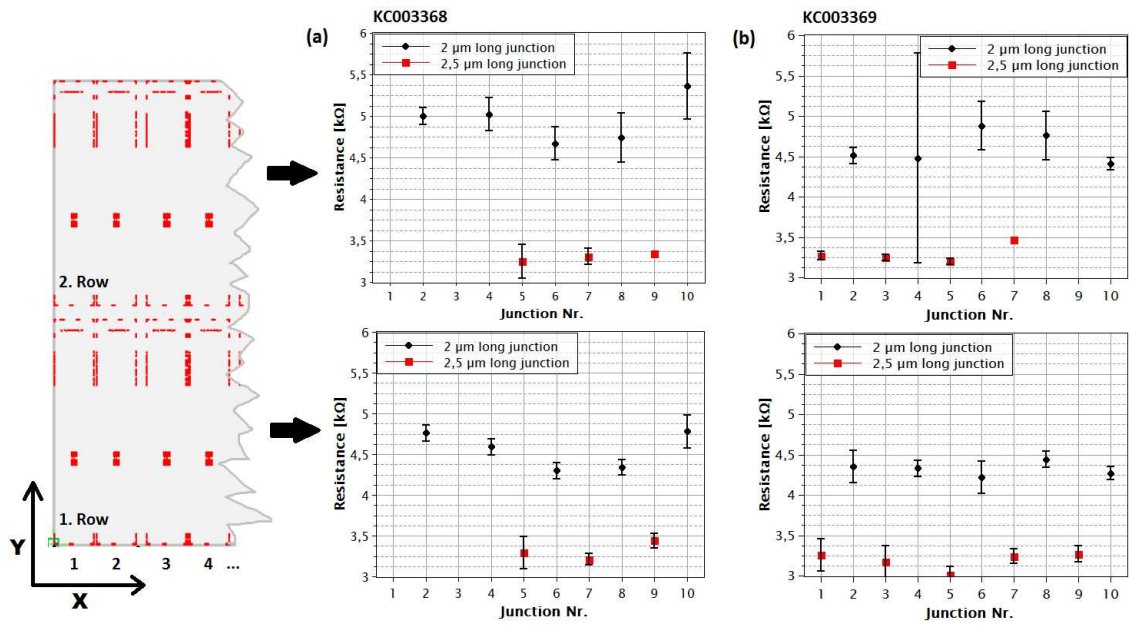


Figure 72: Averaged resistances, from each chip, of the dicing mark junctions on the wafer KC003368 in (a) and KC003369 in (b). They are split up in the resistances of the first row and the resistances in the second row to represent the change over the wafer as well in x-direction as in y-direction.



"The opposite of a correct assertion  
is a false assertion. But the opposite of a  
deep truth can again be a deep truth."

*Niels Bohr*

## 11 Microwave transmission measurement

In this chapter the set up of the microwave measurements and the measurement results are presented. It starts with the final set up of the waveguide, followed by a short explanation how the measurements on the qubits were done in the fridge and what we can learn from the shape of the qubit dips. The resonance frequencies of the qubits are connected to the normal state resistances and while searching for the qubit transition  $|1\rangle \rightarrow |2\rangle$  the so called *Autler-Townes effect* was observed. We also calculated a value for the band gap of the used aluminium from the measurement results.

### 11.1 Waveguide set up

For detailed information about the dimensions and characteristics of the waveguide I refer to [17]. The system to mount the sapphire chips with the qubits in the waveguide is shown in fig.73 (b). The *clamps*, labelled on fig.73 (a), to insert the qubit chips in the wafer are new. They are made out of copper and are connected with copper wires to the so called *T-beam* for extra thermalization. In fig.73 (c) a sideview through the waveguide with two qubit chips inside is shown. For the second cooldown, in addition to the waveguide, a cavity was mounted on the T-beam for another experiment (see fig.73 (d)). After everything is fixed, the T-beam can be mounted into the fridge as shown in fig.73 (e). What we can also find on picture 73 (a), are the so called *couplers* on each side of the waveguide. They couple microwave signals from the coax cables into the waveguide. In our case we use homemade couplers and therefore have to perform an *impedance matching* with the empty waveguide at room temperature.

#### 11.1.1 Impedance matching

Impedance is the opposition by a system to the flow of energy from a source. [29] Upon every change of impedance, reflections occur and power gets effectively lost.[17] To achieve maximum power transfer, all the impedances in a system have to match each other. [30] Couplers are impedance transformers. They transform one impedance to another so that no power is reflected. Therefore we have to tune the couplers to match the impedances of the coax cable with that of the waveguide and achieve the best signal transfer.

The tuning is done by screwing four screws, marked with the blue arrows in fig.74, in and out while sending a microwave through the waveguide and measuring the reflected signal. The goal is to minimize signal reflection. In fig.75 the signal for the final setting of the screws is plotted. The red line marks the reflected signal of -20 dB. Only 1% of the power is reflected there. It is therefore the goal for a good match. As the qubits should have a resonance frequency of about 8 GHz, we optimized the tuning around this frequency. The cutoff frequency of the waveguide is visible at about 6,6 – 6,7 GHz.

After the impedance matching the qubits can be mounted in the waveguide. In fig.76 a sketch of the waveguide and its possible slots to insert a qubit chip is shown. For the first of the two cooldowns we put four single qubits and one junction array resonator in the waveguide. The slots used for the single qubits are marked in orange. The one for the array is marked in green. For the second cooldown we put five qubits inside. Four at the same position as the first time and the fifth in slot number 1. The resistance values of the used qubits and their location in the waveguide are summarized in tab.17.

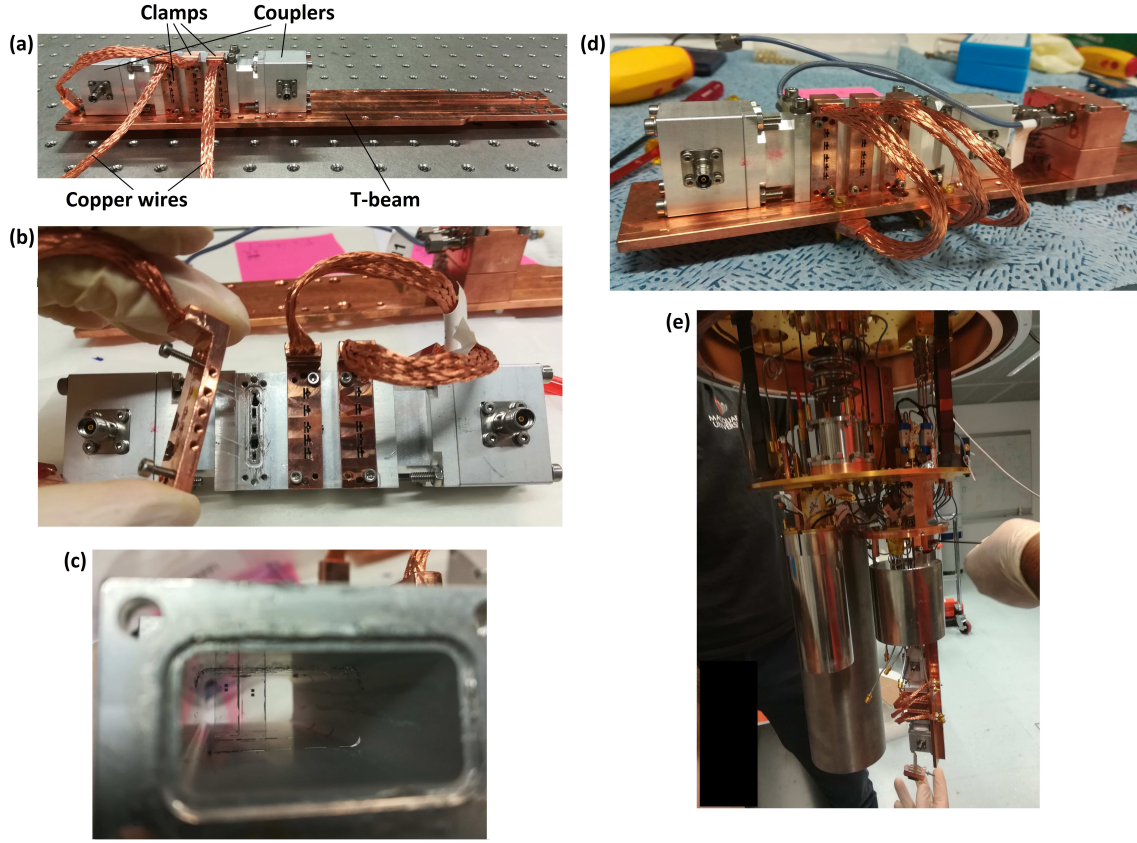


Figure 73: (a) The parts around the waveguide are labelled. (b) The system to insert and mount the qubits in the waveguide. (c) Sideview through the waveguide without the couplers, but with two qubit chips inside. (d) All the parts mounted on the T-beam, ready to go into the fridge. The waveguide with the mounted qubits on the left and a cavity with an additional experiment on the right. (e) Bottom part of the fridge where the T-beam is mounted in one of the cans.

Table 17: Resistance values of the qubits used in the first and the second cooldown. The slot numbers correspond to the numbers in fig.76.

1 <sup>st</sup> cooldown	KC003368				
Slot nr.	5	10	2	7	
$R_n$ [k $\Omega$ ]	6,63	6,31	6,02	4,33	
2 <sup>nd</sup> cooldown	KC003369				
Slot nr.	5	10	2	1	7
$R_n$ [k $\Omega$ ]	4,28	5,91	4,66	4,63	4,13

## 11.2 Performing measurements

Measurements can be performed either in transmittance  $S_{12}$ , where you send in a signal from one end of the waveguide and measure at the other side, or in reflection  $S_{11}$ , where the signal sent in on one side is reflected back and measured at the input port.

If we put a qubit inside the waveguide, the waveguide is effectively shunted by the impedance of the qubit. Most of the signal is just reflected and power gets lost. The measured resonance can be modelled as

$$S_{21} = 1 - \frac{\kappa}{\kappa + 2i(\omega - \omega_0)}$$

with the complex energy decay rate  $\kappa$ , the frequency  $\omega$  and the resonance frequency of the qubit  $\omega_0$ . [31]

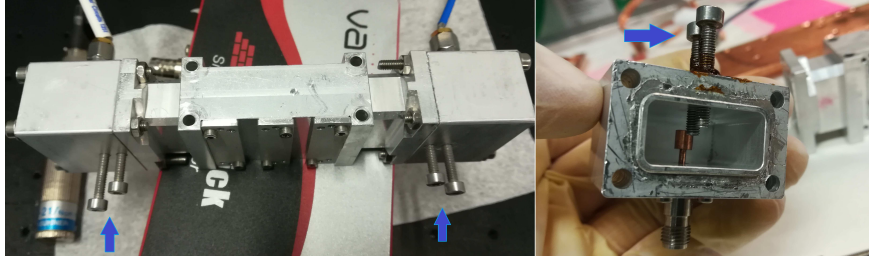


Figure 74: With the blue arrows the screws for the impedance matching are marked. On the left the couplers are already mounted to the waveguide. On the right a view into a coupler is shown. One can see the pin to send in the microwaves and the screws to tune the coupling to the waveguide.

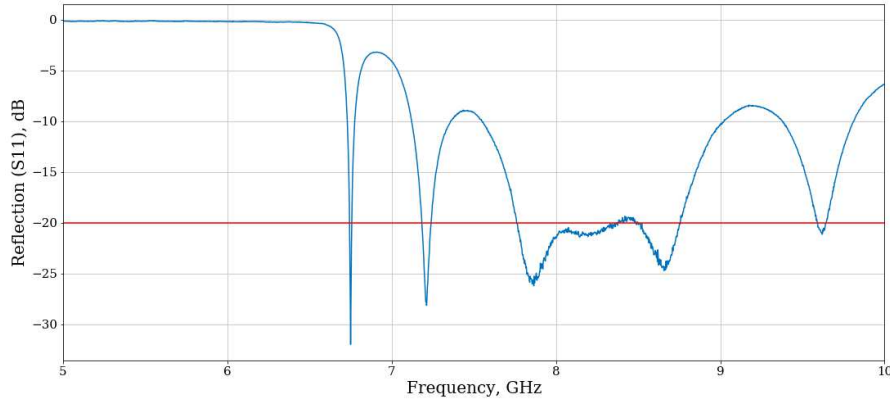


Figure 75: Reflection signal of the impedance matching at room temperature. The red line marks the reflected signal of -20 dB, which is the goal for a good match of the impedances.

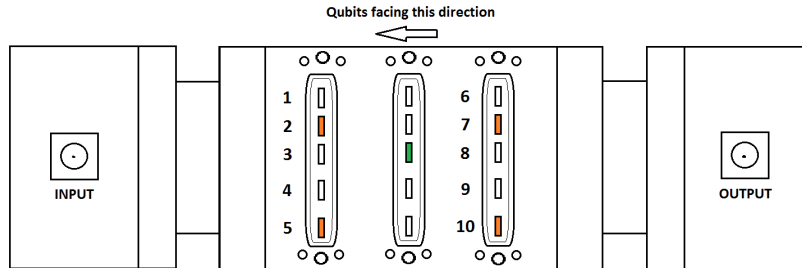


Figure 76: Scheme of the waveguide without the clamps shown from the side with the slots for the qubit chips. In orange the slots used for the first cooldown are marked. For the second cooldown, in addition to the slots 2, 5, 7 and 10, the slot nr. 1 is used for a fifth qubit.

The loss of energy in the system is described by the so called *quality factors*  $Q$ . In general a quality factor gives the losses per cycle compared to the stored energy. [17]

In the first picture of fig.77 the resonance dip of the qubit at 7,218 GHz is shown with the blue line. The red dashed line is a fit to the data. In the second picture the phase of the signal is plotted. One can see a phase shift at the frequency of the resonance. In the bottom two pictures the real and imaginary part of the data is plotted. Fitting this circle with a so called *circle fit* [17] allows us to extract the values for the different quality factors  $Q_l$ ,  $Q_c$  and  $Q_{int}$ .  $Q_l$  is the total quality factor of a resonance and is given by

$$\frac{1}{Q_l} = \frac{1}{Q_c} + \frac{1}{Q_{int}}.$$

$Q_c$  is the quality factor describing the external losses, i.e. the coupling to the waveguide. The internal losses are given by  $Q_{int}$ . This could be dielectric losses, conductive losses or losses due to a contact resistance at the seams of a cavity or waveguide. We are using the circle fit to get an estimate what the quality factors of our qubits are. The ratio of  $Q_{int}$  and  $Q_c$  tells us how deep the resonance dip is. The deeper the resonance the better the coupling of the qubit to the waveguide. More about the circle fit and the quality factors can be found for example in [17].

The measurements in this thesis are all done in transmission. Performed as *single power mea-*

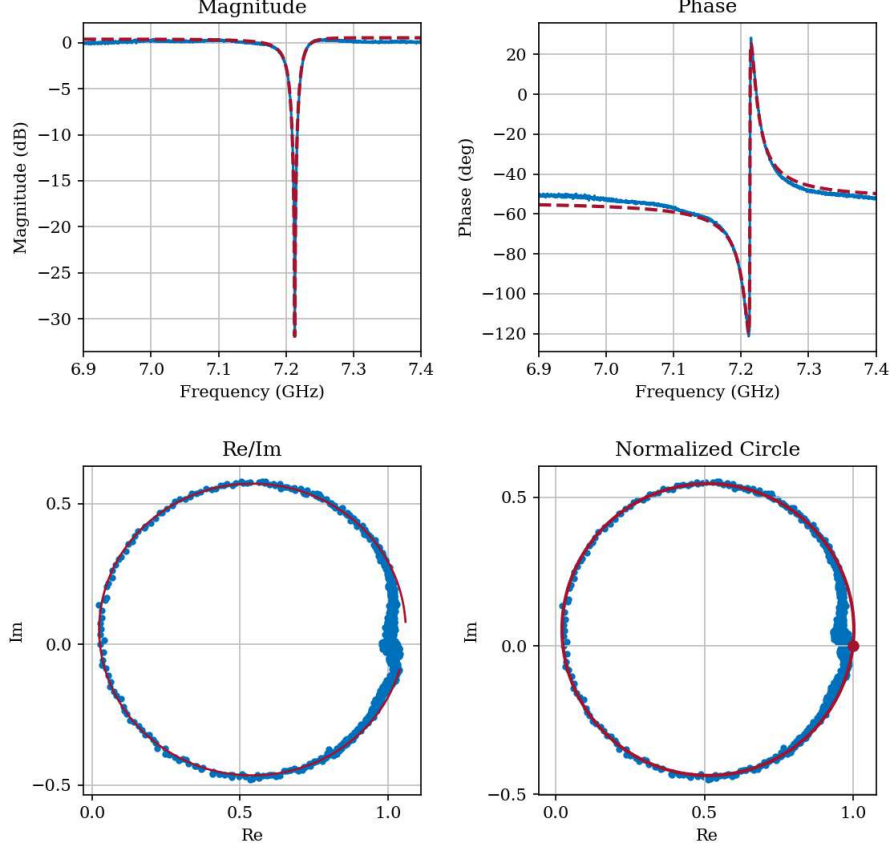


Figure 77: Circle fit of the resonance dip at 7.218 GHz. For the quality factors we get  $Q_L = 308 \pm 1$ ,  $Q_C = 316 \pm 1$  and  $Q_{int} = 13095 \pm 487$ .

*surements* at different frequencies, *powersweeps* at different frequencies, or *two tone* measurements done with an additional *drive power*. With the drive power applied at the resonance frequency of the qubit we can saturate the first qubit transition  $|0\rangle \rightarrow |1\rangle$  and we can find the resonance frequency of the second transition  $f_{12}$ . A summary of the different possibilities to get information out of the system is given in tab.18 For a fixed probe power and a varying drive power we saw a splitting of the second qubit transition. This shift of the energy levels is known as the AC Stark shift or the Autler-Townes splitting.

## 11.3 Results

### 11.3.1 Characterizing the qubits

A first measurement to get an overview of the resonances that are in the waveguide is a scan over a wide range of frequencies with a fixed power. The power has to be high enough to excite a transition, but low enough to not saturate it and drive higher lying energy levels. The waveguide scan from the first cooldown is plotted in fig.78. A power of  $-75$  dBm at the fridge input was used over a frequency range from 5 GHz to 11 GHz. The resonance frequencies of the single qubits at 6,224 GHz and 7,218 GHz are marked with the red arrows. The purple arrow marks the resonance

Table 18: Summary of the measurements that are done within this thesis and how they are named. In general it is about how many microwave signals are applied and what their parameters are.

Measurement	Microwave with...	changed	fixed	What we can find...
<i>Single power</i>	Frequ. $\omega$	✓		Frequ. of 1 <sup>st</sup> qubit transition
	Power $p$		✓	
<i>Powersweep</i>	Frequ. $\omega$	✓		"Colormap" or "3D-plot", higher lying transitions
	Power $p$	✓		
<i>Two tone</i>	$\omega_{probe}$	✓		Frequ. of 2 <sup>nd</sup> qubit transition, (Autler Townes splitting)
	$p_{probe}$ ("weak")		✓	
	$\omega_{drive}$		✓	
	$p_{drive}$ ("strong")	(✓)	✓	

frequency of Phanis junction array at 6,407 GHz. Remember that the cutoff frequency of the waveguide is around 6,6 GHz. The two resonances marked on the left of the cutoff frequency are therefore just weakly coupled to the waveguide. Additionally two single qubits and a second resonance of Phanis array are even further below the cutoff and are not visible in this plot. With a finer scan to reduce the noise we can find these qubits at 6,068 GHz and 5,926 GHz and the junction array at 5,895 GHz.

To find the transition frequency to the second excited state of the qubits we saturate the first

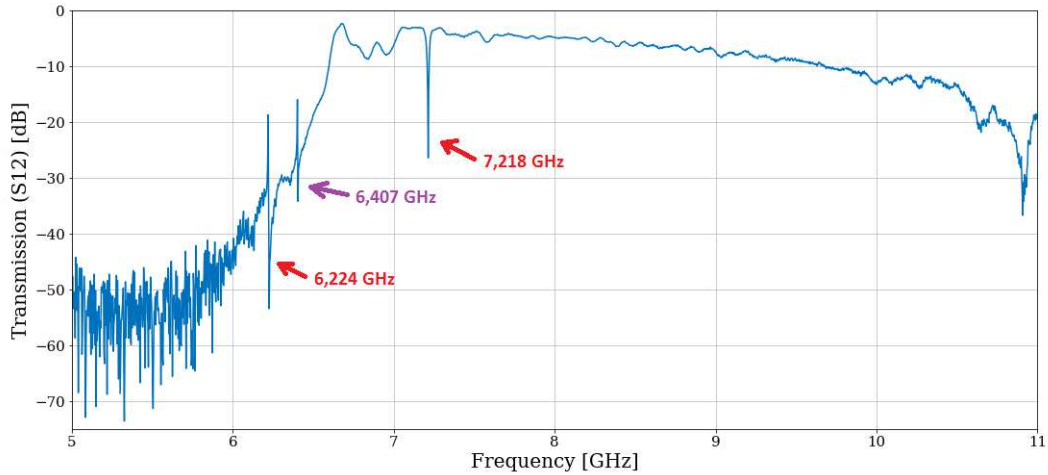


Figure 78: Transmission measurement through the waveguide for the first cooldown with a power of  $-75$  dBm over a range from 5 GHz to 11 GHz. There should be four qubits and resonances from a junction array visible. The resonances marked with red are the single qubits. The resonance marked with purple is one of the resonances of the junction array. The other resonances of the remaining qubits are even further below the cutoff frequency and not visible in this plot due to noise.

transition and sweep through the frequencies nearby. According to theory (see sec.7.2) we should expect a resonance frequency of about 6 GHz for the measured normal state resistance of about  $6 k\Omega$  and an anharmonicity of  $E_C \approx 200$  MHz. We can therefore restrict our scan to a frequency range starting from " $\sim f_{01}$ " to " $\sim f_{01} - 300$  MHz".

In tab.19 the resonance frequencies of the first and the second transition of each single qubit and the corresponding normal state resistances measured before the cooldown are summarized. In addition the values of some calculated parameters are given. The colours indicate the different distances to the waveguide wall and therefore the different capacitances of the qubits.

The same measurements to find the resonance frequencies of the qubits are done during the second cooldown. The waveguide scan from the second cooldown is shown in fig.79. This time only one of the five qubits is below the cutoff of the waveguide, at 6,258 GHz. The others can be found at 6,923 GHz, 6,967 GHz, 7,227 GHz and 7,370 GHz. These frequencies together with the second

Table 19: Parameter of the qubits measured during the first cooldown. The lines marked in gray are the parameters measured directly. The others are calculated from those. The location of the qubits can be compared to the slots marked in fig.76. The colours indicate the different distances to the waveguide wall and the therefore different capacitances of the qubits. In the last row the  $L_J$ s are estimated from the resistances with our value for the band gap of the evaporated aluminium from the fit in fig.81. The resistances are labelled  $R'_n$  because they are corrected by the fit parameter  $b = -0,03 \frac{1}{k\Omega}$ .

Qubit in slot...			Nr. 7	Nr. 2	Nr. 10	Nr. 5
$A_J$	[200 nm x ... $\mu$ m]	design	2,5	2	2	2
$f_{01}$	[GHz]		7,218	6,224	6,068	5,926
$f_{12}$	[GHz]		7,000	5,964	5,811	5,669
$\alpha$	[MHz]	$f_{01} - f_{12}$	218	260	257	257
$E_C$	[J. $10^{-25}$ ]		1,44	1,72	1,70	1,70
$C_\Sigma$	[fF]	$\frac{Q^2}{2 \cdot E_C}$	88,84	74,49	75,35	75,35
$E_J$	[GHz]	$\frac{f_c^2 \cdot h^2}{8 \cdot E_C}$	31,7	20,2	19,5	18,6
$I_C$	[nA]	$\frac{2\pi}{\phi_0} E_J$	63,83	40,69	39,18	37,44
$L_J$	[nH]	$\left(\frac{\Phi_0}{2\pi}\right)^2 \frac{1}{E_J}$	5,16	8,09	8,40	8,79
$R_n$	[k $\Omega$ ]		4,33	6,02	6,31	6,63
$L_J^{R_n}$	[nH] (see equ.19)	$R_n/0,847$	5,11	7,11	7,45	7,83
$L_J^{R'_n}$	[nH] (with our $\Delta$ )	$R'_n/0,938$	5,31	7,84	8,23	8,83

transition frequencies, the measured normal state resistances and the calculated parameters are summarized in tab.20. A discussion of the calculated values is given in the following section 11.3.2.

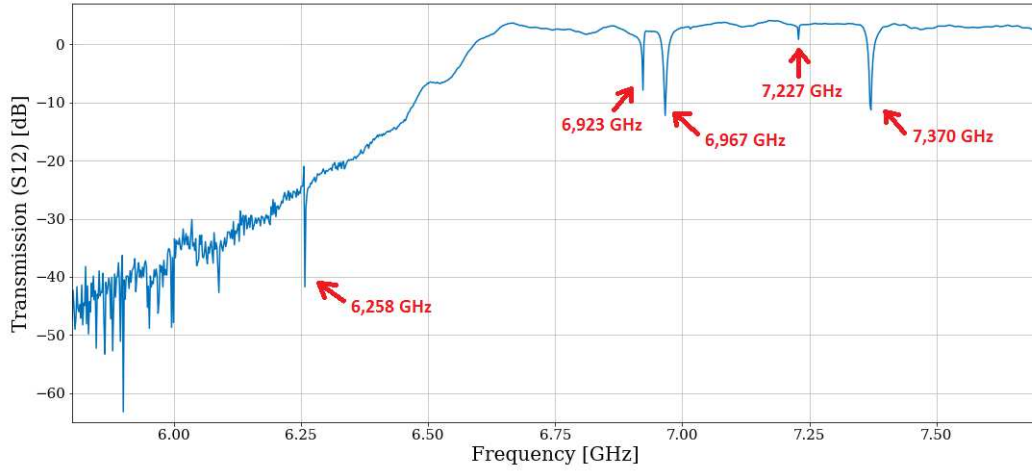


Figure 79: Transmission measurement through the waveguide for the second cooldown over a range from 5,75 GHz to 7,75 GHz. Four qubits above the cutoff of the waveguide and one below the cutoff are visible.

Table 20: Parameters of the qubits measured during the second cooldown. The lines marked in gray are the parameters measured directly. The others are calculated from those. The location of the qubits can be compared to the slots marked in fig.76. This time also slot nr. 1 is used. The colours indicate the different distances to the waveguide wall and the therefore different capacitances of the qubits. In the last row the  $L_J$ s are estimated from the resistances with our value for the band gap of the evaporated aluminium from the fit in fig.81. The resistances are labelled  $R'_n$  because they are corrected by the fit parameter  $b = -0,03 \frac{1}{k\Omega}$ .

Qubit in slot...			Nr. 7	Nr. 5	Nr. 1	Nr. 2	Nr. 10
$A_J$	[200 nm x ... $\mu$ m]	design	2,5	2,5	2,5	2,5	2
$f_{01}$	[GHz]		7,370	7,229	6,967	6,923	6,258
$f_{12}$	[GHz]		7,143	7,002	6,737	6,694	6,004
$\alpha$	[MHz]	$f_{01} - f_{12}$	227	227	230	229	254
$E_C$	[J. $10^{-25}$ ]		1,5	1,5	1,52	1,52	1,68
$C_\Sigma$	[fF]	$\frac{Q^2}{2 \cdot E_C}$	85,31	85,31	84,2	84,57	76,24
$E_J$	[GHz]	$\frac{f_r^2 \cdot h^2}{8 \cdot E_C}$	31,8	30,6	28,2	27,9	20,8
$I_C$	[nA]	$\frac{2\pi}{\phi_0} E_J$	63,99	61,63	56,68	56,21	42,02
$L_J$	[nH]	$\left(\frac{\Phi_0}{2\pi}\right)^2 \frac{1}{E_J}$	5,14	5,34	5,81	5,85	7,83
$R_n$	[k $\Omega$ ]		4,13	4,28	4,63	4,66	5,91
$L_J^{R_n}$	[nH] (see equ.19)	$R_n/0,847$	4,88	5,05	5,47	5,5	6,98
$L_J^{R'_n}$	[nH] (with our $\Delta$ )	$R'_n/0,938$	5,03	5,24	5,73	5,78	7,65

### 11.3.2 Comparison of measurement and theory

Some of the calculated parameters in tab.20 and tab.19 need a short discussion.

**Junction area  $A_J$ :** The first value in the tables is the designed junction area. Depending on the thickness of the polymer layers and the angle under which the aluminium is evaporated, the real junction area can differ from the designed one. Later on we recognized, that the results from the length measurements with the e-beam software were a factor 1,25 smaller than the real lengths. At some point the measuring tool was calibrated wrong. The lengths measured in this thesis therefore have to be multiplied with a factor 1,25 to get the real lengths.

$$\text{real length} = \text{measured length} \times 1,25$$

In our case for the polymer layer thicknesses of about 520 nm and 200 nm and an evaporation angle of 30°, the measured real junction area is about  $780 \pm 30$  nm shorter than the designed junction area. Multiplied with the factor 1,25 leads to a length of  $975 \pm 38$  nm that is missing for the junction area.

**Anharmonicity  $\alpha = E_C$ :** The next value is the anharmonicity  $\alpha$ . It is per definition the difference between the transition frequencies  $\omega_{12}$  and  $\omega_{01}$  of the qubit. For the anharmonic qubit potential it is the same as the charging energy  $E_C$  of the qubit (see sec.4.2).

**Capacitance  $C_\Sigma$ :** The capacitance  $C_\Sigma$  in the tables is calculated as  $C_\Sigma = \frac{Q^2}{2E_C}$  with the charge of an electron  $Q$ . Also from the simulation we get a value for the capacitance. There it is calculated from the given inductance  $L_J$  and the resulting resonance frequency  $\omega_r$  as  $C_{sim} = \frac{1}{L_J \omega_r^2}$ . As discussed in sec.5.2.2 the difference between those values is the junction capacitance. In the simulation we didn't consider the capacitance of the junction whereas in the real measurements all possible capacitances contribute. Calculating this difference should therefore give us the capacitance from the junction area. It turns out that this is not that trivial as it sounds. In fig.80 the capacitances to the resonance frequencies of the qubits from the simulation are plotted against the inductance. For each distance to the wall one would expect a constant line. The capacitance of the



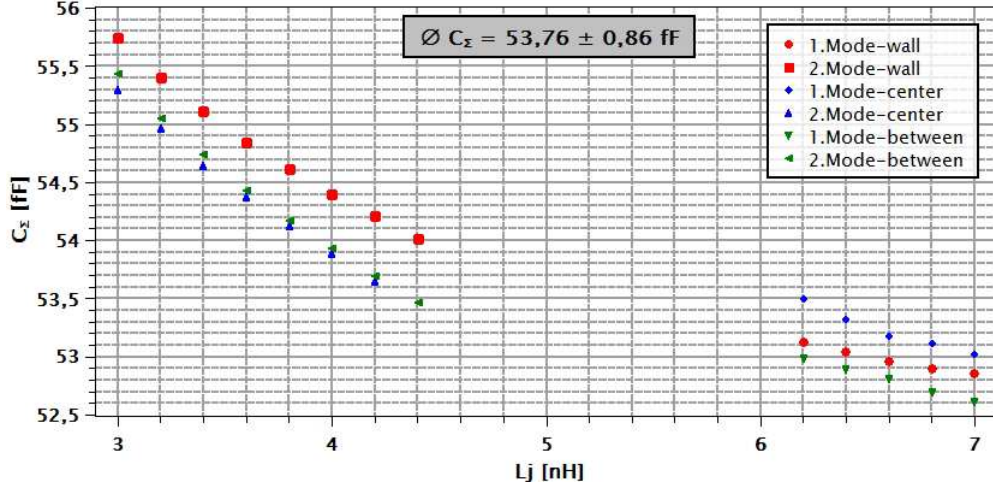


Figure 80: Capacitance of the system calculated from the simulation data. The data points at or near the avoided crossing are excluded.

system in the waveguide theoretically doesn't change. Obviously this is not the case. The influence of the "artificial" cavity modes that we have in the simulation makes it impossible to say which one is the "real" capacitance or even which one is the closest to the "real" value. We calculated the average of all those capacitances and put the difference in the standard deviation. The value for the capacitance we got from the simulation is  $53,8 \pm 0,9$  fF. Also for the capacitances from the measurements we therefore don't care about the position in the waveguide. We just distinguish between the  $2 \mu\text{m}$  and the  $2,5 \mu\text{m}$  long designed junctions. Have in mind that the designed junction length is about  $975 \pm 38$  nm longer than the real junction lengths! For the  $2 \mu\text{m}$  long designed junctions we measured a value of  $75,4 \pm 0,7$  fF ( $6,2 \pm 0,3$  k $\Omega$ ) and for the  $2,5 \mu\text{m}$  long designed junctions a value of  $86 \pm 2$  fF ( $4,4 \pm 0,2$  k $\Omega$ ). In brackets the averaged resistances to the two junction lengths are given. The big error of the capacitance of the  $2,5 \mu\text{m}$  long junctions is due to the qubit in slot Nr.7 from the first cooldown. It had a much higher capacitance compared to the other qubits with the same junctions in the second cool down. Similarly the only  $2 \mu\text{m}$  long junction in the second cooldown has a slightly higher capacitance than the same junction lengths in the first cooldown. Nevertheless, if we take these values and subtract the simulated capacitance we get the values summarized in tab.21 for the junction capacitances.

Table 21: Junction capacitances for the designed  $2 \mu\text{m}$  and  $2,5 \mu\text{m}$  long junctions. The real lengths are about  $975 \pm 38$  nm smaller due to the evaporation angle and an error in the e-beam measurement.

Junction length	$C_{\text{junction}}$
$1,03 \pm 0,04 \mu\text{m}$	$22 \pm 2$ fF
$1,53 \pm 0,04 \mu\text{m}$	$32 \pm 3$ fF

**Josephson energy  $E_J$ :** The next parameter in the tables is the Josephson energy  $E_J$  calculated from the charging energy  $E_C$  and the resonance frequencies of the qubit  $f_r = f_{01} + \alpha$  as  $E_J = \frac{f_r^2 \cdot h^2}{8 \cdot E_C}$ . This is again straight forward but very useful as it is connected to the critical current  $E_J = I_C \frac{\Phi_0}{2\pi}$ . If we know the critical current we can plot it against the measured normal state resistances and get a value for the product  $\Delta \cdot 0,87$  in the Ambegaokar-Baratoff formula  $I_C = \frac{\pi \Delta \cdot 0,87}{2e \cdot R_n}$ . In fig.81 this was done. From a fit through the data points with the fit function  $a * (x + b)$  we find that  $a = \frac{\pi}{2e} \cdot \Delta \cdot 0,87 = 308,9 \pm 11,5$  nA·k $\Omega$  and get for the product of the band gap times the constant  $0,87$  a value of  $\Delta \cdot 0,87 = 1,966 \pm 0,073 \cdot 10^{-4}$  eV. If we trust the constant value of  $0,87$  and assume



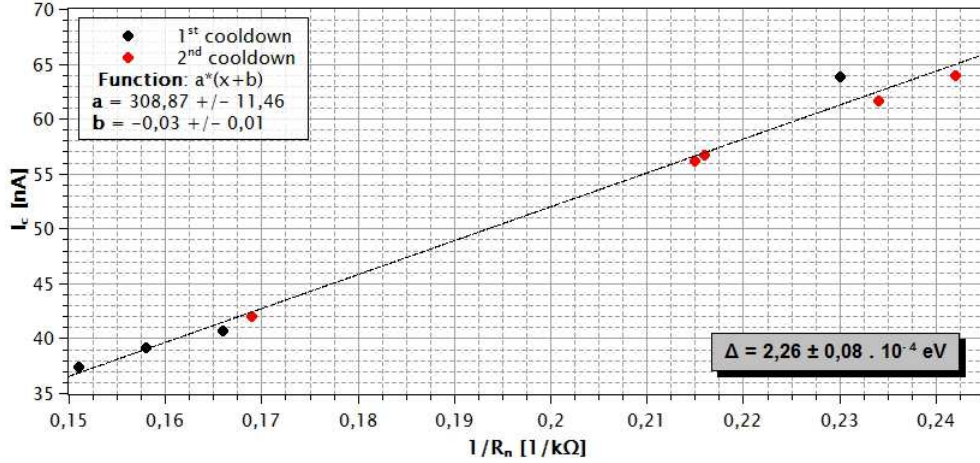


Figure 81: Calculated critical current plotted against the measured normal state resistance. From a fit through the data points we can, according to Ambegaokar-Baratoff, extract a value for the band gap of the used aluminium. For the qubits from the two cooldowns done during this master thesis we get a band gap of  $\Delta = 2,26 \pm 0,08 \cdot 10^{-4}$  eV.

that it is correct, the band gap for the aluminium we are using is about

$$\Delta = 2,26 \pm 0,08 \cdot 10^{-4} \text{ eV}$$

To compare this value, the group of Ioan Pop at KIT measured a value of  $\Delta = 2,04 \cdot 10^{-4}$  eV.

**Inductance  $L_J$ :** The last parameter we calculated in the tables is the inductance of the qubit  $L_J$ . There are three values given. One time the inductance is calculated from the Josephson energy, one time it is estimated from the normal state resistance according to equ.19 from sec.7 and the last value calculates with the same estimation but with the value for the band gap we calculated for the used aluminium. With this customized band gap we get the relation

$$R_n[k\Omega] = 0,94 \pm 0,03[1/s] \cdot L_J[nH]$$

Comparing the two estimations for the inductances in the tables 20 and 19 to the values calculated from the Josephson energy, we see, that the correction for the band gap improves the estimation. The inductance values resulting from the calculation with our band gap are closer to that calculated from the Josephson energy than the estimation made with the band gap value from KIT.

### 11.3.3 Autler-Townes splitting

Due to the similar normal state resistances of the qubits, their measured resonances are close to each other. In this case it can be difficult to find the right resonance line in the Powersweep plots that corresponds to the second transition. Therefore we tried to find the  $|1\rangle \rightarrow |2\rangle$  transitions by varying the drive power that saturates the qubit transition  $|0\rangle \rightarrow |1\rangle$ . We would expect to see one resonance line (the first qubit transition) disappearing, while simultaneously a new resonance (the second qubit transition) appears. In fig.82 our observations are plotted in the example of the qubit at 6,224 GHz. We unintentionally managed to induce the so called *Autler-Townes splitting* [34].

Let's see how this could happen. In our set up we have the situation of an artificial atom, the Transmon, with its eigenstates  $|g\rangle$ ,  $|e\rangle$ , etc., embedded in a waveguide with the eigenstates  $|n\rangle$ , where  $n$  is the number of microwave photons (see the left hand side of fig.83 (a)). The uncoupled states of the combined system 'qubits + waveguide' are described by the so called *bare states*  $|g, n\rangle$ ,  $|e, n\rangle$ ,  $|g, n+1\rangle$ ,  $|e, n+1\rangle$ , etc. (shown on the right hand side of fig.83 (a)).

Depending on the detuning  $\Delta = \omega_d - \omega_q$  between the resonance frequency of the qubit  $\omega_q$  and that of the external field  $\omega_d$ , the levels  $|e, n\rangle$  and  $|g, n+1\rangle$  are either degenerated ( $\Delta = 0$ ) or separated by the detuning  $\Delta$ . In fig.83 (a) they are not degenerated.

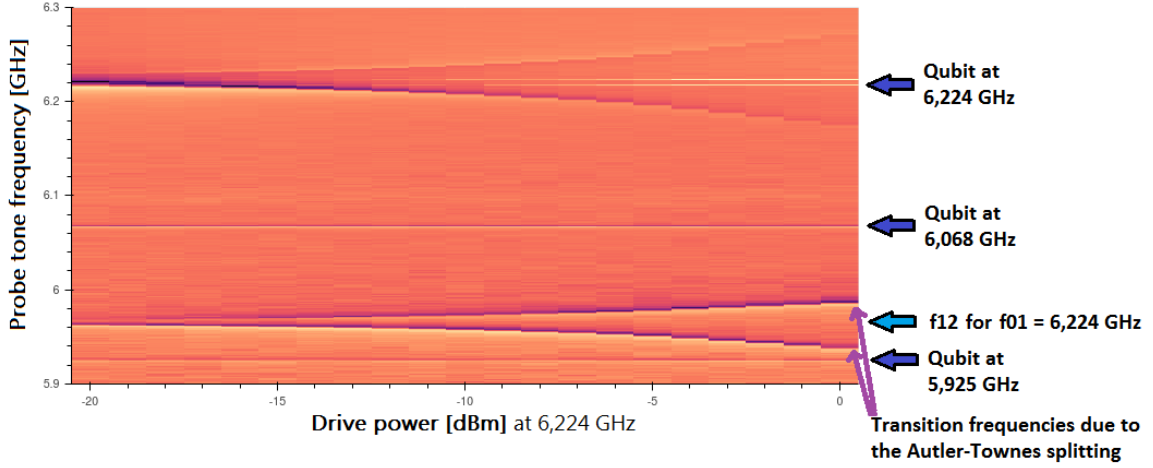


Figure 82: Two tone measurement with a probe power of  $-60$  dBm scanned from  $5.9$  GHz to  $6.3$  GHz for each drive power. The drive power is scanned from  $-20$  dBm to  $-0$  dBm at a fixed frequency of  $6,224$  GHz. With increasing drive power on the first qubit transition at  $6,224$  GHz we can see, that the second qubit transition at  $5,964$  GHz splits up. We can observe the so called *Autler Townes splitting*. In addition we can see the resonance dips of the qubits at  $6,068$  GHz and at  $5,926$  GHz which do not split as they are not driven.

By sending the microwave tone with frequency  $\omega_d$  in the waveguide a coupling between the bare states is turned on. Due to the coupling the two uncoupled states  $|g, n+1\rangle$  and  $|e, n\rangle$  repel each other and are transformed into perturbed states, the so called *dressed states*

$$|+, n\rangle = |e, n\rangle + |g, n+1\rangle$$

$$|-, n\rangle = |e, n\rangle - |g, n+1\rangle$$

(see the right hand side of fig.83 (a)). The absolute energy shift of the dressed states depends on the detuning  $\Delta$ . The biggest absolute energy shift can be found on resonance  $\omega_q = \omega_d$ . There the splitting of the first doublet of dressed states is  $\hbar\Omega$ .  $\Omega$  can be considered as the Rabi frequency of the field associated with a single photon in the waveguide. [34]

The smooth transition from  $-\Delta$  to  $\Delta = 0$  to  $+\Delta$  is sketched in fig.83 (b). It shows the splitting of the dressed states at and near the degeneracy point  $\omega_d = \omega_q$ , where the bare states (indicated with the violet dashed lines) would cross each other. In the regions where  $\Delta \gg \Omega$  the distance between the dressed state to its corresponding asymptote indicates the ac Stark shift of the level  $|g\rangle$  or  $|e\rangle$  due to the coupling to the nonresonant field  $\omega_d$ . [34]

The splitting of the second qubit transition  $\omega_f = f_{12}$  in fig.82 therefore originates from the first dressed state doublet due to the Autler-Townes splitting. Those transitions are indicated with the blue arrows in fig.83 (b) and on the right hand side in (a).

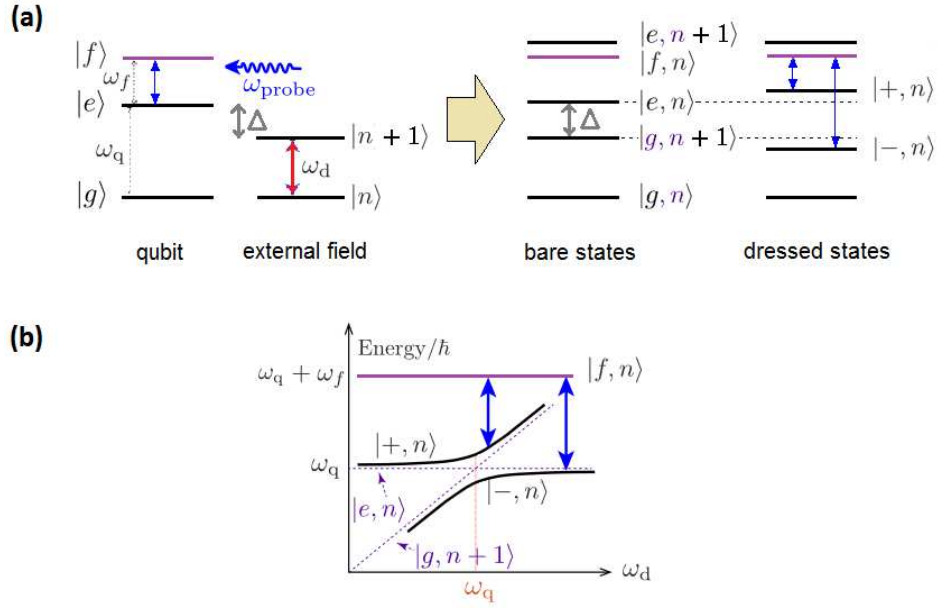


Figure 83: (a) On the very left the first three qubit states and the first two states of a quantized external field are shown. The frequency of the external field and the first qubit transition are detuned by  $\Delta = \omega_d - \omega_q$ . The combined system 'qubit + external field' can be described by the so called *bare states*. If we take the coupling between the states into account, the energy levels are perturbed and it leads to the so called *dressed states*. They are shown on the very right. (b) The energy spectrum of the dressed states depending on the frequency of the drive tone  $\omega_d$ . If the drive tone comes close to resonance with the first qubit transition  $\omega_q$  the energy levels begin to split apart in a so called avoided crossing. The distance between the dressed states (black lines) and the bare states (dashed violet lines) indicates the shift depending on the detuning  $\Delta$ . On resonance  $\omega_q = \omega_d$  the levels shift the most and the splitting is exactly given by the Rabi frequency  $\Omega$ .

"A conclusion is simply the place  
where you got tired of thinking."  
*Dan Chaon*

## 12 Conclusion and Outlook

Let's summarize the main results we found within this master thesis. Fabrication wise the work during this master thesis was a first big step for a long optimization journey that now has to be investigated further. The whole story of our fabrication progress presented in chapter 10 shows, that fabrication is more than just following a recipe. Starting with a brand new clean room with machines nobody worked with before and a recipe from another group to do the qubit fabrication, leads us to months of trial and error before we got to know the right parameters and got working qubits. Some takeaways we learned in this time are, that we still should take care of remaining dust and dirt despite the already clean environment in the clean room. Even if it is not visible at first, enlarged under the microscope we can see a big improvement in the roughness of the qubit surfaces when we take care that really nothing unwanted can settle down on the wafer.

Another point is, that for every new design a dose test should be done before writing the final structures. Small additional or missing parts in the design could lead to additional or missing doses at some features. With the dose test we can directly evaluate and eliminate errors that occur due to the proximity effect.

A first estimation, if the fabricated qubits are working, can be done by measuring the normal state resistance through the junction. From this value we can calculate back, if the qubit provide the expected resonance frequency for the experiment. What we found is, that one has to be a bit careful trusting the resistance values. Even if we measure suitable resistance values it doesn't tell us something about how the qubit, or the junction look like. The resistance measurement is therefore a quick verification of the right resistances just for fabrication procedures that are already investigated and known as procedures that produce good looking qubits.

From the qubits studied in this thesis we found a junction capacitance  $C_{junction}$  of  $22 \pm 2$  fF for a "real" junction size of  $1,03 \pm 0,04 \mu\text{m} \times 200$  nm and a junction capacitance of  $32 \pm 3$  fF for the "real" junction size of  $1,53 \pm 0,04 \mu\text{m} \times 200$  nm. With this values for the junction capacitance we can correct the capacitance resulting from a simulation  $C_{sim}$  to the capacitance of the whole system  $C_{\Sigma}$ .

From the Ambegaokar-Baratoff formula (equ. 17) we calculated for the aluminium we were using a bandgap of  $\Delta = 2,26 \pm 0,08 \cdot 10^{-4}$  eV.

With this value for the bandgap we found the connection between the normal state resistance and the inductance  $R_n[k\Omega] = 0,94 \pm 0,03[1/s] \cdot L_J[nH]$  to quickly estimate the normal state resistance one wants to get after fabrication. Together with the capacitance of the whole system  $C_{\Sigma}$  we can than predict the first transition frequency of the qubit  $\omega_{01} = \frac{1}{\sqrt{LC_{\Sigma}}} - \frac{e^2}{2C_{\Sigma}}$  before cooling down the qubit.

The general conclusion from all the measurements is, that our transmon qubits are working quite well, in the sense that the calculations, done with the measured parameters, fit the theory. They can be characterized as qubits with an aluminium band gap that is a bit bigger than in other groups (see KIT) and a quite high junction capacitance. If we look at the resistance values, we see that there is still potential in the fabrication. Originally the goal was to fabricate two different qubit sizes to get two different resistance values. In reality we saw resistances with a difference up to  $0,5 k\Omega$ . The qubits are therefore only reproducible to a limited extend. Also the surviving rates of the qubits on a wafer can be improved. In sec.10.7.1 we got a surviving rate bigger than 90% just for the shorter junctions. For the longer junctions we got 33,33% and 59,17%. A rate close to 100% would be desirable. Also the aging about 40%, that we saw at these qubits, is quite a lot.

From my point of view the fabrication process still can be improved and is a large part that can contribute to finally get stable and reproducible qubits that can be used for further experiments up to applications. I hope that the detailed descriptions of the fabrication progress in this thesis can help to understand what can happen and what we see in the different steps of the fabrication and why we maybe see unwanted parts on or near the qubit/junction.

## References

- [1] (2016). "Quantum Manifesto - A New Era of Technology". Quantum Flagship. Link: [https://qt.eu/app/uploads/2018/04/93056\\_Quantum-Manifesto\\_WEB.pdf](https://qt.eu/app/uploads/2018/04/93056_Quantum-Manifesto_WEB.pdf)
- [2] Knoglinger H. (2004). "Herstellung und Charakterisierung von supraleitenden Phasen-Qubits". Diplomarbeit, Technische Universität München. Link: [https://www.wmi.badw.de/publications/theses/Knoglinger\\_Diplomarbeit\\_2004.pdf](https://www.wmi.badw.de/publications/theses/Knoglinger_Diplomarbeit_2004.pdf)
- [3] Sieroka N. (2014). "Philosophie der Physik - Eine Einführung". München: C.H.Beck.
- [4] Feynman R. et al. (2010). "The Feynman Lectures On Physics". Vol. 3: Quantum mechanics, New Millennium ed., New York: BASIC BOOKS.
- [5] Gross R., Marx A. (2014). "Festkörperphysik". 2nd ed., Oldenbourg: De Gruyter
- [6] Gross, R. (2014). Lecturenotes, Superconductivity chapter 5. Walther-Meißner-Institut. "[https://www.wmi.badw.de/teaching/Lecturenotes/SLTTP%20I/SL\\_Chapter%205\\_2014.pdf](https://www.wmi.badw.de/teaching/Lecturenotes/SLTTP%20I/SL_Chapter%205_2014.pdf)" (16.03.2020, 14:18 Uhr).
- [7] Likharev K. (1986). "Dynamics of Josephson junctions and circuits". Department of Physics, Moscow State University. New York: Gordon and Breach Science Publishers.
- [8] Ambegaokar V., Baratoff A. (1963). "Tunneling between Superconductors". Phys. Rev. Lett. Vol. 10, Nr. 11. Link: <https://journals.aps.org/prl/pdf/10.1103/PhysRevLett.10.486>
- [9] K. Gloos et al. (2000). "Wide-range thermometer based on the temperature-dependent conductance of planar tunnel junctions". Appl. Phys. Lett. 77. Link: <https://doi.org/10.1063/1.1320861>
- [10] Bilger F. (2011). "Herstellung und Charakterisierung von Flussquantenbits mit vier Josephson-Kontakten". Diplomarbeit, Technische Universität München. Link: [https://www.wmi.badw.de/publications/theses/Bilger\\_Diplomarbeit\\_2011.pdf](https://www.wmi.badw.de/publications/theses/Bilger_Diplomarbeit_2011.pdf)
- [11] Borghini N. (2017). Kapitel V, Hamilton-Formalismus. Universität Bielefeld. "[https://www.physik.uni-bielefeld.de/~borghini/Teaching/Theorie-I/12\\_06.pdf](https://www.physik.uni-bielefeld.de/~borghini/Teaching/Theorie-I/12_06.pdf)" (24.11.2019, 14:35 Uhr).
- [12] Schuster I. (2007). "Circuit Quantum Electrodynamics". Dissertation, Yale University. Link: [https://rsl.yale.edu/sites/default/files/files/RSL\\_Theses/SchusterThesis.pdf](https://rsl.yale.edu/sites/default/files/files/RSL_Theses/SchusterThesis.pdf)
- [13] Krantz P. et al. (2019). "A Quantum Engineer's Guide to Superconducting Qubits". Cornell University. Link: <https://arxiv.org/pdf/1904.06560.pdf>
- [14] Koch J. et al. (2007). "Charge insensitive qubit design derived from the Cooper pair box". Phys. Rev. A 76. Link: <https://journals.aps.org/pra/pdf/10.1103/PhysRevA.76.042319>
- [15] Blais A. et al. (2020). "Circuit Quantum Electrodynamics". Cornell University. Link: <https://arxiv.org/pdf/2005.12667.pdf>
- [16] Pozar D. (2012). "Microwave Engineering". 4th ed., Wiley.

- [17] Zöpfl D. (2017). "Characterisation of stripline resonators in a waveguide". Master thesis, University of Innsbruck.
- [18] Orell T. et al. (2019). "Waveguide QED with an array of transmons", Nano and Molecular Systems Research Unit, University of Oulu.
- [19] Jensen E. CERN, Geneva, Switzerland. "Cavity basics". Link: <https://arxiv.org/ftp/arxiv/papers/1201/1201.3202.pdf>
- [20] Batey G., Teleberg G. (2015). "Principles of dilution refrigerator. A brief technology guide." Oxford Instruments NanoScience. [http://home.agh.edu.pl/~kozlow/fizyka/otrzymywanie\\_niskich\\_T\\_jakdzialaTriton/Principles-of-dilution-refrigeration\\_v14.pdf](http://home.agh.edu.pl/~kozlow/fizyka/otrzymywanie_niskich_T_jakdzialaTriton/Principles-of-dilution-refrigeration_v14.pdf) (15.09.2020, 20:32 Uhr).
- [21] Barrier J. (2019). "Principles of the dilution refrigerator". <http://julienbarrier.eu/blog/2019/08/14/dilution-fridge.html> (26.10.2020, 17:13 Uhr).
- [22] Yu-Lin W. et al. (2013). "Fabrication of Al/AlO<sub>x</sub>/Al Josephson junctions and superconducting quantum circuits by shadow evaporation and a dynamic oxidation process". Chin. Phys. B, Vol. 22, Nr. 6. Link: <https://iopscience.iop.org/article/10.1088/1674-1056/22/6/060309/pdf>
- [23] Zhang K. et al. (2017). "Bridge-free fabrication process for Al/AlO<sub>x</sub>/Al Josephson junctions". Chin. Phys. B, Vol. 26, Nr. 7.
- [24] Stepanova M., Dew S. (Eds.) (2012). "Fundamentals of Electron Beam Exposure and Development." in "Nanofabrication - Techniques and Principles". 1st ed., Chap. 2, pp.11-41, Wien: Springer.
- [25] "Structural Biochemistry/Lipids/Micelles". Wikibooks, Open books for an open world. [https://en.wikibooks.org/wiki/Structural\\_Biochemistry/Lipids/Micelles](https://en.wikibooks.org/wiki/Structural_Biochemistry/Lipids/Micelles) (27.10.2020, 08:25 Uhr).
- [26] (2015). "NANOSUITE Software Reference Manual". Doc. nr. 4-03-6.9. Raith GmbH.
- [27] Zeng L. et al. (2014). "Direct observation of the thickness distribution of ultra thin AlO<sub>x</sub> barrier in Al/AlO<sub>x</sub>/Al Josephson junctions". Chalmers University of Technology, Gothenburg. Link: <https://arxiv.org/ftp/arxiv/papers/1407/1407.0173.pdf>
- [28] Peterer M. (2016). "Experiments on Multi-Level Superconducting Qubits and Coaxial Circuit QED". Dissertation, University of Oxford. Link: [https://ora.ox.ac.uk/objects/uuid:572f08ef-2d14-4fda-8e18-71f80fc4c47a/download\\_file?file\\_format=application/pdf&safe\\_filename=DPhil\\_Peterer\\_Michael\\_dissemination.pdf&type\\_of\\_work=Thesis](https://ora.ox.ac.uk/objects/uuid:572f08ef-2d14-4fda-8e18-71f80fc4c47a/download_file?file_format=application/pdf&safe_filename=DPhil_Peterer_Michael_dissemination.pdf&type_of_work=Thesis)
- [29] "Impedance matching". Wikipedia, The Free Encyclopedia. [https://en.wikipedia.org/wiki/Impedance\\_matching](https://en.wikipedia.org/wiki/Impedance_matching) (24.08.2020, 15:05 Uhr).
- [30] Frenzel L. (2011). "Back to Basics: Impedance Matching (Part 1)". ElectronicDesign, Endeavor Business Media. <https://www.electronicdesign.com/technologies/communications/article/21796367/back-to-basics-impedance-matching-part-1> (12.07.2020, 17:31 Uhr).

- [31] Reagor M. (2015). "Superconducting Cavities for Circuit Quantum Electrodynamics". Dissertation, Yale University. Link: [https://rsl.yale.edu/sites/default/files/files/RSL\\_Theses/reagor-thesis-20151202.pdf](https://rsl.yale.edu/sites/default/files/files/RSL_Theses/reagor-thesis-20151202.pdf)
- [32] Bardeen J., Cooper L., Schrieffer J. (1957). "Theory of Superconductivity". Phys. Rev. Vol. 108, Nr. 5. Link: <https://journals.aps.org/pr/pdf/10.1103/PhysRev.108.1175>
- [33] Devoret M. (1995). "Quantum Fluctuations in Electrical Circuits". Les Houches, Session LXIII. Elsevier Science. Link: [http://qulab.eng.yale.edu/documents/reprints/Houches\\_fluctuations.pdf](http://qulab.eng.yale.edu/documents/reprints/Houches_fluctuations.pdf)
- [34] Cohen-Tannoudji C. "The Autler-Townes effect revisited". College de France et Laboratoire Kastler Brossel de l'Ecole Normale Supérieure.





## Appendices...



Sample:

Date:

<u>Fabroutine:</u>	<u>Changes:</u>	<u>Notes:</u>
<b>Cleaning:</b> <ul style="list-style-type: none"> <li>- <b>10 min in Aceton</b></li> <li>- Rinse with Aceton, Isoprop, Water</li> <li>- Blow dry</li> </ul>	On: _____	
<b>Spincoat:</b> ----- <ul style="list-style-type: none"> <li>- <u>Copolymer</u> -&gt; (ramp: 1000 rpm/s, speed: 2000 rpm, time: 100 s), put resist with closed lid on the wafer when it is already spinning, bake <b>5 min at 200°C</b></li> <li>- <u>PMMA</u> -&gt; (ramp: 1000 rpm/s, speed: 2000 rpm, time: 100 s), put resist on it before closing the lid till wafer is nearly full with resist, bake <b>10 min at 200°C</b></li> </ul>	On: _____	
<b>Sputter Gold:</b> ----- <ul style="list-style-type: none"> <li>- <u>Table: at the bottom</u></li> <li>- <u>170 s</u></li> <li>- <u>10 mA</u></li> <li>- <u>0,6 mbar</u></li> </ul>	On: _____	
<b>E-beam:</b> ----- <ul style="list-style-type: none"> <li>- Meander mode</li> <li>- Z: 26 mm</li> <li>- 30 kV</li> <li>- 10 mm Working Distance</li> <li>- 120 µm aperture (1000 µm WF, 130x magnification)               <ul style="list-style-type: none"> <li>o Beam current: ~ 5,4 nA</li> <li>o Area Step Size: 0,02 µm</li> <li>o Area Line Spacing: 0,02 µm</li> <li>o Area Dose: 80 µC/cm<sup>2</sup></li> <li>o In positionlist: U,V =&gt; +0.45,+0.45 [mm]</li> </ul> </li> <li>- 10 µm aperture (100 µm WF, 1300x magnification)               <ul style="list-style-type: none"> <li>o Beam current: ~ 35 pA</li> <li>o Area Step Size: 0,002 µm</li> <li>o Area Line Spacing: 0,002 µm</li> <li>o Area Dose: 80 µC/cm<sup>2</sup></li> <li>o In positionlist: U,V =&gt; +0,+0 [mm]</li> </ul> </li> </ul>	On: _____ Design file: _____	
<b>Remove Gold:</b> ----- <ul style="list-style-type: none"> <li>- <u>Lugol:</u> <u>Ration -&gt; 1g I<sub>2</sub> : 4g KI : 40ml H<sub>2</sub>O</u> <u>(mix 2g : 8g : 80ml -&gt; 3h, 80rpm in orbital shaker)</u></li> <li>- <b>80 rpm</b></li> <li>- <b>1 min</b></li> </ul>	Lugol used the ____ time. (mixed on _____, used on _____)	
<b>Develop:</b> ----- <ul style="list-style-type: none"> <li>- In Chiller at 6,7°C</li> <li>- <b>1:45 min</b> in 3 : 1 (IPA : H<sub>2</sub>O)</li> <li>- Stop in water</li> </ul>	Developer used the ____ time. (mixed on _____, used on _____)	
<b>Plassys:</b> ----- <ul style="list-style-type: none"> <li>- Fill cold trap</li> <li>- Pump 3h to ~ 2 x 10<sup>-7</sup> mBar</li> <li>- Descum: 200 V, 10 mA, 5 sccm O<sub>2</sub>, 10 sccm Ar, 1min</li> <li>- Getter: Ti, 0,2 nm/s, 2 min</li> <li>- Evaporation: Al, <b>25 nm +30 nm</b>, <b>+ 30°, 1 nm/s</b></li> <li>- Oxidation: <b>15min, 30mbar</b></li> </ul>	On: _____	
<b>Lift Off:</b> ----- <ul style="list-style-type: none"> <li>- In Aceton for 5 min</li> <li>- <b>Sonicate 1 min, 35 kHz, 20 %</b></li> <li>- Left in Aceton for.....</li> <li>- Sonicate again + rinse</li> </ul>	Time: _____	



## How to do and what to pay attention on in fabrication of qubits

### General rules:

- Wear **mouthguard mask**
- **Avoid doing things over your wafer** (like lean over it to get a pipette for example, or speak without mask over the wafer,...)
- **Only** touch your wafer with a **tweezer on the waferflat!!**
- The **upper side is the one you can't read the wafer number from**
- For every step have in mind that the surface of the wafer should **have as little as possible contact to liquid surfaces** to avoid dirt on your sample!!
- work with liquids and gases **always in the direction to the tweezer** and not from the tweezer to the wafer!

### **Clean the wafer:**

#### What you need:

Each a spray bottle of Aceton, Isopropanol, distilled water  
Small Petri dish  
Nitrogen gun  
Tweezer  
Wafer box

- Put your wafer in a cleaned Petri dish with Aceton for 10 min, the side you want to write on facing upwards, slew from time to time so that the Aceton is moving over the wafer
- When you get the wafer out of the Petri dish, make sure that the surface is still covered with Aceton. Then immediately rinse with Aceton, then with Isopropanol and then with distilled water.
- Blow dry with nitrogen -> always towards the tweezer!
- Put the wafer facing downwards with the side you want to write on (so that you can read the wafer number) in a wafer box (or, when already prepared directly on the spin-coater...)

### **Spin-coating the wafer:**

#### What you need:

Cleanroom towels  
Tweezer  
Pipettes  
Your resist (for ex. PMMA, Copolymer EL)  
Stopwatch  
Hotplate  
Spray bottle with Isopropanol

- **Turn on the hotplate**
- **Load** the full **pipette** with the resist you want to use
- **Select** the **program** you want to use at the spin-coater
  - Copolymer -> ramp: 1000 rpm/s, speed: 2000 rpm, time: 100s
  - PMMA -> ramp: 1000 rpm/s, speed: 2000 rpm, time: 100s
- **center the wafer** with the waver holder **on the spin-coater chuck**
- **turn on the vacuum**

There are two possibilities how you spin-coat your wafer. Either dynamically or statically

<u>dynamically</u>	<u>statically</u>
<ul style="list-style-type: none"><li>• <b>close the lid</b></li><li>• be ready with your pipette to put the resist through the hole in the lid on the wafer</li><li>• <b>start the program</b>, and when you are sure it runs correctly (speed up to the wanted rpm etc...) <b>put the resist</b> on the wafer. To make sure to avoid bubbles on the wafer do <u>not</u> put all of the resist in the pipette on the wafer.</li></ul>	<ul style="list-style-type: none"><li>• <b>put the resist</b> on the wafer so that nearly the whole wafer is covered. Do <u>not</u> put so much that it reaches the edge or flows over the edge. When it creeps under the wafer you can't be sure that the wafer will be plain on the e-beam holder etc.</li><li>• again avoid bubbles by not putting all of the resist in the pipette on the wafer</li><li>• <b>close the lid</b></li><li>• <b>start the program</b></li></ul>

- when the program is done, open the lid, take the wafer at the waferflat with a tweezer and put it on the **hotplate**
- start the **stopwatch**
- after the time you want to bake your resist put the wafer on a cleanroom towel for a while or blow it with nitrogen to **cool down the wafer**
- then put it back in the wafer box or spin-coat another resist layer
- when you are done, **clean the spincoater** with the cleanroom towels and Isopropanol!

### **Sputter gold:**

What you need:            tweezer

- for qubit fab it turned out that it is best when the **table** of the sputter coater is **at the very bottom**
- **put the wafer** with the side you want to write on, facing upwards **on the table**
- **turn on the machine** -> it starts to pump the vacuum
- the sputter coater should be set to 10 mA and around 0,6 mbar (for qubit fab), **set the time** you want to sputter the gold (by pressing the "Pause" button and increase or reduce the time)
- wait until the needle doesn't move anymore -> then press "**Flush**" -> wait a few second -> press again
- wait again until the needle doesn't move (the vacuum should be better now) -> press "**Leak**"
- wait again until the needle doesn't move anymore (should now go to the set 0,6 mbar) -> press "**Start**" (now the current is turned on and you can see the plasma)
- **wait until the time is up**
- **just turn off the machine** and put out the wafer

### **Electron-beam lithography:**

What you need:            Tweezer  
                                 Nitrogen gun

ToDo:

- **Design** your structures. Set the **dose value** for each design element! Place the design/**working area at (U,V) = (0,0)**.

- Drive z to 26 mm
- Activate 10  $\mu\text{m}$  aperture: 30 kV, 10  $\mu\text{m}$ , 10 mm WD (working distance) (**small aperture**)
- **Origin + angle correction**
- **Image optimization** with 30 kV, 10  $\mu\text{m}$ , 10 mm WD -> save/pipette the new values
- Activate 120  $\mu\text{m}$  aperture: 30 kV, 120  $\mu\text{m}$ , 10 mm WD (**big aperture**)
- **Image optimization** with 30 kV, 120  $\mu\text{m}$ , 10 mm WD -> save/pipette the new values
- **Writefield Alignment for big aperture**
  - 1000  $\mu\text{m}$  WF – Manual ALWF 100  $\mu\text{m}$  marks
  - 1000  $\mu\text{m}$  WF – Manual ALWF 10  $\mu\text{m}$  marks
- Save! Stay at the same position!!!
- Activate small aperture
- **Writefield Alignment for the small aperture**
  - 100  $\mu\text{m}$  WF – Manual ALWF 25  $\mu\text{m}$  marks
  - 100  $\mu\text{m}$  WF – Manual ALWF 5  $\mu\text{m}$  marks
  - 100  $\mu\text{m}$  WF – Manual ALWF 1  $\mu\text{m}$  marks
- Save!
  
- **Measure beam current** (Faraday Cup on holder; drive back) (with small aperture)
- **Drag and drop the design layers** written with the **small aperture into the positionlist**
- 'Properties – PositionButton – Calculator... -> Area Dwell Time (Area Step Size: 0,002  $\mu\text{m}$ ; Area Dose: 80  $\mu\text{C}/\text{cm}^2$ ; Area Line Spacing: 0,002  $\mu\text{m}$ )'
- **Drag and drop the design layers** written with the **big aperture into the positionlist**
  - 'Properties' - **NOT** PositionButton!, but add by hand +0,45 mm in U- and V-direction
  - Either you measured the beam current for the big aperture before and can write in the Area Dwell Time (Area Step Size: 0,02  $\mu\text{m}$ ; Area Dose: 80  $\mu\text{C}/\text{cm}^2$ ; Area Line Spacing: 0,02  $\mu\text{m}$ ) by hand, or you put an extra comment in the positionlist to measure the beam current after the lithography with the small aperture and let it calculate then.
- **Start ☺**

### **Wash off lugol:**

#### What you need:

Tweezer  
 Small petri dish  
 Lugol solution  
 Orbital shaker  
 Stop watch  
 Spray bottle of distilled water  
 Nitrogen gun

- Mix the **lugol solution** if you don't have one -> 8 g  $\text{I}_2$  : 80 g KI : 80 ml  $\text{H}_2\text{O}$  -> mix 3h at 80 rpm on orbital shaker
- Fill a small petri dish with the solution and put it on an **orbital shaker at 80 rpm**
- Take the wafer on the wafer flat and put it, facing the **gold upwards**, in the solution **for 1 min**
- **Rinse the wafer** with distilled water (don't let the liquid try on the wafer! Don't use Aceton or Isopropanol!!!)
- **Blow dry** with nitrogen

### Development:

What you need:

- Chiller
- Tweezer
- Stop watch
- Isopropanol
- Glass beaker with distilled water
- Nitrogen gun

- Fill the chiller with a mixture of **IPA and H<sub>2</sub>O (3 : 1)** and cool it down to about **6°C**.
- Take the wafer with the tweezer on the waferflat and put it for **1 min 45 s in the cold mixture**. Stir a bit.
- **Afterwards** put the wafer **immediately in** the beaker with **distilled water (for 30 s)** to stop the development
- **Blow dry** with nitrogen

### Plassys:

What you need:

- Tweezer

1. **Vent** (until atmospheric pressure lamp lights up)
2. **Build in your wafer** so that the flat is aligned with the bottom line on the holder (at least for the bridge free qubits with the 2 angle evap. from opposite sites)
3. **Pump**
4. **Fill cold trap** (open valve and look at the cold trap. It is full, when liquid nitrogen comes out...!)
5. **Wait 3h** (load lock:  $\sim 10^{-7}$  mbar; chamber:  $\sim 10^{-8}$  mbar)
6. **Select your process** (maybe change something)
7. **Turn on:** voltage, Kaufman source, Telemark (in this order!)
8. **Run process** (copy the filename down to the logfilename)  
-> when the plasma breaks down and the beam current drops to zero one can abort the process and either start it again or change something in the recipe... (don't have to wait until the error occurs) when a discharge error **HLP26** appears, then one has to reset the 'Kaufmansource'/the discharge thing by pushing the left down button and the upper one from the next buttons on the right next to it.
9. When it's done -> **switch it off** (first Telemark, then Kaufman source, then voltage)
10. **Vent** (until upper light on the right light up)

### Lift off:

What you need:

- Tweezer
- Big glass beaker with Aceton
- Sonicator

- Put the wafer for **5 min in Aceton**
- **Sonicate** the wafer in the Aceton for **1 min at 35 kHz and 20% power**
- **Leave the wafer** (in a wafer holder) **in Aceton** until most of the aluminium is gone (few h – over night)
- **Sonicate** the wafer **again** and rinse it with Aceton, Isopropanol and distilled water
- **Blow dry** it



### **Tipps and Tricks (e-beam):**

- The smaller the working distance the better the resolution
- 50 / 30 are good values for Contrast & Brightness
- A different aperture, working distance and EHT change the stigmatism and the aperture alignment!
- For FBMS (fixed beam moving stage) mode one has to do an additional 'beam tracking alignment'
- Make sure you are in the 'global U-V-system' before you start the lithography!
- 'Meander mode' is faster than 'Line mode', but 'Line mode' is more accurate as you don't have the Hysteresis-Effect
- Max. beam speed = 1 mm/s -> recommended = lower than 0.2 mm/s
- If you don't see anything -> try to switch between 'patterning' & 'imaging' mode!